High Resolution Observations and Modeling of MG0414+0534

by

John D. Ellithorpe

B.S. Physics, University of California, Irvine (1990)

Submitted to the Department of Physics
in partial fulfillment of the requirements for the degree of

Doctor of Philosophy in Physics

at the

MASSACHUSETTS INSTITUTE OF TECHNOLOGY

June 1995

© Massachusetts Institute of Technology 1995. All rights reserved.

Author_____
Department of Physics
May 18, 1995

Certified by_____
Jacqueline N. Hewitt
Class of 1948 Associate Professor of Physics
Thesis Supervisor

Accepted by_____
George F. Koster
Chairman, Graduate Committee

MASSACHUSETTS INSTITUTE OF TECHNOLOGY
JUN 26 1995
LIBRARIES
Science

High Resolution Observations and Modeling of MG0414+0534

by

John D. Ellithorpe

Submitted to the Department of Physics
on May 18, 1995, in partial fulfillment of the
requirements for the degree of
Doctor of Philosophy in Physics

Abstract

Gravitational lenses provide unique opportunities to probe distant galaxies and to examine models of the universe. We focus our attention on the gravitational lens MG 0414+0534. The bright four-image geometry and source variability make this system an excellent candidate for study. The first step in addressing astrophysical applications is the accurate determination of the lens matter distribution. In this thesis, we focused on improving the lens inversion algorithms and obtaining high-resolution observations of MG 0414+0534 to yield a reliable reconstruction of the lens. We then use this information to measure astrophysical properties of the lens and universe.

Multiple imaging by the lens provides strong constraints in the observed images allowing reconstruction of both the total matter distribution in the lens and the light distribution in the source. Although the lens inversion algorithm, LensClean, has been applied successfully, we find systematic errors which bias the results. Systems with compact images are affected to a greater extent, though the effects are also significant in systems dominated by diffuse emission. The primary errors result from the inclusion of negative clean components and the assumption that the standard image reconstruction procedures do not affect the lens modeling. We develop the Visibility LensClean algorithm which removes the systematic errors by requiring positive clean components and by operating directly on the complex visibility data. We find the Visibility LensClean algorithm dramatically reduces the systematic errors and provides more reliable lens inversion results. This algorithm also yields a better reconstruction than the standard image reconstruction techniques once a lens model is found which fits the system reasonably well.

Using 15 GHz (λ2cm) VLA observations, we find that a simple monopole plus quadrupole structure is insufficient in describing the lens in MG 0414+0534. The angular structure of the lens models does not produce the observed image geometry, resulting in a position error of $\sim 0\farcs1$. Since the nature of LensClean requires that the nonlinear equation for the images be solved efficiently, we can not explore a more general class of lens models within the LensClean framework at present. Instead,

using a point source inversion procedure, we find the lens is fit satisfactorily by a singular isothermal sphere plus the two lowest order terms in the multipole expansion due to an mass distribution outside the ring of images, $\frac{1}{2}\gamma r^2 \cos 2(\theta - \theta_\gamma)$ and $\beta r^3 \cos 3(\theta - \theta_\beta)$. We observed MG 0414+0534 at 5 GHz (λ6cm) using Very Long Baseline Interferometry and detected all the components except C. We find resolved structures in A1, A2, and B at the 10 milliarcsecond level. We modeled the lens using the two strongest components in each VLBI image and find the $\cos 3\theta$ model does fit the VLBI data and the best fit lens parameters are consistent with those found with the 15 GHz VLA data.

We believe the galaxy detected by Schechter & Moore (1993) is the primary object responsible for the lensing. The orientation of the quadrupole moment is consistent with the shear caused by other objects present in the field, although the inferred masses of those objects would be much larger than expected for normal galaxies. We believe the $\cos 3\theta$ perturbation to the ellipticity is due to object X. If we assume an Einstein-de Sitter cosmology and a lens redshift of $z_L = 0.5$, we find the mass of the primary galaxy is $8.5 \pm 0.1 \times 10^{11} h_{75}^{-1} M_\odot$ and the velocity dispersion is 258 ± 1 km/s. These values are consistent with typical elliptical galaxies. The best fit lens model predicts $0.6 \sim 0.8$ for the A2/A1 magnification ratios of the VLBI components. If the quasar core is associated with these components, the predicted magnification ratios cannot explain the optical A2/A1 flux ratio of 0.3. We estimate the apparent magnitude of the galaxy and find that if the lens is a normal elliptical galaxy then it contains a significant amount of dust or is at a large redshift ($z_L \gtrsim 1$).

Assuming a time delay of 2 weeks for the A1-B time delay and lens redshift of $z_L = 0.5$, the best fit lens model predicts $H_o = 60 \pm 8$ km s^{-1} Mpc^{-1} in an Einstein-de Sitter cosmology. The exact value of H_o is model dependent, and constraining the radial shape of the lens is necessary to provide a unique relationship between the time delay and the Hubble constant. If H_o is measured independently, this system may be able to put limits on Ω and possibly Λ. Deep high-resolution observations at optical and radio wavelengths should provide more stringent constraints on the lens inversion and may reveal more information about the nature of object X. Furthermore, performing the lens inversion with the Visibility LensClean algorithm will reduce the possible range of lens models by using all the available information in the observations.

Thesis Supervisor: Jacqueline N. Hewitt
Title: Class of 1948 Associate Professor of Physics

To the memory of my father

Acknowledgments

I wish to thank those people who have helped me during my tenure at the Massachusetts Institute of Technology. I thank my advisor, Professor Jacqueline Hewitt, for allowing me to pursue the research in this thesis. She has embarked on many intriguing research topics during the course of my thesis and I am sincerely grateful to have worked with her. I also thank Professor Edmund Bertschinger and Professor Peter Fisher for participating on my thesis committee. Professor Bertschinger gave his time and provided many useful suggestions. Even though Professor Fisher is not an astrophysicist, his perspective and suggestions improved the quality of this thesis. I must also thank Professor Kerson Huang for being on my thesis committee for over a year. I regret that Professor Huang was not able complete his service on my committee due to his sabbatical this semester.

I thank Professor Christopher Kochanek at the Harvard-Smithsonian Center for Astrophysics. I am very grateful for his many useful discussions and scientific insights which helped me over the past two years. I am privileged to have been able to work with him.

I wish to thank all those who have worked in the radio astronomy group at MIT over the past five years. I have enjoyed working with Grace Chen, Charlie Katz, and Christopher Moore. My years at MIT would not have been the same without Max Avruch, Sam Conner, and with the rest of Professor Burke's group. I would also like to thank Mike Titus at the Haystack Observatory. His assistance and friendship was invaluable during the correlation of the 5 GHz VLBI observation.

I thank Krishna Shenoy for his many years of friendship and support. I have enjoyed our many discussions and adventures both at UC Irvine and MIT. I also thank my family for their years of love and support. I especially thank my father for his continuous belief in my abilities. Finally, and most importantly, I want to thank Elizabeth Barton for her love and understanding and Elsie for her constant attention.

Contents

Abstract **2**

Acknowledgments **5**

1 Introduction **20**

1.1 The MG 0414+0534 System 21

1.2 Motivation 24

1.3 Chapter Summary 26

2 Interferometry Theory **27**

2.1 Introduction 27

2.2 The Two-Element Interferometer 28

2.3 Aperture Synthesis 31

2.4 Smearing Effects 34

2.4.1 Bandwidth Smearing 34

2.4.2 Time-Average Smearing 35

2.5 Image Reconstruction 36

2.5.1 Self-Calibration 37

2.5.2 Deconvolution Algorithms 38

2.6 Very Long Baseline Interferometry 41

2.6.1 Amplitude Calibration 41

2.6.2 Fringe Fitting 42

3 Gravitational Lensing and Lens Inversion **46**

3.1 Gravitational Lens Theory 46

3.2 Lens Inversion 54

3.3 Clean map LensClean 57

3.4 Negative Clean Components 59

3.5 Visibility LensClean 63

3.5.1 Self-Calibration with a Model Consistent with Lensing 66

3.6 Clean map LensClean vs Visibility LensClean 66

3.6.1 MG 0414+0534 67

3.6.2 MG 1654+1346 71

3.7 Discussion of LensClean 78

4 Modeling the 15 GHz VLA Data **81**

4.1 Visibility LensClean 81

4.1.1 Lens Models 82

4.1.2 Results 83

4.2 Point Source Lens Inversion 91

4.2.1 Lens Models 94

4.2.2 Results 95

5 5 GHz VLBI Observations **102**

5.1 Observations 102

5.2 Correlation 103

5.3 Calibration 105

5.3.1 Fringe Fitting 105

5.3.2 Amplitude Calibration 106

5.4 Image Reconstruction 107

5.4.1 Editing 107

5.4.2 Mapping Procedure 110

5.4.3 0423-013 112

5.4.4 MG 0414+0534 112

5.5 Image Reliability 116
5.5.1 Consistency within the Data Sets 117
5.5.2 Time Segmentation 117
5.5.3 Consistency with Gravitational Lensing 119
5.6 Lens Inversion 122

6 Conclusions **128**
6.1 Lens Inversion Results 128
6.2 Optical-Radio Flux Ratio Discrepancy 132
6.3 Nature of the Lens 133
6.4 Prospects for Determining H_o 138
6.5 Future Prospects 140

A Lens Models **142**
A.1 Singular Isothermal Sphere (SIS) plus External Shear 142
A.2 Generalized Monopole plus External Shear 143
A.3 Approximate Singular Isothermal Ellipsoid 145
A.4 De Vaucouleurs Mass Distribution plus External Shear 146
A.5 Approximate Elliptical Mass Distribution 147
A.6 SIS plus External Shear and Cosine 3θ Component 149
A.7 SIS plus External Shear and Octupole 150

Bibliography **152**

List of Figures

1-1 Total Intensity Map of MG 0414+0534 from 15 GHz VLA Observations (Katz & Hewitt 1995). The contour levels are -0.375, 0.375, 0.75, 1.5, 3, 6, 12, 24, 48, and 96 percent of the peak, 160.7 mJy/Beam. The $\times$ symbol shows the position of the lens galaxy (Falco 1995). The + symbol shows the position of Object X (Schechter & Moore 1993). . . 22

2-1 Diagram of the two element interferometer. $\vec{b}$ is the vector from antenna 1 to antenna 2, $\vec{s}$ is the direction to the source, τ_g is the geometric time delay, and τ_o is a delay introduced before correlation. 29

3-1 Gravitational lens diagram. The path of a single light ray is drawn. D_{ij} is the angular diameter distances from point i to point j, $\vec{\theta}$ is the angular position of the image (apparent source), $\vec{\beta}$ is the angular position of the source in the absence of a lens, and $\vec{\alpha}_t$ is the deflection angle. 47

3-2 The deflection angle diagram for a point lens of mass M. The axes are in units of the "Einstein" ring radius. 49

3-3 The deflection angle diagram for a general lens with circular symmetry. 50

3-4 The caustics and critical lines for a strong non-singular elliptical lens. Panel (a) shows the source plane caustics. Panel (b) shows the image plane critical lines. The $\square$, $\bullet$, and $\times$ symbols represent sources in the one, three, and five image regions, respectively. 53

3-5 Final CLEAN image of MG 0414+0534 from a 15 GHz VLA observation of MG 0414+0534 (Katz & Hewitt 1995) used in the Clean map LensClean analyses. The contour levels are -1.5, -0.75, -0.375, 0.375, 0.75, 1.5, 3, 6, 12, 24, 48 and 96 percent of the peak, 158.4 mJy/Beam. The beam FWHM is 0.″12 by 0.″11. 59

3-6 Residual Map from Best Fit SIS plus external shear model using the Clean map LensClean method including negative clean components. The absolute contour levels are the same as Figure 3-5. 60

3-7 Distribution of clean components used in the best fit SIS plus external shear model using the Clean map LensClean method including negative clean components. 62

3-8 Multiplicity image from the best fit SIS plus external shear model using the Clean map LensClean method including negative clean components. The curves are boundaries between the 1, 2, and 4 image regions. A1, A2, B, and C show the locations of the MG 0414+0534 components and + symbol shows the location of the clean components west of B. 63

3-9 The MG+0414+0534 residual images after LensClean. The absolute contour levels are the same as Figure 3-5. Panel (a) shows the best fit residuals after Clean map LensClean. Panel (b) shows the residuals after Visibility LensClean using the best fit Clean map LensClean lens model. Panel (c) shows the best fit residuals after Visibility LensClean. Panel (d) shows the best fit residuals after Visibility LensClean on the self-calibrated data set. 68

3-10 Final CLEAN image of MG 1654+1346 used in Clean map LensClean. The contour levels are -3, -1.5, 1.5, 3, 6, 12, 24, 48, and 96 percent of the peak, 5.01 mJy/Beam. The beam FWHM is 0.″21 by 0.″19. 72

3-11 The MG 1654+1346 residual images after LensClean. The absolute contour levels are the same as Figure 3-10. Panel (a) shows the best fit residuals after Clean map LensClean. Panel (b) shows the best fit residuals after Visibility LensClean. Panel (c) shows the best fit residuals after Visibility LensClean on the self-calibrated data set. . . 74

3-12 The distribution of clean components using the Clean map LensClean algorithm on the 5 GHz MG 1654+1346 data set. Panel (a) shows the distribution using the constraint of positive definite clean components and Panel (b) shows the distribution with negative clean components. The + symbols show the positions of the largest negative clean components ($\gtrsim 15$ μJy/Beam). 76

3-13 The reconstructed Visibility LensClean images of MG 1654+1346 using the self-calibrated data set. The absolute contour levels are the same as Figure 3-10. Panel (a) shows the reconstruction at normal resolution, 0.″21 by 0.″19. Panel (b) shows the super-resolved reconstruction using a 0.″1 restoring beam. 78

4-1 Panel (a) shows the reconstructed image and Panel (b) shows the residual image from the best fit singular isothermal sphere (SIS) plus external shear model (1). The absolute contours levels are the same as Figure 3-5. 85

4-2 Panel (a) shows the reconstructed image and Panel (b) shows the residual image from the best fit approximate singular isothermal ellipsoid model (3). The absolute contours levels are the same as Figure 3-5. . 86

4-3 Panel (a) shows the reconstructed image and Panel (b) shows the residual image from the best fit generalized monopole plus external shear model (2) using $\alpha = 0.0$ and $s = 0.''005$. The absolute contours levels are the same as Figure 3-5. 86

4-4 Panel (a) shows the reconstructed image and Panel (b) shows the residual image from the best fit generalized monopole plus external shear model (2) using $\alpha = 0.5$ and $s = 0''.005$. The absolute contours levels are the same as Figure 3-5. 87

4-5 Panel (a) shows the reconstructed image and Panel (b) shows the residual image from the best fit generalized monopole plus external shear model (2) using $\alpha = 1.0$ and $s = 0''.005$. The absolute contours levels are the same as Figure 3-5. 87

4-6 Panel (a) shows the reconstructed image and Panel (b) shows the residual image from the best fit generalized monopole plus external shear model (2) using $\alpha = 1.0$ and $s = 0''.05$. The absolute contours levels are the same as Figure 3-5. 88

4-7 Panel (a) shows the reconstructed image and Panel (b) shows the residual image from the best fit generalized monopole plus external shear model (2) using $\alpha = 1.0$ and $s = 0''.20$. The absolute contours levels are the same as Figure 3-5. 88

4-8 Panel (a) shows the reconstructed image and Panel (b) shows the residual image from the best fit de Vaucouleurs plus external shear model (4) using $R_e = 1''.25$. The absolute contours levels are the same as Figure 3-5. 89

4-9 Panel (a) shows the reconstructed image and Panel (b) shows the residual image from the best fit approximate elliptical mass distribution model (5) using $\alpha = 0.5$. The absolute contours levels are the same as Figure 3-5. 89

4-10 Panel (a) shows the reconstructed source and tangential caustic and and Panel (b) shows the point images and the tangential critical for Model 4. The image in panel (a) is a factor of four smaller in each dimension than the image in panel (b). Due to the finite pixel size, the source components do not lie on top of one another. 97

4-11 Panel (a) shows the reconstructed source and tangential caustic and and Panel (b) shows the point images and the tangential critical for Model 8. The image in panel (a) is a factor of four smaller in each dimension than the image in panel (b). Due to the finite pixel size, the source components do not lie on top of each other. 100

4-12 Plot of χ^2 versus the flux of component B. We used the $\cos 3\theta$ lens model. The χ^2 is the value after optimizing all the lens model parameters. The □ symbol indicates the measured flux of component B used in the lens inversion. 101

5-1 Visibility amplitude for 0423-013 (J2000) on Haystack baselines. The amplitudes dramatically drop after 13:00 UT. 109

5-2 The left panel shows the *u-v* coverage and the right panel shows the dirty beam for the 5 GHz (λ6cm) observation of MG 0414+0534 after the data were edited. To produce the dirty beam, the data were uniformly weighted with a *u-v* box size of 3 pixels. The FWHM of the central lobe is 17 mas by 8 mas. The largest sidelobe is 50 percent of the peak. 110

5-3 Final 5 GHz image of 0423-013 (J2000). The data have been uniformly weighted with a *u-v* box size of 3 pixels. The size of the restoring beam is given in the lower left corner. 113

5-4 Final 5 GHz image of each component in MG 0414+0534. Clockwise from the bottom left, the images are A1, A2, B, and C. The data have been uniformly weighted with a *u-v* box size of 3 pixels. The contour levels are -2, -1, 1, 2, 4, 8, 16, 32, 64, and 96 percent of the peak flux in A1 (185 mJy/Beam). The size of the restoring beam is shown in the lower left corner of each panel. The image parameters are given in Table 5.3. 115

5-5 Final 5 GHz images of A1/A2 and B using data from 16:00 UT to 23:00 UT. The data have been uniformly weighted with a u-v box size of 3 pixels. The contour levels are -3, -1.5, 1.5, 3, 6, 12, 24, 48, and 96 percent of the peak in A1 (193.8 mJy/Beam). The size of the restoring beam is shown in the lower left corner of each panel. 118

5-6 The upper right panel shows the reconstructed source brightness distribution of MG0414 from the clean component model of A1. The reconstructed source has been convolved with the lens distorted clean beam. The other panels contain the reconstructed images of MG0414 using the reconstructed MG0414 source. The source and images were created using the Gravitational Image Tracing (GrIT) package. The brightest two components are indicated in each panel with the Roman numeral: I is the brightest component and II is the second brightest component at A1. 121

5-7 The reconstructed images for the best fit $\cos 3\theta$ model. The upper right panel shows the reconstructed source brightness distribution of MG0414 from the clean component model of A1. The reconstructed source has been convolved with the lens distorted clean beam. The other panels contain the reconstructed images of MG0414 using the reconstructed MG0414 source. The source and images were created using the Gravitational Image Tracing (GrIT) package. The brightest two components are indicated in each panel with the Roman numeral: I is the brightest component and II is the second brightest component at A1. 126

6-1 Mass of the primary lensing galaxy as a function of lens redshift. We assume a Friedmann cosmology with $\Lambda = 0$ and $H_o = 75$ km s^{-1} Mpc^{-1}. We plot three curves corresponding to $\Omega = 0.2$, 1.0, and 1.5. 134

6-2 Velocity dispersion of the lensing galaxy as a function of lens redshift and Ω. We plotted three values of Ω: 0.2, 1.0, and 1.5. 136

6-3 Apparent magnitude of the lensing galaxy as a function of lens redshift and Ω using the Faber-Jackson relation which assumes the lens galaxy is a normal elliptical galaxy. We have assumed $H_o = 75$ km s^{-1} Mpc^{-1} and plotted curves three values of Ω: 0.2, 1.0, and 1.5. 137

6-4 Hubble constant for different lens models. We have assumed a time delay of 2 weeks between A1 and B. We have assume $\Omega = 1$ and $\Lambda = 0$. 139

6-5 Hubble constant for different cosmologies and best fit lens model. We have assumed a time delay of 2 weeks between A1 and B. 140

List of Tables

3.1 Results for the MG 0414+0534 system using the singular isothermal sphere plus external shear model. VLC/SC indicates the results using the visibility data set after self-calibration with the converged VLC model. The lens position is measured relative to component B. P-P indicates the peak-to-peak value in the residual image. θ_γ is measured north through east. The CLC confidence intervals are calculated using $\Delta\chi^2 \leq 15.1$ and the VLC confidence intervals are calculated using $\Delta\chi^2 \leq 4$. χ^2 is calculated using χ^2_{clc} for the CLC model and χ^2_{vlc} for the VLC models. 69

3.2 Results for the MG 1654+1346 system using the approximate elliptical mass distribution. VLC/SC indicates the results using the visibility data set after self-calibration with the converged VLC model. The lens position is measured relative to the quasar core. P-P indicates the peak-to-peak value in the residual image. θ_γ is measured north through east. The CLC confidence intervals are calculated using $\Delta\chi^2 \leq 15.1$ and the VLC confidence intervals are calculated using $\Delta\chi^2 \leq 4$. χ^2 is calculated using χ^2_{clc} for the CLC model and χ^2_{vlc} for the VLC models. 75

4.1 Visibility LensClean results on the 15 GHz VLA MG 0414+0534 data set. The results are from Visibility LensClean on the original self-calibrated data set. The errors are 95 percent confidence levels. The lens position is measured relative to component B. The shear position angle is measured north through east. P-P is the peak-to-peak value in the residual image. 84

4.2 Image positions and peak fluxes for the components in MG0414. The image positions are measured relative to component B. These data were taken from Katz & Hewitt (1995). 93

4.3 Best fit lens model parameters and error statistics for the singular isothermal sphere plus external shear and approximate singular isothermal ellipsoid using the point source solver. The errors are 95 percent confidence intervals. The lens position is measured relative to component B. These models have six degrees of freedom. 95

4.4 Best fit lens model parameters and error statistics for lens models 3, 4, and 5 using the point source solver. The errors are 95 percent confidence levels. The lens position is measured relative to component B. These models have four degrees of freedom. 96

4.5 Best fit lens model parameters and error statistics for lens models 6, 7, and 8 using the point source solver. The errors are 95 percent confidence levels. The lens positions are measured relative to component B. Model 6 has five degrees of freedom and models 7 and 8 have three degrees of freedom. 99

5.1 Correlation delay center coordinates. The MG 0414+0534 positions are taken from Katz & Hewitt (1995) and the 0423-013 position is from the VLA Calibrator Manual. All positions measured with respect to the J2000 coordinate system. 104

5.2 Four point source model of MG 0414+0534 used for the global fringe fitting. The positions and flux ratios are relative to B. The absolute positions and relative fluxes were obtained from Katz & Hewitt (1995) and the absolute flux level was determined from Hewitt *et al.* (1992). All positions are measured with respect to J2000 coordinates. 107

5.3 Parameters from the 5 GHz VLBI images of MG 0414+0534. The positions ($\triangle\alpha$,$\triangle\delta$) are measured from the peak in the image to the peak in the B image. σ is determined in empty regions of the final images. The 5 GHz VLA integrated fluxes are taken from Katz & Hewitt (1995). 116

5.4 Parameters from the 5 GHz VLBI images of MG 0414+0534 using only the data from 16:00 UT to 23:00 UT. σ is determined in empty regions of the final images. † The noise level for A1 and A2 was determined from the same image. 119

5.5 Parameters for the singular isothermal sphere plus external shear lens model used to ray-trace the A1 clean component model. The lens position (x,y) is measured relative to B and x increases to the west. θ_γ is measured north through east. 120

5.6 Input positions and fluxes from the VLBI images. The component positions are measured with respect to the B primary component. . . 123

5.7 Best fit lens model parameters and error statistics for the $\cos 3\theta$ model on the 5 GHz VLBI data. P means only the primary components were fit. P&S 1 includes both the primary and secondary components were used in the inversion and P&S 2 includes the primary component and only the fluxes of the secondary component. P&S+C is identical to P&S 1 except that the VLA C position was added as a constraint. The errors are 95 percent confidence levels. The lens position is measured relative to the primary component in B. The position angles are measured north through east. 124

5.8 The relative separations between the primary and secondary components for both the 5 GHz VLBI data set and best fit lens model. . . . 125

6.1 Parameters for lens model which best fit the MG 0414+0534 system, the singular isothermal sphere plus external shear and $\cos 3\theta$ component. The errors are 95 percent confidence levels. The lens position is measured relative to the primary component in B. The position angles are measured north through east. 129

6.2 Magnifications at the positions of the primary and secondary components predicted by the best fit $\cos 3\theta$ lens model. 132

Chapter 1

Introduction

Long before the development of the general theory of relativity, it was speculated that light rays would be deflected by a massive body in the same manner as normal particles (Michell 1784; Laplace 1795). Soldner (1804) predicted that if the light from a star grazed the surface of the sun, the apparent position of the star would move by 0.85 arcseconds. Einstein (1915) applied his general theory of relativity to this problem and predicted that, due to the curvature of space and time dilation, a ray of starlight would be deflected by twice that predicted by the classical methods. During a solar eclipse in 1919, Eddington measured the apparent shift of stars, thus proving light is affected by gravity (Eddington 1919; Dyson *et al.* 1920). The magnitude of the shifts ruled out the Newtonian description and provided a strong confirmation of general relativity. Using interferometry, these observations have been refined such that the agreement with general relativity is better than a tenth of a percent (Lebach *et al.* 1995).

Eddington (1920) and Chowlson (1924) soon realized that the gravitational effect can cause multiple images of a single background source. They showed that if a star lies sufficiently close to the line-of-sight of another more distant star, a second image of the background star will appear. In the dramatic case of a star positioned directly behind an intervening star, the image of the background star will be distorted into an entire ring (called an "Einstein" ring). However, Einstein (1936) calculated the image separations would be too small to observe. Zwicky (1937a) was the first to

recognize that the lensing of galaxies by galaxies would lead to detectable deflections. He stated that the probability of finding a gravitational lensing system is "practically a *certainty*" because of the masses and distances involved (Zwicky 1937b). He was also the first to realize the importance of gravitational lenses as a probe of distant galaxies and cosmology.

Even though Zwicky predicted that gravitational lenses should be easily detected, the first discovery of a lens system did not occur until 1979. Walsh, Carswell, & Weymann (1979) observed the "twin QSO" system, 0957+561, and found that both QSO images, separated by 6 arcseconds, had a redshift of $z = 1.41$ and nearly identical spectra. From this spectroscopic evidence they concluded that it was very unlikely that the images were of separate objects. Since this discovery, many different gravitational lens systems have been found: point-like systems, arcs, and rings. The point-like systems consist of two or more compact images of a distant quasar, such as 0957+561 and MG0414+0534 (Hewitt *et al.* 1988a). The arcs are usually lensed images of faint blue galaxies by a cluster. The blue color distinguishes the arcs from intrinsic structures within the cluster. Examples are seen in Abell 370 (Lynds & Petrosian 1986) and Abell 963 (Lavery & Henry 1988). The most dramatic examples of gravitational lensing are the ring systems (also referred to as "Einstein" rings). The lobe of a distant radio galaxy is lensed into a ring of emission, such as in MG1131+0456 (Hewitt *et al.* 1988b) and MG1654+1346 (Langston *et al.* 1989). The rings are always images of an extended background object, since the probability of finding a perfect alignment of a compact object necessary to produce a true "Einstein" ring is effectively zero.

1.1 The MG 0414+0534 System

In contrast to the early discoveries of gravitational lenses, MG 0414+0534 (hereafter MG0414) was discovered by a systematic search for lenses using high-resolution radio observations (Hewitt *et al.* 1988a). MG0414 was selected as a gravitational lens candidate because of its unusual radio structure, consisting of three bright objects. Through high-resolution VLA observations, Hewitt *et al.* (1992) discovered the system

actually comprised four images in a configuration suggestive of lensing of a compact object by a galaxy. Figure 1-1 shows the arcsecond-scale radio structure of MG0414

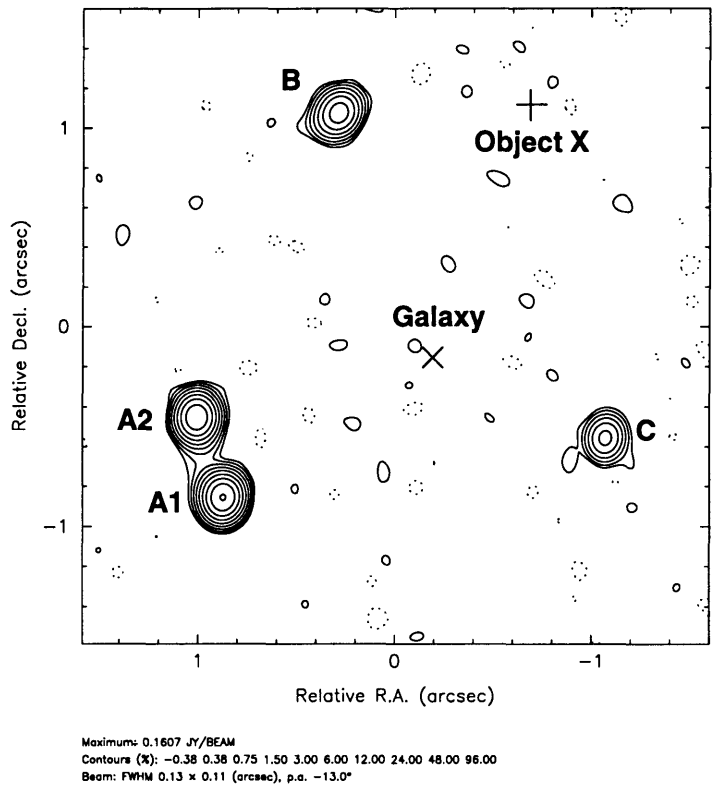

Figure 1-1: Total Intensity Map of MG 0414+0534 from 15 GHz VLA Observations (Katz & Hewitt 1995). The contour levels are -0.375, 0.375, 0.75, 1.5, 3, 6, 12, 24, 48, and 96 percent of the peak, 160.7 mJy/Beam. The × symbol shows the position of the lens galaxy (Falco 1995). The + symbol shows the position of Object X (Schechter & Moore 1993).

from 15 GHz Very Large Array[1] observations in January 1993 (Katz & Hewitt 1995). The close source-lens alignment in MG0414 leads to four images of the source, rather than the two images seen in the "Twin Quasar" gravitational lens system, 0957+561. All the components except C show extended structure. The A1 and A2 components have low-level emission extending towards each other. Component B is elongated along the NW-SE direction, approximately in a tangential direction with respect to

[1]The Very Large Array is part of the National Radio Astronomy Observatory which is operated by Associated Universities, Inc. under co-operative agreement with the National Science Foundation.

the lens that is near the center of the system.

If the lens has a smooth surface mass density, the number of images in the system must be odd (Schneider *et al.* 1992). The "odd" or "fifth" image is expected to lie near the lens position. Deep radio observations of MG0414 have not detected any emission from either the "fifth" image or the lensing galaxy (Katz & Hewitt 1995). The limits imposed on the "fifth" image magnification are useful since they correspond directly to upper limits on the central surface mass density (Kochanek 1991).

The flux in MG0414 is dominated by A1 and A2, which together contain 78 percent of the radio flux. Component B is the next brightest with 16 percent, and C has only 6 percent. The gravitational lensing effect is achromatic. In other words, if a source emits radiation at two frequencies, the deflection and magnification observed at both frequencies will be the same. A lens candidate can be confirmed by observations at multiple frequencies. This method assumes the intrinsic source structure does not vary with frequency and that additional effects such as dust extinction or microlensing by the lens galaxy are not present. Katz & Hewitt (1995) found the flux ratios at many radio wavelengths are equal, even though the total flux of the system changes rapidly with a steep spectral index of $\alpha = 0.8$ ($f \sim \nu^{-\alpha}$). Hence, there is little observational evidence for any absorption or microlensing at radio wavelengths. The radio flux ratios are expected to approximate the true lensing magnifications because the typical sizes of the radio sources are large compared with the expected cross-section for microlensing events (Witt *et al.* 1994; Blandford 1990).

Optical observations of MG0414 detected the same structure as seen in radio images, confirming MG0414 as a true gravitational lens (Hewitt *et al.* 1992). The relative positions of all components in optical images agree with those measured in the radio (Schechter & Moore 1993). The optical flux ratios, however, are not consistent with those measured at radio wavelengths. Lawrence *et al.* (1994) explained the flux ratio discrepancy through differential amounts of dust in the lensing galaxy. They found the background source is best fit by a $z = 2.64$ flat-spectrum quasar seen through $A_V = 4.5 \sim 6$ magnitudes of visual extinction. However, Witt, Mao, & Schechter (1994) found that microlensing can explain the optical flux ratios. Optical

monitoring of MG0414 is necessary to resolve the competing theories, since we expect that microlensing events will change over a timescale of months.

Schechter & Moore (1993) detected a single galaxy at the center of MG0414, which they believed responsible for the lensing. Optical and infrared spectroscopy have not found any features attributed to the lensing galaxy (Lawrence 1995; Hewitt *et al.* 1992). To the west of component B, a faint component (called "object X") has been observed (Schechter & Moore 1993; Angonin-Willaime *et al.* 1994). The nature of this object has not been determined although Angonin-Willaime *et al.* (1994) suggest that it is a distant galactic star. Observations with the Hubble Space Telescope show diffuse emission rather than a compact object at the position of object X (Falco 1995), implying that it is a galaxy. If object X is extragalactic and contains significant mass, its proximity to the line-of-sight will affect the simple lensing scenario.

1.2 Motivation

Gravitational lens systems can provide unique information about distant galaxies and cosmology. The most direct application is the determination of matter distributions in the lens galaxies. The rotation curves of spiral galaxies and velocity dispersion in clusters indicate significantly more mass than is inferred from summing the luminous matter. The gravitational lens effect is dependent only on the total matter distribution in the lens. Hence, reconstruction of the lens provides a probe into the dark matter distribution in the lensing galaxy (Kochanek 1995, for example).

Another intriguing use of gravitational lenses is as a cosmological ruler. Consider a lensing system which contains multiple images of a common source. The light rays from each image traverse different geometric path lengths and encounter different regions of the gravitational potential (Shapiro 1963). The differences in arrival times between images (referred to as "time delays") depend on the angular-diameter distances between the lens, source, and observer. Therefore, measurements of these delays can be used to estimate Hubble's constant, H_o (Refsdal 1964; Refsdal 1966).

This method requires that the background source have an observable parameter which varies with time. The variable flux at optical and radio wavelengths has led to measurements of a time delay in 0957+561 (Lehár *et al.* 1992; Press *et al.* 1992). However, the uncertainties in the lensing models result in large uncertainties in the estimate of H_o (Falco *et al.* 1991; Roberts *et al.* 1991).

Gravitational lenses are important since they can provide estimates of astrophysical parameters. The confidence limits depend on the accuracy of the lens reconstruction. Small changes in the matter distribution lead to uncertainties in the astrophysical interpretations. MG0414 was chosen as the focus of this study because the four image configuration gives more constraints in the lens inversion than the two image systems, such as 0957+561. Although MG0414 does not probe the lens potential as thoroughly as a ring system, the extended emission in the ring is too large to be variable. Monitoring of the components in MG0414 have found them to be variable at a level of a few percent (Moore & Hewitt 1995). In addition, this system consists of four bright, compact components at many wavelengths, making high-resolution observations feasible.

In this thesis, we pursued the goal of understanding the system through the lens modeling of the 0.″1 resolution VLA observations and the 0.″01 resolution Very Long Baseline Interferometry (VLBI) observations of MG0414. Using VLA observations of the ring, MG 1654+1346, Kochanek (1995) modeled the lens galaxy and found evidence for dark matter in the core of the galaxy, a giant elliptical at a redshift of 0.254. The lens galaxies in gravitational lens systems are generally large ellipticals because smaller spiral galaxies will not create the easily identified large separation systems. Therefore, the study of gravitational lenses can provide a window into the dynamics and structure of the cores of elliptical galaxies.

VLBI observations have proven effective in constraining the gravitational lens systems 0957+561 and 2016+112. Porcas *et al.* (1981) discovered the same core-jet structure in both 0957+561 images. Using this structure, Gorenstein *et al.* (1988a) derived the magnification matrix which relates the brightness distribution in one image to that in the other. Recent VLBI observations by Garrett *et al.* (1995) found

that the magnification matrix varies across the jet, as claimed by Conner, Lehár, & Burke (1992). To investigate the unusual gravitational lens 2016+112, Heflin *et al.* (1992) observed this system using a global VLBI array. He found the system was not consistent with a linear magnification matrix, indicating the source is evolving on a shorter timescale than the time delay, predicted to be between 8 and 11 months (Narasimha *et al.* 1987; Narasimha & Chitre 1989).

1.3 Chapter Summary

In Chapter 2, we review the theory of interferometry and aperture synthesis, including the effects specific to VLBI. Chapter 3 reviews the basic theory of gravitational lensing and the lens inversion problem. This chapter discusses the problems with the current implementation of the LensClean algorithm (Kochanek & Narayan 1992) and presents a modified implementation to remove these effects. In Chapter 4, we extensively model the MG0414 system using the 15 GHz VLA observations (Katz & Hewitt 1995). We explore a variety of simple lens models in LensClean and more complex models using "point solvers" (see Section 3.2). This work has been performed in collaboration with Professor Christopher Kochanek at the Harvard-Smithsonian Center for Astrophysics. Chapter 5 presents the 5 GHz VLBI observations of the MG0414 system. The data reduction procedures used to achieve the final images and their reliability are discussed. Using the components in the VLBI images, we modeled the system with the lens model parameterization which best fit the 15 GHz VLA observations. Chapter 6 discusses the results and future work.

Chapter 2

Interferometry Theory

2.1 Introduction

Any finite continuous function can be fully described by a complete set of Fourier components (Arfken 1985; Churchill & Brown 1976). Consider a two-dimensional brightness distribution $I(x, y)$ emitted from a source. Each Fourier component is isolated by modulating $I(x, y)$ with the corresponding basis function and integrating over space. The Fourier component is specified by the wave-vector $u\hat{x} + v\hat{y}$, which is orthogonal to the two-dimensional wave fronts and has length equal to the spatial frequency of that component. Therefore, the Fourier basis function is $e^{2\pi i(ux+vy)}$ and the projected Fourier component is,

$$S_o\Gamma(u, v) = \int \mathrm{d}x\mathrm{d}y I(x, y)e^{2\pi i(ux+vy)}. \tag{2.1}$$

The function $\Gamma(u, v)$, known as the complex visibility function, is the Fourier component normalized by the total flux of the source,

$$S_o = \int \mathrm{d}x\mathrm{d}y I(x, y). \tag{2.2}$$

Equation 2.1 relates the brightness distribution and the complex visibility function through a two-dimensional Fourier transform, and, thus, the x-y (or sky) plane and the

u-v (or visibility) plane are Fourier conjugate spaces. We have assumed that $I(x,y)$ is defined on a two-dimensional plane rather than the celestial sphere. This assumption is valid in the regime where the source size is small compared to the curvature of the sphere. The brightness distributions of astrophysical sources are purely real, requiring the visibilities to be conjugate-symmetric, i.e. $\Gamma(u,v) = \Gamma^*(-u,-v)$. Therefore, to fully specify a source brightness distribution, the complex visibility function must be measured over half the u-v plane.

A measurement with an interferometer is equivalent to projecting a sinusoidal pattern, or "fringes" (see Section 2.2), and integrating over the sky. Therefore, an interferometer measures the spatial Fourier components of astrophysical sources. Each (u,v) point corresponds to the vector pointing from one antenna to another, where the projected antenna separation is $\sqrt{u^2+v^2}$ and the orientation is specified by $\tan^{-1}\left(\frac{v}{u}\right)$.

In the following sections, we review the basic interferometry theory as applied to radio astronomy. For a more detailed discussion, we recommend Thompson, Moran, & Swenson (1986) and the VLA Summer School lectures (1989).

2.2 The Two-Element Interferometer

The basic element in interferometry is the two-element interferometer. Consider the two antennae shown in Figure 2-1. The relative orientation of the antennae is given by the baseline vector $\vec{b}$, pointing from one antenna to the other. The sign of the vector is not important, since the u-v plane is conjugate-symmetric. The radiation from a distant monochromatic point source of flux S_o reaches antenna 1 before antenna 2 by the geometrical delay,

$$\tau_g = -\frac{\vec{b}\cdot\vec{s}}{c} \tag{2.3}$$

where $\vec{s}$ is the source position unit vector and c is the speed of light. To compensate for this geometrical delay, we introduce an instrumental delay in the signal path from antenna 1,

$$\tau_o = -\frac{\vec{b}\cdot\vec{s}_o}{c}. \tag{2.4}$$

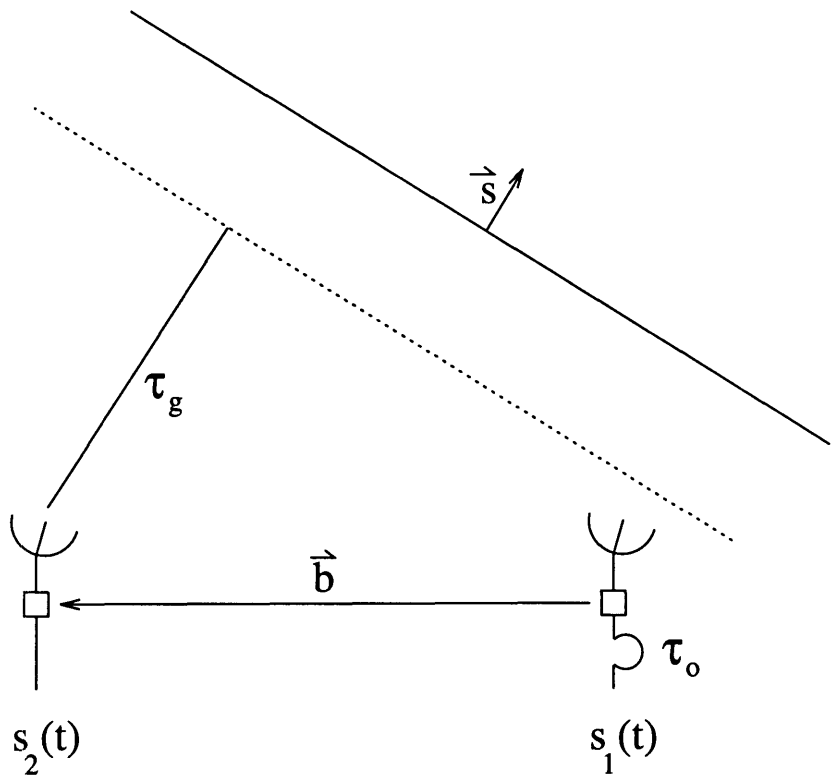

Figure 2-1: Diagram of the two element interferometer. $\vec{b}$ is the vector from antenna 1 to antenna 2, $\vec{s}$ is the direction to the source, τ_g is the geometric time delay, and τ_o is a delay introduced before correlation.

The effect of τ_o is to "point" the interferometer at a specific position in the sky $\vec{s}_o$, known as the delay center. Therefore, the signals received from both antennae are,

$$s_1(t) = \sqrt{S_o}\cos\omega(t-\tau_o) \tag{2.5}$$

$$s_2(t) = \sqrt{S_o}\cos\omega(t-\tau_g) \tag{2.6}$$

where ω is the observing frequency. Multiplying these signals together, we find,

$$V_R = \frac{S_o}{2}\left[\cos\omega(2t-\tau_g-\tau_o)+\cos\omega(\tau_g-\tau_o)\right] \tag{2.7}$$

Since we are interested in the relative phase of the incident emission, we keep only the latter term. As the Earth rotates, $\tau_g - \tau_o$ varies very slowly compared with the $2t-\tau_g-\tau_o$ term. Applying an appropriate low-pass filter, we obtain the correlated

signal,

$$V_R = S_o \cos\left(2\pi \vec{b}_\lambda \cdot (\vec{s} - \vec{s}_o)\right) \tag{2.8}$$

where $\vec{b}_\lambda$ is the baseline vector measured in wavelengths. We have scaled the response by a factor of two since half the correlated response has been filtered out. This response is a function of position $\vec{s}$ and effectively projects a sinusoidal function on the sky, known as "fringes". If the "fringe" pattern and source position are such that $\vec{b}_\lambda \cdot (\vec{s} - \vec{s}_o) = 1/4$, the correlated signal vanishes. These nulls in the response function can be easily moved by delaying the signal from telescope one by an additional $\pi/2\omega$, introducing a $\pi/2$ phase shift into the response function. Therefore, the response becomes,

$$V_I = S_o \sin\left(2\pi \vec{b}_\lambda \cdot (\vec{s} - \vec{s}_o)\right). \tag{2.9}$$

We remove the nulls in the response functions by combining both V_R and V_I to obtain the total complex response function to a point source,

$$V = S_o e^{2\pi i \vec{b}_\lambda \cdot (\vec{s} - \vec{s}_o)}. \tag{2.10}$$

To calculate the response to an extended source, we rely on the principle of superposition. For an interferometer, superposition states that the response to a sum of sources is the sum of the individual responses for each source. Since we can express the extended source as an integral of point sources, the response is an integral of point source response functions,

$$V\left(\vec{b}_\lambda\right) = \int I(\Omega) e^{2\pi i \vec{b}_\lambda \cdot (\vec{s}(\Omega) - \vec{s}_o)} d\Omega. \tag{2.11}$$

where $I(\Omega)$ is the brightness distribution of the extended source on the celestial sphere. We assume the individual antenna responses (primary beams) are constant over the source. This assumption is valid when the source size is small relative to the primary beam and the antenna elements track the source throughout the observation.

The interferometer response is not a two-dimensional Fourier transform of the source brightness distribution because $I(\Omega)$ is defined on the celestial sphere, not a

flat two-dimensional surface. By limiting our field-of-view to a region defined such that $d\Omega \approx d^2\vec{x}$, we approximate a small region of the sphere as a plane. This transformation projects the points on the celestial sphere onto a tangent plane, where the tangent point is $\vec{s}_o$. We express the relative source coordinates $\vec{s} - \vec{s}_o$ using a rectangular coordinate system defined such that the x-axis points towards local west and the y-axis points towards local north on the tangent plane. We use (u, v) for the baseline coordinates measured in wavelengths (i.e. $\vec{b}_\lambda = (u, v)$). In this coordinate system, we recover the Fourier transform relationship between the response and the two-dimensional brightness distribution,

$$V(u,v) = \int I(x,y) e^{2\pi i(ux+vy)} dx dy. \tag{2.12}$$

An interferometer measures the complex visibility function, which is the ratio of the correlated flux density $V(u, v)$ to the total flux density,

$$\Gamma(u,v) = \frac{\int I(x,y) e^{2\pi i(ux+vy)} dx dy}{\int I(x,y) dx dy}. \tag{2.13}$$

2.3 Aperture Synthesis

From Equation 2.13, we see that by measuring all the Fourier components of $I(x, y)$, we can reconstruct the brightness distribution simply by Fourier inversion,

$$I(x,y) = S_o \int \Gamma(u,v) e^{-2\pi i(ux+vy)} du dv \tag{2.14}$$

where S_o is the total flux of the source. In practice, we do not have measurements over the entire visibility plane since resources are limited. Radio interferometers exploit the rotation of the Earth to fill in the u-v plane. Since an interferometer has a finite number of antennae, the u-v plane is sampled at a small number of points $(u_{ij}(t), v_{ij}(t))$, each corresponding to a single baseline at a given time. As the Earth rotates, the orientation of a baseline changes, tracing out arcs in the u-v plane. If the source does not vary on the timescale on the observation, the entire

u-v track can be used to reconstruct the image. Each measurement along the track is an average of the true complex visibility function over a finite integration period. We assume the integration period is short such that the measured visibility is an accurate representation of the underlying true visibility. We address the effects of the averaging in section 2.4.2.

Consider an East-West baseline and a source directly north ($\delta = 90^o$). At a given time t, this baseline defines two u-v points: $(u_{12}(t), v_{12}(t))$ and $(-u_{12}(t), -v_{12}(t))$. For a continuous observation using an integration time τ_a, the rotation of the Earth causes the baseline to trace out a full circle over a 12 hour period, where half the circle is made up from $(u_{12}(t), v_{12}(t))$ and the other half is made up from $(-u_{12}(t), -v_{12}(t))$. This u-v track consists of samples separated by a distance,

$$\pi\sqrt{u_{12}^2(t) + v_{12}^2(t)}\left(\frac{\tau_a}{12 \text{ hrs}}\right). \tag{2.15}$$

In general, the projected baselines will traces out ellipses in the u-v plane.

An interferometer consisting of N stations measures $\Gamma(u,v)$ on $\frac{1}{2}N(N-1)$ baselines simultaneously. We can express the measured visibility $\Gamma^m(u,v)$ as the product of the true visibility $\Gamma(u,v)$ with a sampling function,

$$\Gamma^m(u,v) = \Gamma(u,v)S(u,v) \tag{2.16}$$

where the sampling function is,

$$S(u,v) = \sum_{k}^{N_t}\sum_{i,j}^{N} w_{ij}\delta(u - u_{ij}(t_k))\delta(v - v_{ij}(t_k)) \tag{2.17}$$

and N_t is the number of integration periods and w_{ij} are weighting factors to adjust the shape of the instrumental response function. The effect in the image plane is to convolve the true image by the instrumental response,

$$I^d(x,y) = I(x,y) \otimes B(x,y) \tag{2.18}$$

where $I^d(x,y)$ is the dirty image and the dirty beam $B(x,y)$ is the Fourier transform of the sampling function. Typically, the dirty beam contains many lower level peaks (referred to as "sidelobes") separated from the main central peak. For sparse arrays, the heights of the sidelobes can be a significant fraction of the height of the main central peak.

The resolution of the interferometer is characterized by the full-width at half-maximum (FWHM) of the dirty beam central lobe. The exact size and shape of the dirty beam depends on the distribution of visibility samples in the u-v plane and their weights, given by w_{ij}. In the absence of u-v tapering, the FWHM is approximately determined by the angular distance which causes a 2π phase rotation on the largest projected baseline $b_\perp$,

$$\theta_{FWHM} \simeq \frac{1}{b_{\lambda\perp}} \simeq \frac{\lambda}{b_\perp} \tag{2.19}$$

where λ is the observing wavelength. In A-configuration, the VLA has a maximum baseline length of $\simeq$ 40 km. Therefore, a $\lambda 2$ cm observation would have a minimum beam size of $\simeq$ 0.″1. We see that largest baseline length in an interferometer is analogous to the diameter of a filled aperture telescope in determining the resolving power of the instrument. Since we can reconstruct images of astronomical sources without measurements throughout the entire aperture, this technique is also known as aperture synthesis.

The weighting factors w_{ij} are used to modify the shape of the dirty beam. The two commonly used weighting schemes are natural weighting and uniform weighting (Sramek & Schwab 1989). Natural weighting applies the same weight to all the data points, yielding the highest signal-to-noise ratio. Since the shorter spacings spend more time in a given region per unit area, natural weighting tends to emphasis the short baselines and broaden the dirty beam, resulting in lower resolution. Uniform weighting assigns weights which are inversely proportional to the number of data points within a certain region,

$$w_{ij} = \frac{1}{N_{ij}} \tag{2.20}$$

where N_{ij} is the number of data points within a region centered on $\vec{u}_{ij}$. Typically, the

region is defined as a square box (referred to as a u-v box). The shorter baselines are more densely populated and thus down-weighted with respect to the longer baselines. The result is that uniform weighting has a smaller beam than the naturally weighted beam at the expense of a larger average sidelobe level.

2.4 Smearing Effects

2.4.1 Bandwidth Smearing

The discussion up to now has assumed a monochromatic signal. In practice, the source is broadband and measured across a finite bandwidth. The non-zero bandwidth has the effect of decorrelating the measured signals across the bandpass (Bridle & Schwab 1989). The response to a frequency-dependent brightness distribution, $I(x, y, \nu)$, is,

$$V(u,v) = \int \mathrm{d}x\mathrm{d}y \left[\frac{1}{\triangle\nu} \int_{\nu_o - \frac{1}{2}\triangle\nu}^{\nu_o + \frac{1}{2}\triangle\nu} \mathrm{d}\nu I(x,y,\nu) e^{2\pi i \vec{b}\cdot(\vec{s}-\vec{s}_o)\nu/c} \right] \tag{2.21}$$

where the bandpass is assumed to be rectangular, centered on ν_o, and has width $\triangle\nu$. If we assume the cosmic signals vary slowly with frequency across the bandwidth of the receiver, then the brightness distribution can be approximated as a constant function evaluated at the center frequency. Integrating over frequency, we find,

$$V(u,v) = \int \mathrm{d}x\mathrm{d}y I(x,y,\nu_o) e^{2\pi i \vec{b}_{\lambda_o}\cdot(\vec{s}-\vec{s}_o)} \left[\frac{\sin(\pi\tau\triangle\nu)}{\pi\tau\triangle\nu} \right] \tag{2.22}$$

where $\tau = \vec{b}\cdot(\vec{s}-\vec{s}_o)/c$. We see that the brightness distribution is multiplied by a sinc function, limiting the field-of-view. The amount of sky which can be mapped is given by when the sinc function reaches its first null,

$$\theta_{\triangle\nu} = \frac{c}{b_\perp \triangle\nu} \tag{2.23}$$

where $\theta_{\Delta\nu}$ is the width of "delay" beam and $b_\perp$ is the length of the projected baseline. The VLA has a bandwidth of 50 MHz resulting in a delay beam of $\simeq 30''$ for a maximum baseline length $\simeq 40$ km (A-array). If we examine the effect in the visibility plane, we see that the bandwidth corresponds to the radial width of the u-v tracks, which is integrated to yield the measured visibility point. If the visibility function varies rapidly over that width, then the measured visibility point does not accurately represent the true visibility function. In the measured image, the effect smears the source along the radial direction. The amount of smearing depends on the distance from the delay center in the sense that larger u-v distances correspond to larger distortions. Bandwidth smearing is serious because the effect modifies the convolving function to one which is a function of position on the sky. Deconvolution algorithms, such as CLEAN and NNLS (see section 2.5), assume the dirty beam is independent of position and will create spurious extensions due to this type of smearing.

2.4.2 Time-Average Smearing

Time-averaging of the visibilities causes an effect analogous to bandwidth smearing except in approximately the orthogonal direction (Bridle & Schwab 1989). Each measured point in the u-v plane is an average of the visibilities over some integration period. The (u, v) point assigned to the integration period is the midpoint of the integration interval along the u-v track. In exactly the same manner as bandwidth smearing, if the visibility function varies rapidly over the integration period, the integrated visibility will not be an accurate representation of the true underlying visibility value. Clearly, the longer baselines are more affected since, for a given integration time, they trace out a larger distance in the u-v plane (see Equation 2.15). Therefore, the time-average smearing effect is baseline dependent, resulting in a smearing of the dirty beam as a function of position.

Although this effect does not alter the flux detected in the image, the amplitudes in the image are reduced due to the smearing of the dirty beam. For a source which is a distance θ away from the phase center, the average fractional reduction in amplitude

for an integration interval of τ_a is,

$$\langle R_{\tau_a} \rangle = 1 - \frac{\alpha\pi^2}{12}\omega_e^2\tau_a^2\left(\frac{\theta}{\theta_{FWHM}}\right)^2 \tag{2.24}$$

where ω_e is the rotational frequency of the Earth, θ_{FWHM} is the half-power beam-width of the synthesized beam, θ is the offset of the source from the phase center, and α is a constant of order unity describing the details of the baseline distribution and tapering function used (Bridle & Schwab 1989). The amplitude of the smearing depends on the ratio of the source separation to the beam width and, therefore, affects VLBI observations more seriously. If we require that $\langle R_{\tau_a} \rangle \gtrsim 0.99$ for an averaging period of $\tau_a = 30$ s, the extent of the source must be $\lesssim 200\theta_{FWHM}$ in diameter.

2.5 Image Reconstruction

Radio interferometers use sparse arrays of antennae to achieve high-resolution observations of cosmic sources. The resulting dirty beam will contain sidelobes away from the main peak. The amplitude of those lobes is determined by the amount of the u-v plane which is filled during the observation. Equation 2.18 shows that the result of choosing these sparse configurations is that the measured image is strongly corrupted by the convolution with the dirty beam. Even for densely sampled VLA observations, significant sidelobes are present away from the central peak, introducing correlations between widely separated regions in the dirty image. In addition to these sampling effects, the measured visibilities are contaminated by errors in the observation. The primary sources of the errors are antennas-based, such as atmospheric and instrumental effects. Baseline-based errors are present due to errors such as correlator problems; however, we ignore these since these effects are usually far smaller than the antenna-based errors. For interferometers with $N > 3$ antennae, there are $N(N-1)/2 > N$ measured complex visibilities. Therefore, by constraining the errors to be antenna-based, we need only solve for N amplitude and N phase errors, given $N(N-1)/2$ complex constraint equations.

2.5.1 Self-Calibration

The noise is characterized by an amplitude and phase error for each antenna. Since these errors are due to effects such as clouds, they are allowed to vary with time. Let $\epsilon_i(t)$ be the multiplicative complex error associated with antenna i at time t. Then, the measured visibility on the baseline from antenna i to antenna j is,

$$V^m(\vec{u}_{ij}) = \epsilon_i(t)\epsilon_j^*(t)V(\vec{u}_{ij}) \tag{2.25}$$

Let $I^{model}(\vec{x})$ be a model of the true image. By Fourier transforming this model, we can directly compare the measured visibility with the predicted model visibilities $V^{model}(\vec{u})$. If a reference antenna is chosen to have zero error, the errors for all the other antenna can be solved for using the constraints,

$$\hat{\epsilon}_i(t)\hat{\epsilon}_j^*(t) = \frac{V^m(\vec{u}_{ij}(t))}{V^{model}(\vec{u}_{ij}(t))} \tag{2.26}$$

Since we have arbitrarily defined the zero point, the absolute position (phase) information is lost. The flux reference is preserved by requiring the mean amplitude correction to the visibilities be unity.

Since an *a priori* model of the source is rarely available, an iterative approach to image reconstruction is used to account for the effects of noise and discrete sampling. Self-calibration (Cornwell & Fomalont 1989) solves for a model of the true image and the antenna-based errors by applying consistency requirements on the data. At each iteration, the visibility data is Fourier transformed to create the dirty image. Deconvolution methods, such as CLEAN and NNLS, are used to reconstruct a model of the true image. Using Equation 2.26, the antenna-based errors are estimated and the visibilities are corrected by,

$$V_{corr}(\vec{u}_{ij}) = g_i(t)g_j^*(t)V^m(\vec{u}_{ij}) \tag{2.27}$$

where $g_i(t) = 1/\hat{\epsilon}_i(t)$ are the antenna gains. These iterations are repeated until a self-consistent solution for the gains and image is found. Typically, amplitude errors

in VLA observations are $\lesssim 2$ percent and not usually corrected. On the other hand, VLBI observations can have amplitude errors of 10 percent or more. The variations in the phase error are usually dominated by changes in the atmosphere and can exceed 2π.

This method of image reconstruction raises the question of uniqueness. In most cases, poor choices of the self-calibration or deconvolution parameters leads only to solutions in which the solution is not optimal. Only on rare occasions—extremely poor u-v sampling with very few antennae—has self-calibration produced multiple significantly different solutions (Cornwell & Fomalont 1989).

2.5.2 Deconvolution Algorithms

The choice of algorithm is important since the deconvolution techniques are not perfect and can introduce systematic errors into the reconstructions. Three deconvolution algorithms are in use in radio astronomy: CLEAN, NNLS, and MEM. The most frequently used algorithm is the CLEAN algorithm (Högbom 1974; Clark 1980; Schwab 1984), which is based on the assumption that sources can be decomposed into point sources. In order to implement CLEAN efficiently, each visibility point is convolved and sampled onto a $2^n \times 2^n$ grid in the u-v plane (typically referred to as "gridding"), so the Fast Fourier Transform (FFT) routine can be used. The u-v grid dimensions—both the cellsize and number of pixels—should be such that, in the image plane, the dirty beam is oversampled (i.e. the width of the dirty beam is $\gtrsim 3$ image plane pixels).

The normal implementation divides the procedure into the minor and major cycles. During the minor cycle, the algorithm finds the position and flux of the peak in the dirty image. At this position, the dirty beam is subtracted from the dirty image, scaled to a fraction (called the loop-gain) of the peak flux and a point source with the same flux is added to the clean map. The procedure is repeated until a stopping criterion is satisfied, typically when all the pixels are less than a fixed fraction of the dirty image peak at the start of the minor cycle. In the major cycle, the accumulated clean components collected in the previous minor cycle are subtracted from the ungridded

complex visibilities. When a specified number of clean components are subtracted or the maximum residual in the image is below a fixed value, the algorithm stops. The clean component model is used as the model for the true image structure in self-calibration. Since spatial frequencies much larger than those sampled by the longest baseline are not well constrained, we remove these frequencies through convolution before producing the final image. The convolving function (referred to as the clean or restoring beam) is a gaussian which is fit to the central lobe of the dirty beam. The clean image is created by convolving the final reconstructed image—the collection of clean components—with the clean beam. The residual image is added to include any flux which was not reconstructed in the deconvolution process.

A number of problems are intrinsic to this method of deconvolution. CLEAN is an inherently "local" algorithm in that each new clean component cannot alter any previously subtracted component. This independent nature leads to errors in both compact and extended structures. CLEAN subtracts from the peak of the dirty image, but due to noise and beam sidelobes, the peak is not the actual location of the underlying compact source. CLEAN compensates for the initial error by adding many nearby low level components. This behavior adds spurious "skirts" around bright components, and it is characteristic of CLEAN reconstructions of compact components. Another well-known problem affects extended sources, where CLEAN tends to subtract in periodic "stripes" with a period equal to the distance between the beam peak and the first negative sidelobe (see Cornwell 1983, for example).

Briggs (1994) has adapted the Non-Negative Least-Squares (NNLS) algorithm (Lawson & Hanson 1974) to the deconvolution problem. NNLS generalizes CLEAN to use a least-squares fit to the visibility data with a finite number of non-negative clean components. The algorithm constructs a model for the source by minimizing the mean-squared difference between the dirty image and the convolution of the source model with the dirty beam,

$$\varphi = \int \mathrm{d}^2\vec{x} \left(B \otimes I^{model}(\vec{x}) - I^d(\vec{x}) \right)^2 \tag{2.28}$$

where $I^{model}(\vec{x})$ is the model of the true source distribution. At each iteration, the model adds another component to the image, located at the pixel which produces the largest reduction in φ. The fluxes for all the components in the model, including the newly chosen component, are simultaneously optimized by minimizing φ in a least-squares sense with the requirement that all fluxes remain non-negative. The algorithm converges when adding components does not reduce φ or when all the pixels in the image have been included. As with CLEAN, the clean component model is used as the self-calibration model of the true image. To produce the final NNLS image, the components are convolved with the restoring beam and added to the residual image. The NNLS algorithm is "global" in the sense that the correlations between clean components are accounted for in the flux optimization step. NNLS also enforces positivity in the reconstructed source by constraining each pixel to be non-negative. The NNLS algorithm performs far better than CLEAN on partially resolved sources (Briggs *et al.* 1994), but NNLS is both a memory and time intensive calculation. It requires storage and inversion of a dense matrix with $N_d N_s$ entries, where N_d is the number of pixels in the dirty image and N_s are the number of source pixels in the reconstructed image. Since matrix inversion scales in time approximately as $\mathcal{O}(N_d N_s^2)$, this algorithm is only beginning to become computationally practical.

Unlike CLEAN and NNLS, the Maximum Entropy Method (MEM) (Narayan & Nityananda 1986, for example) does not represent the source as a collection of point sources. MEM attempts to reconstruct the image under the constraints that the model is positive, fits the visibility data, and maximizes the image "entropy". MEM performs well for sources with diffuse emission or simple structure, but poorly reconstructs compact sources embedded in extended emission (Cornwell & Fomalont 1989). The nature of the entropy function leads to reconstructions with edges only as sharp as the data requires. This "smoothness" constraint can cause spurious extensions in the reconstructed images of compact sources.

2.6 Very Long Baseline Interferometry

Historically, Very Long Baseline Interferometry has used isolated single-dish telescopes around the world as elements of a "global" interferometer. Differences in the atmospheric conditions and instrumentation at each site cause large differences in the amplitude and phase of the electric field recorded at each site. Furthermore, in contrast to the VLA, the independent time standards at each site are not phase-locked, so errors in the "clocks" corrupt the observed phases. These effects must be corrected before the data can be imaged.

2.6.1 Amplitude Calibration

To obtain correct amplitudes, the normalized visibilities are scaled by,

$$V(\vec{u}_{ij}) = b\sqrt{\frac{T_i^{sys}T_j^{sys}}{G_iG_j}}\Gamma(\vec{u}_{ij}) \tag{2.29}$$

where T_i^{sys} and G_i are the system temperature and gain of antenna i. The digitization losses are characterized by the parameter b. For 1-bit sampling, b is 1.57 (Thompson *et al.* 1986). The gains are computed using one of two sources: established gain curves or antenna temperature measurements. The first method relies on observations of calibration sources. In this context, a sufficient definition for the calibrator is a compact source of known flux. Many observations of these calibrators can be used to map out the gain of the station as a function of elevation. Most telescopes use altitude-azimuth mounts, so the gain is parameterized by only the elevation angle. Some stations, such as the NRAO 140 foot telescope in Greenbank, use polar mounts which require the gain to be a function of both hour angle and declination,

The second method relies on antenna temperature measurements taken during the course of the observation. The antenna temperature is a measure of the total power received due to the source. The measurement is performed by recording the response

of the antenna both on and off source,

$$T^{ant} = T^{sys}_{ON} - T^{sys}_{OFF} \tag{2.30}$$

This procedure, known as "on-offs", requires knowledge of the flux of the source of interest. The gain of the station i is then given by,

$$G_i = \frac{T^{ant}_i}{S} \tag{2.31}$$

2.6.2 Fringe Fitting

This discussion draws heavily from Schwab & Cotton (1983). When the antenna signals are correlated, a model of the visibility phase is subtracted. This correlator model accounts for the array geometry, atmospheric delays, and constant clock offsets. However, differences in the independent time standards along with uncertainties in the antenna positions and atmospheric propagation delays cause significant errors in the observed phase. Therefore, the VLBI signals are correlated with several different time lags between each station. The observations are also simultaneously recorded at several different frequencies. Let the observed visibility be $\Gamma^m_{ij}(f_k, \tau_l)$, where f_k is the kth frequency channel and τ_l is the lth correlator delay for baseline ij. We can Fourier transform $\Gamma^m_{ij}(f_k, \tau_l)$ into the time and frequency domain to obtain the observed cross-spectral function, $\tilde{\Gamma}^m_{ij}(t_k, \nu_l)$, which is related to the true cross-spectral function $\mathcal{V}_{ij}(t_k, \nu_l)$ by,

$$\tilde{\Gamma}^m_{ij}(t_k, \nu_l) = g_i(t_k, \nu_l) g^*_j(t_k, \nu_l) \mathcal{V}_{ij}(t_k, \nu_l) + \epsilon_{ijkl} \tag{2.32}$$

where the antenna-based errors are absorbed into the complex functions,

$$g_i(t_k, \nu_l) = a_i e^{i\psi_i(t_k, \nu_l)} \tag{2.33}$$

and the amplitude $a_i(t_k, \nu_l)$ is assumed to vary slowly compared to the antenna phase $\psi_i(t_k, \nu_l)$. The baseline-based error ϵ_{ijkl} is assumed to be small and neglected. We

can expand the observed visibility about (t_0, ν_0) to first order,

$$\begin{aligned}\tilde{\Gamma}_{ij}^{m}(t_k,\nu_l) \;\simeq\; & a_i a_j \mathcal{V}_{ij}(t_0,\nu_0)\exp\left\{i\left[(\psi_i-\psi_j)(t_0,\nu_0)\right]\right\} \\ & + \left\{ i\left[\left.\frac{\partial(\psi_i-\psi_j+\phi_{ij})}{\partial t}\right|_{(t_0,\nu_0)}(t_k-t_0) \right.\right. \\ & \left.\left. + \left.\frac{\partial(\psi_i-\psi_j+\phi_{ij})}{\partial \nu}\right|_{(t_0,\nu_0)}(\nu_l-\nu_0)\right]\right\} \end{aligned} \tag{2.34}$$

where ϕ_{ij} is the phase due only to the source brightness distribution. We define the fringe delay (or "delay") as,

$$\tau_{ij} = \left.\frac{\partial(\psi_i-\psi_j+\phi_{ij})}{\partial \nu}\right|_{(t_0,\nu_0)} \tag{2.35}$$

and the fringe rate (or "rate") as,

$$r_{ij} = \left.\frac{\partial(\psi_i-\psi_j+\phi_{ij})}{\partial t}\right|_{(t_0,\nu_0)}. \tag{2.36}$$

The delay is the difference in the clock errors and the rate is the difference in the derivative of the clock errors.

The traditional baseline-based method of fringe fitting solved for the delays and rates by Fourier transforming the distribution,

$$F_{ij}(t,\nu) = \sum_{kl}\delta(t-(t_k-t_0))\delta(\nu-(\nu_l-\nu_0))\tilde{\Gamma}_{ij}^{m}(t_k,\nu_l) \tag{2.37}$$

to obtain $\tilde{F}_{ij}(r,\tau)$ and searching for the maximum. The observed visibilities are then corrected by,

$$\tilde{\Gamma}_{ij}^{corr}(t_k,\nu_l) = \tilde{\Gamma}_{ij}^{m}(t_k,\nu_l)\exp\left\{-i\left[(t_k-t_0)r_{ij}+(\nu_k-\nu_l)\tau_{ij}\right]\right\} \tag{2.38}$$

where τ_{ij} and r_{ij} are the delay and rate solutions corresponding to the peak. Note that the antenna phase ψ_i is not removed, so the visibilities are corrected up to a constant phase offset for each antenna. However, since these offsets are antenna-based, they

are removed during self-calibration. The major drawback of this method is that the source must be strong enough on each visibility so that the delays and rates can be solved.

The global fringe fitting procedure has been developed to solve for all the delays and rates in an antenna-based framework similar to self-calibration (Schwab & Cotton 1983). We can define the antenna-based phase, delay, and rate by,

$$\begin{aligned} \psi_i &= \psi_i(t_0, \nu_0) \\ \tau_i &= \left.\frac{\partial \psi_i}{\partial \nu}\right|_{(t_0,\nu_0)} \\ r_i &= \left.\frac{\partial \psi_i}{\partial t}\right|_{(t_0,\nu_0)} \end{aligned} \tag{2.39}$$

where the delay and rate are no longer functions of the true phase of the source ϕ_{ij}. Let $\mathcal{V}_{ij}^{model}$ be a model of the true source visibility $\mathcal{V}_{ij}$. Global fringe fitting finds the set of antenna-based parameters such that,

$$\tilde{\Gamma}_{ij}^{m}(t_k, \nu_l) \simeq a_i a_j \mathcal{V}_{ij}^{model}(t_0, \nu_0) E_{ij,kl} \tag{2.40}$$

where all the antenna-based effects have been grouped into,

$$E_{ij,kl} = \exp\left\{i\left[(\psi_i - \psi_j) + (r_i - r_j)(t_k - t_0) + (\tau_i - \tau_j)(\nu_l - \nu_0)\right]\right\}. \tag{2.41}$$

Since the parameters enter only through pairwise differences, we define a reference antenna which has zero error (i.e. $\psi_{ref} = r_{ref} = \tau_{ref} = 0$).

Since we are interested only in the visibility phase, we assume the model amplitudes are equal to the calibrated amplitudes. In other words, we assume that after dividing the data $\mathcal{V}^m$ by the model $\mathcal{V}^{model}$, the result is a complex phase $e^{i(\tilde{\phi}-\phi^{model})}$, where $\tilde{\phi}$ is the observed visibility phase and ϕ^{model} is the phase of $\mathcal{V}^{model}$. Consider the distribution for a baseline from antenna 1 to antenna 2,

$$F_{12}(t,\nu) = \sum_{kl} \delta(t - (t_k - t_0))\delta(\nu - (\nu_l - \nu_0)) \exp\left\{i\left[(\tilde{\phi}_{12}(t_k, \nu_l) - \phi_{12}^{model}(t_k, \nu_l))\right]\right\} \tag{2.42}$$

If we choose antenna 1 as the reference antenna ($\psi_1 = r_1 = \tau_1 = 0$), then by Fourier transforming $F_{12}(t,\nu)$ and searching for the peak, we can solve for r_2 and τ_2. In addition, the phase of $F_{12}(t,\nu)$ gives ψ_2. For antennas 1, 2, and 3, we can define the closure relation,

$$\tilde{\phi}_{12} - \phi_{12}^{model} = (\tilde{\phi}_{13} - \phi_{13}^{model}) - (\tilde{\phi}_{23} - \phi_{23}^{model}) \tag{2.43}$$

and, therefore, solve for the parameters for antenna 3. Then, the closure relations for antennas 2, 3, and 4 can be used to find the antenna 4 parameters, and so forth until all the antenna parameters have been determined. This algorithm reduces the requirement that all the baselines have signal-to-noise ratios large enough to solve for the delays and rates to the requirement that at least one baseline to each antenna have a large signal-to-noise ratio. Moreover, since the problem is solved assuming antenna-based effects, the closure relations cannot be corrupted through this procedure.

The global fringe fitting algorithm implemented within the AIPS data reduction system incorporates the information from multiple baselines to a single antenna rather than the single baseline function $F_{12}(t,\nu)$, giving better parameter estimates (Cotton & Schwab 1993; Rogers 1993a; Rogers 1993b).

Chapter 3

Gravitational Lensing and Lens Inversion

3.1 Gravitational Lens Theory

Gravitational lensing occurs when the light rays from a distant source are deflected by an intervening massive object. The effects of the gravitational potential are adequately described in the weak field limit of general relativity (Refsdal 1964). Since the distances between the lens, object, and observer are a significant fraction of the universe and the interaction region is approximately given by the size of a galaxy, we can describe the system using the thin lens approximation. The photons are unaffected until they reach the lens, at which point, their trajectories are abruptly changed by a two-dimensional surface mass density. This scenario is illustrated in Figure 3-1.

Assuming small angles, we derive the lens equation,

$$\vec{\beta} = \vec{\theta} - \frac{D_{LS}}{D_{OS}}\vec{\alpha}_t \tag{3.1}$$

where D_{ij} is the angular diameter distance from point i to point j $(i < j)$ (Weinberg 1972). The positions vectors $\vec{\theta}$ and $\vec{\beta}$ are two-dimensional vectors defined in the lens (image) plane and the source plane, respectively. The lensing equation describes the mapping from the image plane $\vec{\theta}$ to the source plane $\vec{\beta}$. For a point source of

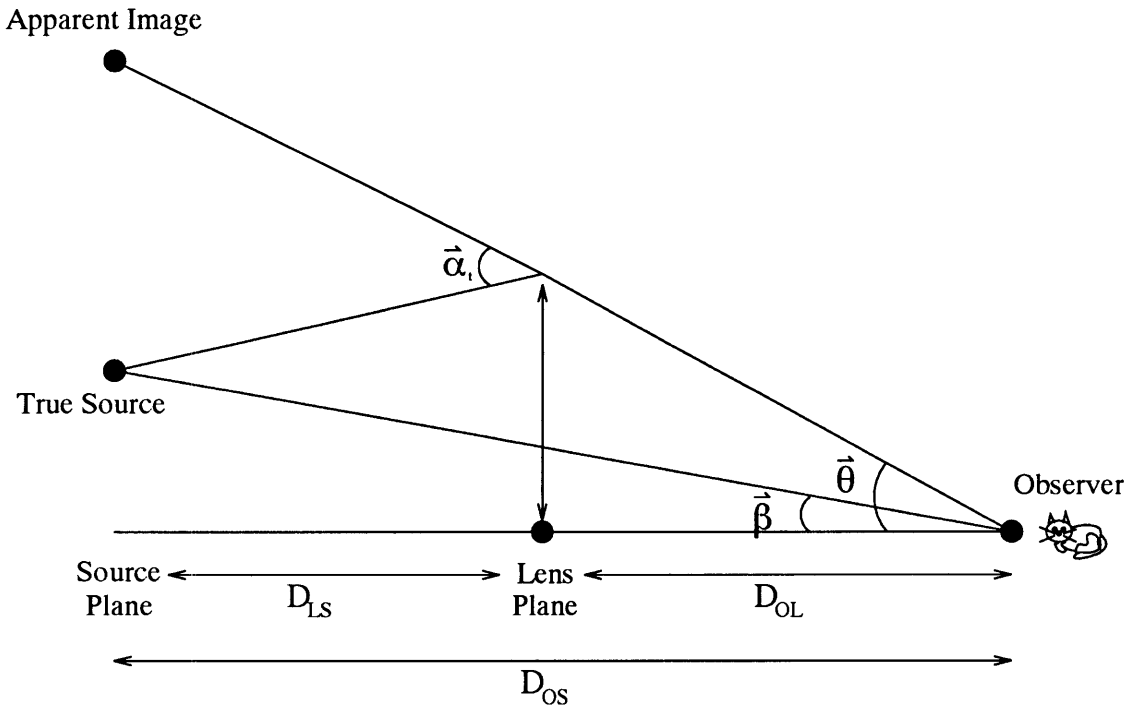

Figure 3-1: Gravitational lens diagram. The path of a single light ray is drawn. D_{ij} is the angular diameter distances from point i to point j, $\vec{\theta}$ is the angular position of the image (apparent source), $\vec{\beta}$ is the angular position of the source in the absence of a lens, and $\vec{\alpha}_t$ is the deflection angle.

mass M, the deflection angle is given by (Schneider *et al.* 1992),

$$\vec{\alpha}_t = \frac{4GM}{c^2 D_{OL}} \frac{\vec{\theta}}{|\vec{\theta}|^2}. \tag{3.2}$$

Using superposition, we extend this definition to find the deflection due to distributed mass,

$$\vec{\alpha}_t = \frac{4G}{c^2 D_{OL}} \int \mathrm{d}^2\vec{\theta}' \Sigma(\vec{\theta}') \frac{(\vec{\theta} - \vec{\theta}')}{|\vec{\theta} - \vec{\theta}'|^2} \tag{3.3}$$

where $\Sigma(\vec{\theta}')$ is the surface mass density of the lens. The two dimensional gravitational potential due to $\Sigma(\vec{\theta}')$ is,

$$\phi_t\left(\vec{\theta}\right) = \frac{4G}{c^2} \int \mathrm{d}^2\vec{\theta}' \Sigma(\vec{\theta}') \ln|\vec{\theta} - \vec{\theta}'|. \tag{3.4}$$

Beginning with the gravitational potential, we can invert Equations 3.3 and 3.4

to recover the deflection angle,

$$\vec{\alpha}_t = \nabla_{D_{OL}\theta}\phi_t \equiv \frac{1}{D_{OL}}\frac{\partial\phi_t}{\partial\vec{\theta}} \tag{3.5}$$

and the mass distribution,

$$\nabla^2_{D_{OL}\theta}\phi_t = 4\pi G\Sigma(\vec{\theta}). \tag{3.6}$$

To remove the dependence on the distances, we define dimensionless counterparts for the potential,

$$\phi = \frac{D_{LS}}{D_{OL}D_{OS}}\phi_t \tag{3.7}$$

and deflection angle,

$$\vec{\alpha} = \frac{D_{LS}}{D_{OS}}\vec{\alpha}_t = \nabla_\theta\phi \tag{3.8}$$

so the lens equation becomes,

$$\vec{\beta} = \vec{\theta} - \vec{\alpha}. \tag{3.9}$$

The Laplacian of the dimensionless potential yields twice the surface mass density in units of the critical density,

$$\nabla^2_\theta\phi = 2\frac{\Sigma(\vec{\theta})}{\Sigma_c} \tag{3.10}$$

where $\Sigma_c = c^2 D_{OS}/4\pi G D_{OL} D_{LS}$.

For cosmological lenses, the distances between the observer, lens, and source extend over large fractions of the observable universe. Therefore, the curvature of the universe must be taken into account. In a Friedmann cosmology with $\Lambda = 0$, the angular diameter distance between a point at redshift z_i and a point at redshift z_j ($z_i < z_j$) is,

$$D_{ij} = \frac{2c}{H_o}\frac{(1-\Omega_o)(G_i - G_j) + (G_i G_j^2 - G_i^2 G_j)}{\Omega_o^2(1+z_i)(1+z_j)^2} \tag{3.11}$$

where $G_i = \sqrt{1+\Omega_o z_i}$, H_o is Hubble's constant, and Ω_o is the ratio of the density of the universe to the critical density (Blandford & Narayan 1992). The Friedmann cosmology assume the universe is homogeneous and isotropic. On the distance scales which we are interested, approximately a gigaparsec, the universe appears uniform

and is approximately described by a Friedmann cosmology (Seljak 1995). The Dyer-Roeder equation can be used to determine the angular diameter distance as a function of redshift in a universe with gravitationally bound objects (Dyer & Roeder 1973; Schneider *et al.* 1992). This equations assumes that some fraction of the mass in the universe has coalesced into gravitationally bound objects, all of which are far from the bundle of light rays of interest.

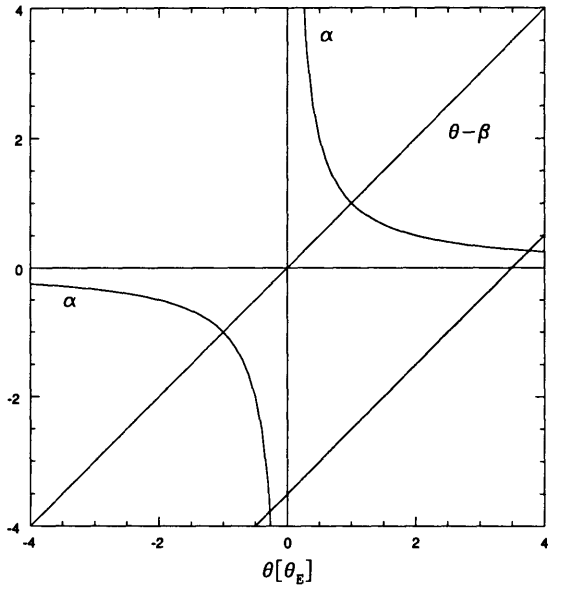

Figure 3-2: The deflection angle diagram for a point lens of mass M. The axes are in units of the "Einstein" ring radius.

The characteristics of a lensing system can be seen by plotting $\vec{\alpha}$ and $\vec{\theta} - \vec{\beta}$ as functions of impact parameter $\vec{\theta}$. The image positions are found at the points where the two curves intersect. Figure 3-2 shows the lensing behavior for a point mass lens. Since $\vec{\theta}$ is a two-dimensional vector and the mass distribution has circular symmetry, we only plot the $\vec{\theta}$ at a given position angle. The diagonal lines correspond to $\vec{\theta} - \vec{\beta}$ for different values of $\vec{\beta}$. It is clear that for any $\vec{\beta}$, there are two and only two images. For large $\vec{\beta}$, one image lies near the source position and one image lies near the lens center. For smaller values of $\vec{\beta}$, the two images tend towards the same distance from the lens center. Since this lens model is axially symmetric, a point source directly

behind the lens will be imaged into an "Einstein" ring with a radius,

$$\theta_E = \sqrt{\frac{4GM}{c^2}\frac{D_{LS}}{D_{OS}D_{OL}}}. \tag{3.12}$$

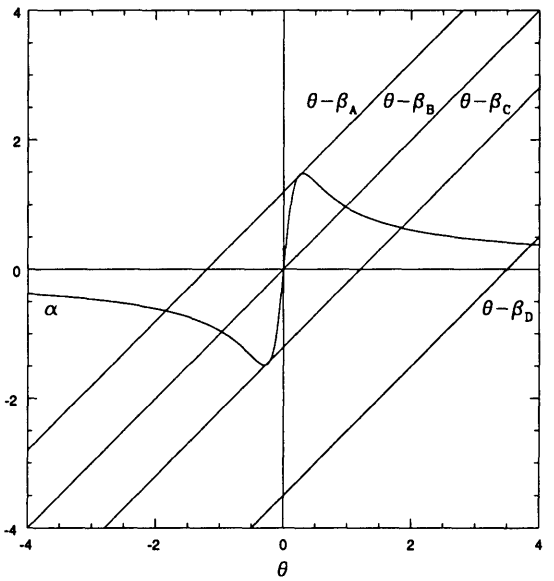

Figure 3-3: The deflection angle diagram for a general lens with circular symmetry.

For a general lens with circular symmetry, the deflection angle does not diverge at small values of $\vec{\beta}$. Figure 3-3 shows a deflection angle diagram for an extended lens and four source positions: $\vec{\beta}_A$, $\vec{\beta}_B$, $\vec{\beta}_C$, and $\vec{\beta}_D$. As θ becomes large compared to the size of the lens, the mass distribution is more accurately approximately by a point mass. Therefore, far from the lens, $\vec{\alpha}$ falls off as θ^{-1}. The behavior of $\vec{\alpha}$ for small impact parameters depends on the exact mass distribution in the lens. The source positions $\vec{\beta}_A$ and $\vec{\beta}_C$ define the boundary of the multiply-imaged region for this lens. Within this region, each source maps into three images, corresponding to the three points of intersection. Curve $\vec{\theta} - \vec{\beta}_B$ describes a source directly behind the lens center which is lensed into three images, one of which is located at the lens center. We see from the steep rise in the deflection function, any multiply-imaged source will have one image near the lens center. As a source crosses from the triply-imaged region to

the singly-image region, two of its images merge together and disappear. Although the more distant sources, such as $\vec{\beta}_D$, are shifted and distorted, they do not map to multiple positions in the image plane. We see that a circularly symmetric lens can produce at most three images. Hence, the observed lens systems, such as MG0414, require the lens with at least a monopole and quadrupole moment.

The magnification of each image can be found by considering the effect of the lens on a bundle of light rays emanating from the source. In the absence of the lens, the received flux from a source of surface brightness I_ν is $I_\nu d\Omega$, where $d\Omega$ is the solid angle subtended by the source. Since gravitational lensing conserves surface brightness, the magnification is due solely to the distortion of the solid angle,

$$\mu = \frac{d\Omega_{lens}}{d\Omega} \tag{3.13}$$

where $d\Omega_{lens}$ is the solid angle subtended by the distorted image. We describe the undistorted area as a function of the distorted area using the mapping given by the lens equation (Equation 3.9),

$$d\Omega = \left|\frac{\partial\vec{\beta}}{\partial\vec{\theta}}\right| d\Omega_{lens} \tag{3.14}$$

where $||$ indicates the determinant. Therefore, the magnification is,

$$\begin{aligned} \mu &= \left|\frac{\partial\vec{\beta}}{\partial\vec{\theta}}\right|^{-1} \\ &= \left|\mathcal{I} - \frac{\partial\vec{\alpha}}{\partial\vec{\theta}}\right|^{-1} \end{aligned} \tag{3.15}$$

where $\mathcal{I}$ is the identity matrix. In a frame where the magnification matrix,

$$\mathcal{M} = \left[\frac{\partial\vec{\beta}}{\partial\vec{\theta}}\right]^{-1} \tag{3.16}$$

is diagonal, the magnification is simply,

$$\mu = \begin{vmatrix} \lambda_1 & 0 \\ 0 & \lambda_2 \end{vmatrix} = \lambda_1 \lambda_2 \tag{3.17}$$

where λ_i is the ith eigenvalue of $\mathcal{M}$. For typical quasar-galaxy lens systems, the average magnification is ~ 10. If the magnification is negative, then the distortions include a reflection through the axis corresponding to the negative eigenvalue. In this case, the image is said to have "negative" parity. A positive magnification means the image has "positive" parity.

The magnification of a point source is,

$$\mu_{\pm} = \frac{1}{4}\left[\sqrt{\frac{\beta^2}{\beta^2 + 4\theta_E^2}} + \sqrt{\frac{\beta^2 + 4\theta_E^2}{\beta^2}} \pm 2\right] \tag{3.18}$$

where the + solution corresponds to the image on the same side as the source and the − solution corresponds to the image on the other side of the lens (Schneider *et al.* 1992). As the source positions grows large, the magnification of the + image approaches unity and the − image dims to zero. As $\beta \to 0$, the magnification diverges and at $\beta = 0$ the source is distorted into an entire ring.

For a general elliptical lens, the magnification is infinite at two loci of points in the source plane. Each curve corresponds to locations where one of the eigenvalues of the magnification matrix diverges. These curves (or "caustics") define regions in the source plane which are mapped into regions in the image plane with different numbers of images. Figure 3-4a show the caustics for a generic non-singular elliptical lens. The outer (or "radial") caustic separates the 1 and 3 image region, and the inner diamond-shaped (or "tangential") caustic separates the 3 and 5 image region. We can map the caustics to "critical lines" in the image plane, shown in Figure 3-4b. The radial caustic maps to the inner critical line and the tangential caustic maps to the outer critical line. The □, •, and × symbols represent different lensing configurations with one, three, and five images. In the source plane, the symbols represent the sources relative to the caustics, and, in the image plane, the symbols represent the

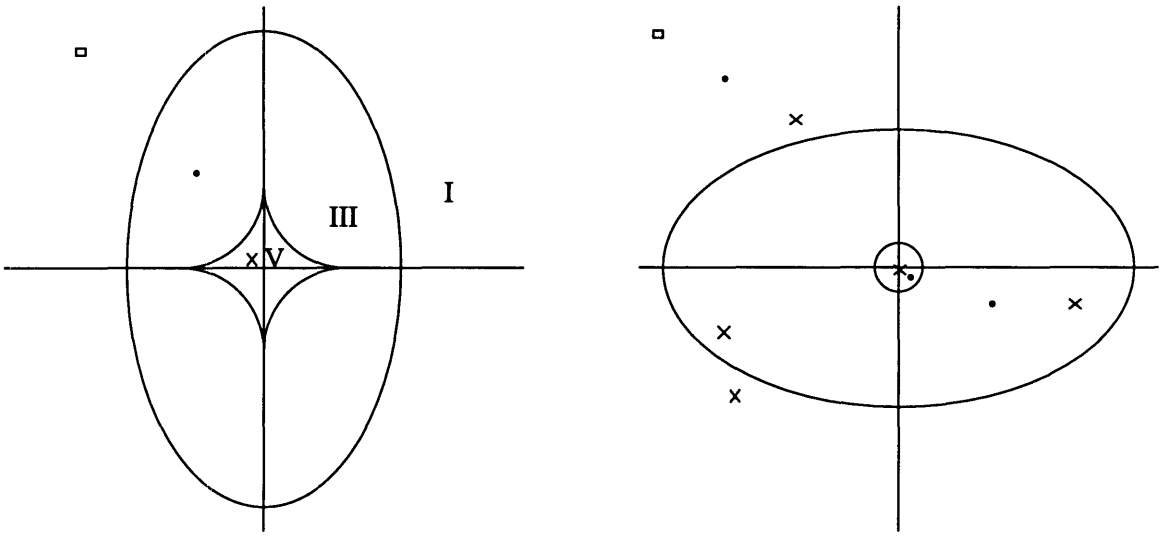

Figure 3-4: The caustics and critical lines for a strong non-singular elliptical lens. Panel (a) shows the source plane caustics. Panel (b) shows the image plane critical lines. The □, •, and × symbols represent sources in the one, three, and five image regions, respectively.

positions of all their associated images. The three-image configuration (•) is seen in lens systems like 0957+561, and the five-image configuration (×) are seen systems such as MG 0414+0534 and PG 1115+080 (Weymann *et al.* 1980). We see that the "odd" image is always located near the lens center, given by the origin in Figure 3-4. The magnification of this image depends strongly on the size of the core radius in the sense that a smaller core radius corresponds to a fainter "odd" image (see Section A.2). The lack of "odd" images in many observed lensing systems indicate that galaxies tend to have small or zero core radii.

An important observation quantity is the time delay between the images in a multiply-imaged system. For a single light ray, the lens delays the arrival time at the observer by,

$$T\left(\vec{\theta},\vec{\beta}\right) = \left(\frac{1+z_L}{c}\right)\left(\frac{D_{OL}D_{OS}}{D_{LS}}\right)\left[\frac{1}{2}\left(\vec{\theta}-\vec{\beta}\right)^2 - \phi\left(\vec{\theta}\right)\right] + \text{constant} \qquad (3.19)$$

with respect to the arrival time in the absence of the lens (Schneider *et al.* 1992), where z_L is the redshift of the lens and c is the speed of light. The two contributions to the elapsed time are due to the geometric path length and gravitational potential of the lensing galaxy. The deflection of the photons extends the length of the trajectories needed to reach the observer. The photons also traverse through the gravitational potential of the lens which leads to a contribution through time dilation. The difference in arrival times between two images of a common source is,

$$\Delta t_{12} = \left(\frac{1+z_L}{c}\right)\left(\frac{D_{OL}D_{OS}}{D_{LS}}\right)\left\{\frac{1}{2}\left[\left(\vec{\theta}_1-\vec{\beta}\right)^2-\left(\vec{\theta}_2-\vec{\beta}\right)^2\right]-\left[\phi\left(\vec{\theta}_1\right)-\phi\left(\vec{\theta}_2\right)\right]\right\}. \tag{3.20}$$

This relationship includes an overall distance scale for the system, $D = D_{OL}D_{OS}/D_{LS}$. Using Equation 3.11, we find,

$$D = \frac{2c}{H_o}\frac{(1-\Omega-G_L)(1-G_L)(1-\Omega-G_S)(1-G_S)}{\Omega^2(1+z_L)(1-\Omega-G_LG_S)(G_L-G_S)} \tag{3.21}$$

where $G_i = \sqrt{1+\Omega z_i}$. If the system is described reasonably well by a lens model, Hubble's constant can be found by measuring the time delay between images.

3.2 Lens Inversion

The lens inversion problem is one of reconstructing the lens and unlensed source from the distorted image. In general, reconstructing the underlying source altered by some corrupting medium is not possible. In gravitational lens systems, the multiple imaging effect adds stringent constraints allowing both the lens mass distribution and source brightness distribution to be recovered.

A simple "point solver" algorithm for lenses with compact sources assumes all the images map back to a common point in the source plane. The lens is parameterized and used to map each image back to the corresponding source point. The lens parameters are determined by minimizing the discrepancy in the source positions and fluxes. This procedure is straightforward in that the modeling constraints are obvious, i.e. requiring the images map back to a common source point. However, most

lens systems have some extended emission, which we would like to incorporate into the lens model. The problem lies in defining the constraints on the modeling, since we usually do not know in advance which regions in the image are correlated through the lens. In addition, the finite resolution of real observations compromises the lens reconstruction, since the image pixels do not represent the underlying image.

Kochanek & Narayan (1992) developed the LensClean algorithm as a general tool for inverting gravitational lens systems in the presence of finite resolution and noise. LensClean determines both the lens model parameters and source structure simultaneously using an optimization procedure. LensClean deconvolves the image assuming some lens model to determine the residual error in the fluxes due to inconsistencies between the data and the lens model. The error is minimized by adjusting the lens model parameters. The LensClean algorithm uses the CLEAN algorithm (Högbom 1974; Clark 1980; Schwab 1984), modified to include the distorting effects of the lens galaxy. Since the lens completely determines the image of a given source, LensClean iteratively reconstructs the unlensed source and compares the distorted image of that source with the observed data. In a manner identical to CLEAN, LensClean constructs the source from a collection of point sources (clean components).

The image of a source plane clean component $\mathcal{S}$ will consist of N distorted copies of $\mathcal{S}$ at positions $\vec{x}_k$ with magnifications M_k. After subtracting the clean component from the image, the mean square residual is,

$$\epsilon^2 = \int \mathrm{d}^2\vec{x} \left[I^d(\vec{x}) - f \sum_{k=1}^{N} |\mu_k| B(\vec{x} - \vec{x}_k) \right]^2 \tag{3.22}$$

where f is the source plane flux of $\mathcal{S}$. By requiring that ϵ^2 be minimized with respect to f and $\vec{x}_k$, the optimum position for $\mathcal{S}$ is given when,

$$\frac{\left[\sum_k^N |\mu_i| (I \otimes B)(\vec{x}_k)\right]^2}{\sum_i^N \sum_j^N |\mu_i||\mu_j| (B \otimes B)(\vec{x}_i - \vec{x}_j)} \tag{3.23}$$

is maximized and the optimum flux at that position is,

$$f = \frac{\sum_{k=1}^{N} |\mu_k| (I \otimes B)(\vec{x}_k)}{\sum_{i=1}^{N} \sum_{j=1}^{N} |\mu_i||\mu_j| (B \otimes B)(\vec{x}_i - \vec{x}_j)}. \tag{3.24}$$

In the absence of a lens, the optimum component is the peak of the dirty image, and LensClean reduces to the normal CLEAN algorithm.

For a fixed lens model, LensClean iteratively subtracts clean components from the dirty image. Unlike CLEAN, LensClean will not be able to subtract all the flux from the image because of inconsistencies between the measured data and reconstructed image assuming a lens model. During the cleaning stage, LensClean monitors the peak residuals after each major cycle. If the peak does not decrease by more than one percent from the last major cycle, LensClean assumes the cleaning cycle has converged. Errors in the lens model will create errors in the final residual image. Therefore, LensClean uses the dispersion in the residual image as a measure of the goodness of fit.

Each iteration of LensClean requires a knowledge of all positions and magnifications of the image plane clean components which map to the same source component, i.e. a solution to the nonlinear lens equation. Kovner (1987) showed that the quadrupole lens models produce the same image configurations and are much simpler to handle than truly elliptical lens models. Therefore, the lens models implemented in LensClean include only the monopole and quadrupole moments. At least five parameters are required to specify this type of lens. Two position parameters are needed to specify the lens center. One parameter is needed to specify the overall mass (or critical radius) of the lens. The quadrupole terms requires at least one parameter for its strength and one parameter for its orientation.

LensClean optimizes the lens model by minimizing the residuals as a function of the lens model parameters, using the "downhill simplex method" (Press *et al.* 1988; Nelder & Mead 1965). The "error surface" is the minimized rms residual as a function of the lens position. In other words, the "error surface" is found by minimizing all the parameters except the lens position. Typically, the "error surface" is corrupted

by systematic errors and noise, creating a lumpy texture. We outline the following optimization procedure to prevent converging within a local minimum.

If we fix the value of the lens position, the critical radius and quadrupole parameters are well constrained because of the four image geometry in MG0414. Therefore, we grid search over plausible lens positions (near the center of the lensing system). At each point (lens position) in the grid, we use a "point solver" algorithm to determine starting values for the critical radius and quadrupole parameters. Then, we optimize only these parameters keeping the lens position (and possibly other parameters such as core radius) fixed. We manually examine the "error surface" to find the location of the global minimum. Then, we perform a full minimization allowing all the parameters including lens position to vary with the starting point of the optimization near the global minimum.

3.3 Clean map LensClean

Although the LensClean algorithm is designed to account for both deconvolution and gravitational lens effects, this method has only been applied to clean maps and beams. We refer to this implementation as the Clean map LensClean (CLC) algorithm. This approach is computationally simpler because it manipulates the final images instead of the visibility data, thereby eliminating problems such as gridding and assigning weights to the visibilities. The gaussian restoring beam is significantly smaller than the dirty beam, reducing the computation time for the minor cycle subtractions. CLC does, however, assume that the systematic errors in the reconstructed clean maps do not impact the lens modeling results.

The goodness-of-fit of the lens model is measured by comparing the rms residual in the multiply-imaged region to that of noise multiplied by the size of the multiply-imaged region in beam areas (Kochanek 1995),

$$\chi^2_{clc} = N_{mul} \frac{\triangle x^2}{2\pi\sigma_b^2} \left(\frac{\sigma_{mul}}{\sigma_o}\right)^2 \tag{3.25}$$

where N_{mul} and σ_{mul} are the number of pixels of linear size $\triangle x$ and rms residual in the multiply-imaged region, respectively. The area of a beam is $2\pi\sigma_b^2$ and σ_b =FWHM[1]$/\sqrt{8\ln 2}$. The noise in the data σ_o is estimated by the rms value in empty regions of the image. The error estimate should be limited to the multiply-imaged region, since the singly-imaged region contains no extra degrees of freedom (Wallington & Kochanek 1995; Kochanek 1995). Since the χ^2 surface near the minimum may be dominated by systematic errors, a conservative scheme is used to determine the confidence levels on the parameters. First, to offset any overall systematic bias, the χ^2 surface is rescaled such that the minimum corresponds to the number of degrees of freedom, approximately given by the number of beams which fit within the tangential critical line minus the number of parameters required by the lens model (Kochanek 1995),

$$N_{dof} = \frac{A_{tan}}{2\pi\sigma_b^2} - M. \tag{3.26}$$

Second, the confidence level on a parameter is defined as the largest variation of that parameter from the best fit value with $N_{dof}\left(\chi^2 - \chi^2_{min}\right)/\chi^2_{min} \leq 15.1$, normally corresponding to the 99.99 percent confidence level. However, Kochanek (1995) suggests that the parameter limits should be conservatively interpreted as 95 percent confidence levels to compensate for the unknown systematic errors in the inversion procedure.

The final reconstructed image from LensClean is obtained by convolving the clean components with a gaussian restoring beam. If the lens model fits the data then the residual image contains only noise. However, if the model does not fit perfectly, the residuals are the noise plus the difference between the observed data and the reconstruction. Therefore, we do not add the residuals to the final image.

[1]FWHM is the Full-Width at Half-Maximum of the restoring (CLEAN) beam.

3.4 Negative Clean Components

The LensClean algorithm has originally been implemented with the freedom to subtract both positive and negative clean components, in the same fashion as CLEAN. LensClean treats each clean component as representing a small region of the source. Hence, in the multiply-imaged region, each subtraction removes all images of the source plane clean component. In the course of modeling the lens in MG0414, we found this freedom leads to non-physical solutions. In other words, the converged lens model requires the source brightness distribution contain negative flux.

Using the singular isothermal sphere (SIS) plus external shear model (see Section A.1), we modeled the MG0414 system with the CLC algorithm. We optimized the lens model parameters to fit the CLEAN image from the 15 GHz VLA observations (Katz & Hewitt 1995), shown in Figure 3-5. We followed the minimization

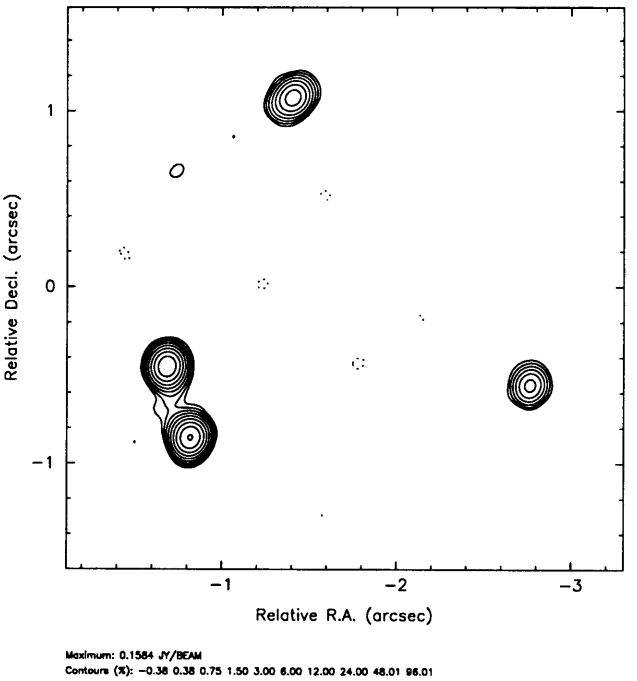

Figure 3-5: Final CLEAN image of MG 0414+0534 from a 15 GHz VLA observation of MG 0414+0534 (Katz & Hewitt 1995) used in the Clean map LensClean analyses. The contour levels are -1.5, -0.75, -0.375, 0.375, 0.75, 1.5, 3, 6, 12, 24, 48 and 96 percent of the peak, 158.4 mJy/Beam. The beam FWHM is 0.″12 by 0.″11.

procedure described in Section 3.2. Figure 3-6 shows the residual image using the best fit lens model. We find $\sigma_{mul} = 215$ μJy/Beam and a peak residual of 2.0 mJy/Beam.

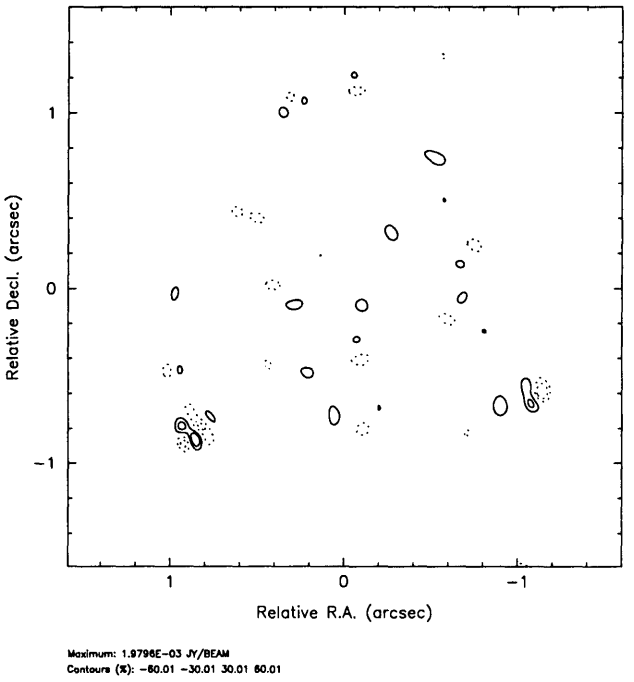

Figure 3-6: Residual Map from Best Fit SIS plus external shear model using the Clean map LensClean method including negative clean components. The absolute contour levels are the same as Figure 3-5.

From VLA monitoring of MG0414, Moore & Hewitt (1995) find variability in the system at the level of a few percent. Since there is a time delay between the arrival times between each image, we expect the variability to lead to deviations from the true flux ratios and to prevent LensClean from finding a perfect fit. LensClean constructs the source brightness distribution and attempts to fit the observed data such that the mean square residual is minimized. Therefore, LensClean minimizes the error in the source plane weighted by the image magnifications.

Consider a two-image gravitational lens where the source is unresolved. If the source is variable and the time delay is non-zero, then the mean square value in the image is,

$$\langle x^2 \rangle = [\mathcal{F}(t)\mu_1]^2 + [\mathcal{F}(t + \Delta t)\mu_2]^2 \tag{3.27}$$

$$= [\mathcal{F}_t\mu_1]^2 + [(\mathcal{F}_t + \delta\mathcal{F})\mu_2]^2 \tag{3.28}$$

where $\mathcal{F}_t$ is the source plane flux at time t and $\delta\mathcal{F}$ is change in the source plane flux from time t to $t + \triangle t$. We assume that we know the exact lens model for the system. If we subtract a source plane component of flux $\mathcal{F}_t$ from the data, the mean square residual in the image is,

$$\epsilon^2 = (\delta\mathcal{F}\mu_2)^2. \tag{3.29}$$

However, if we subtract a component of flux $\mathcal{F}_t + \delta\mathcal{F}$, the mean square residual is,

$$\epsilon^2 = (\delta\mathcal{F}\mu_1)^2. \tag{3.30}$$

If $\mu_1 > \mu_2$, the smallest residual is achieved by subtracting a component equal to the image plane flux of component 1 divided by its magnification ($\mathcal{F}_t$). However, if $\mu_1 < \mu_2$, the optimal source flux is the flux at component 2 divided by μ_2 ($\mathcal{F}_t + \delta\mathcal{F}$). Therefore, we see that the optimal flux for the subtracted component is determined by the flux of the highest magnification component. The time delay between A1 and A2 is short ($\approx$ 1 day), so the measured A1/A2 flux ratio in the image should be very close to the true flux ratio. Therefore, the dominant error in the modeling should be located at component B. At 15 GHz, the total flux of B is $\simeq$ 65 mJy. At a variability level of a few percent, we would then expect peak-to-peak errors of $\gtrsim$ 2 mJy/Beam for a perfect lens model inversion. From the residual image, we find the peak errors in the CLC inversion at components A1 and not at A1 or B indicating variability was not limiting the fit.

We found a problem in the solution from examining the distribution of clean components, shown in Figure 3-7. We see that to the west of B, there is a concentration of clean components in a region with no observed flux. The clean components are arranged such that the large positive and negative components cancel when convolved with the beam, resulting in no net flux in the image. We mapped these components through the lens to find their associated components in the image and found that they map to A1, A2, and C. This behavior is more clearly understood using the multiplicity

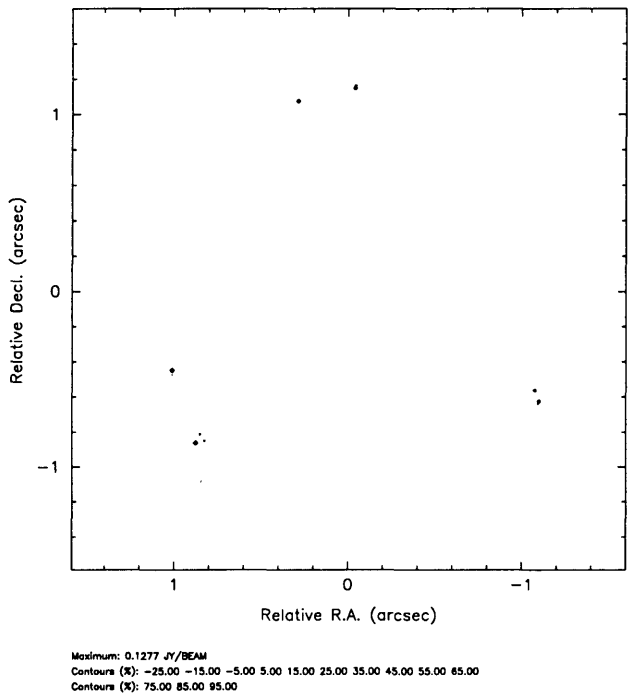

Figure 3-7: Distribution of clean components used in the best fit SIS plus external shear model using the Clean map LensClean method including negative clean components.

image (Figure 3-8). Each pixel in the image maps back to a single source position. If the source is within the multiply-imaged region, then more than one image pixel will trace back to that same location. The multiplicity image gives the number of image pixels that map back to a given source position as a function of the image positions. We expected that each component in MG0414 maps back to the same source, i.e. A1, A2, B, and C are all in the four-image region. However, Figure 3-8 clearly shows B is in the two-image region and the components west of B are in the four image region. Somewhat surprisingly, the model has enough freedom also to map the associated images of B to near the position of C.

We see this behavior in all the lens models used to fit MG0414. Even though the lens models have different angular structures and radial profiles, the addition of negative components artificially enhances the fit. The key to this behavior in LensClean is the differential magnification in the image. The components west of B are distributed such that they add no flux, however, their associated components at A1 and

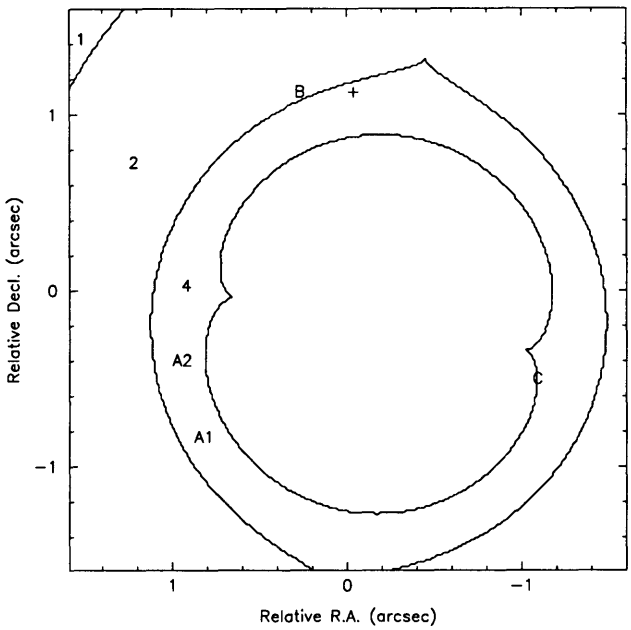

Figure 3-8: Multiplicity image from the best fit SIS plus external shear model using the Clean map LensClean method including negative clean components. The curves are boundaries between the 1, 2, and 4 image regions. A1, A2, B, and C show the locations of the MG 0414+0534 components and + symbol shows the location of the clean components west of B.

A2 contribute a large amount of flux. Since we are treating the image pixels as the real photons (i.e. tracing them through the lens), negative pixels are clearly artificial and cannot contribute to a valid image reconstruction. We, therefore, have modified LensClean so that it subtracts only positive clean components. This requirement constrains the pixels to be positive, but it also prevents any compensation for over-subtracting pixels during the iterative process. We minimized the oversubtraction by reducing the loop-gain (see Section 2.5.2) from 0.2 to 0.075.

3.5 Visibility LensClean

The Clean map LensClean algorithm forces the lens model to fit not only the gain-corrected visibilities, but the entire reconstructed visibility plane. Since standard

deconvolution methods are "local" in the sense that they ignore correlations caused by the lens galaxy, lensed images of a common source need not be consistent with each other in the final clean map. Chen, Kochanek, & Hewitt (1995) find that for lens model reconstructions of the Einstein ring, MG 1131+0456, differences in the CLEAN reconstructions affect the CLC results. In particular, they examine the sensitivity of their results to changes in the loop-gain parameter. They found the differences in the lens model solutions are consistent with the conservative confidence levels adopted, further justifying the validity of these conservative error estimates. However, variations in the loop-gain change the final rms residual by up to 50 percent. Since the tests were limited to CLEAN images, they could not fully explore the systematic errors, but they showed that the LensClean results are affected by the systematic errors in the reconstructed images.

We developed an improved LensClean algorithm, named Visibility LensClean (VLC), to avoid the systematic errors of the standard image reconstruction methods by operating directly on the complex visibility data. We implement VLC in the NRAO Software Development Environment. The algorithm is a modification of the Cotton-Schwab CLEAN algorithm (Schwab 1984; Cornwell & Fomalont 1989). As in the CLC algorithm, the minor cycle cleans the image under the constraints of the lens model. During the major cycle, the accumulated clean components from the previous minor cycle are subtracted from the ungridded visibility data, which are then Fourier transformed to produce the new residual dirty image. The major cycle ends when the peak-to-peak residual does not drop by more than one percent of its value from the previous major cycle.

Since VLC operates on the ungridded visibility data, the definition of a χ^2 statistic is straightforward. Let N_{vis} be the number of measured visibility points. Each visibility has complex value V_i and noise σ_i. We assume that the noise shows sufficiently little variability over the V_i to allow us to replace σ_i by an average noise per visibility point σ_V. If the model visibilities are V_i^{model} then the χ^2 statistic for the fit of the

model to the data is,

$$\chi^2_{vlc} = \sum_i^{N_{vis}} \frac{\left|V_i - V_i^{model}\right|^2}{\sigma_V^2}. \tag{3.31}$$

There is no ambiguity in the visibility-based clean as to the number of data being fit and the correct form for the χ^2 statistic. We, therefore, determine the lens model parameters by minimizing χ^2.

To evaluate the goodness-of-fit, we need to determine the number of degrees of freedom in the system. If we fit N_{comp} clean components in the source model and M parameters in the lens model, then the number of degrees of freedom is,

$$N_{dof} = 2N_{vis} - 3N_{comp} - M. \tag{3.32}$$

Each complex visibility has two degrees of freedom and we lose three degrees of freedom in specifying the position and flux of each clean component. Because the lens model completely determines the relationship between image plane components and the source plane components, we count the clean components in the source plane. The ambiguity in Equation 3.32 is whether multiple clean components can be subtracted at the same position. We believe N_{comp} is the number of independent components. Clean components at the same location correspond to multiple sinusoids with the same spatial frequency, and even though the clean components are chosen independently, fitting these identical functions to the measured data should not add degrees of freedom. We, therefore, conclude that clean components subtracted at the same location are not independent and should be treated as a single component.

We expect that the VLC results are less affected by systematic errors, and the formal errors more closely resemble the true errors. We use the same procedure for determining the parameter confidence levels as in CLC except we use the formal $\Delta\chi^2 \leq 4$ limit for calculating the 95 percent confidence intervals. We still try to compensate for any remaining systematic errors by rescaling the χ^2 such that the minimum χ^2 is equal to the expected number of degrees of freedom for the system. It is likely that this is a correct statistical interpretation, but it can only be confirmed

by extensive Monte Carlo simulations. A typical LensClean optimization requires $\simeq$ 10 hours on a desktop workstation. Therefore, to obtain 95 percent confidence levels, one would need $\gtrsim$ 20 optimizations requiring over a week per lens model parameterization.

3.5.1 Self-Calibration with a Model Consistent with Lensing

If the reconstruction of the image is inconsistent with the object being a gravitational lens, then self-calibration can reinforce the errors by adjusting the antenna gains to maximize the agreement with the incorrect reconstruction. Such a systematic bias in the self-calibration process will increase the estimated noise in the image, since the converged solution is not fully consistent with the measured data. We can test if errors are introduced by performing a self-calibration of the visibilities using the converged VLC model of the image. The decrease in χ^2 gives a measure of the errors in the original self-calibration. This approach is not fully self-consistent because the VLC reconstruction was found using the visibility data produced by the standard self-calibration methods. To fully correct for the systematic biases, the self-calibration and lens modeling need to be combined so the complex gain factors and lens parameters are optimized simultaneously.

The gain factors used in the self-calibration must be taken into account in the counting of the degrees of freedom, so Equation 3.32 becomes,

$$N_{dof} = 2N_{vis} - 3N_{comp} - M - \begin{cases} N_{gain} & \text{Phase only} \\ 2N_{gain} & \text{Amplitude and Phase} \end{cases} \tag{3.33}$$

where N_{gain} is the total number of gain solution intervals.

3.6 Clean map LensClean vs Visibility LensClean

To examine the differences between the CLC and VLC algorithms, we chose two gravitational lensing systems as test cases: MG 0414+0534 and MG 1654+1346. The

components in MG0414 test the reconstruction of compact sources, and the diffuse emission in MG1654 tests the reconstruction of extended low-level flux. The results are summarized in Table 3.1 for MG0414 and Table 3.2 for MG1654.

3.6.1 MG 0414+0534

We used the data from the 15 GHz VLA observation (Katz & Hewitt 1995). The reconstructed CLEAN image is shown in Figure 3-5. The beam full-width at half-maximum is 0".12 by 0".11. The peak fluxes of A1, A2, B, and C are 158 mJy/Beam, 141 mJy/Beam, 56.5 mJy/Beam, and 24.2 mJy/Beam, respectively. Using empty regions of the image, we estimated the noise at 180 mJy/Beam, and find that the peak-to-peak error—the maximum value minus the minimum value in the region—is 1.39 mJy/Beam. The data set includes 120390 visibility points with a theoretical noise per point of 36.8 mJy for a 10 second integration period (Crane & Napier 1989). We parameterized the lens model as a singular isothermal sphere in an external shear field (see Section A.1),

$$\phi(\vec{r}) = br + \frac{1}{2}\gamma r^2 \cos 2\left(\theta - \theta_\gamma\right) \tag{3.34}$$

where b is the critical radius, γ is the shear strength, and θ_γ is the shear position angle.

When we model MG0414 using the CLC algorithm, we find strong residuals near all the components. Figure 3-9a shows the residual image after subtraction of the clean components using the best fit lens parameters. We find large residuals near components B and C, suggesting the lens model does not have enough freedom to fit the measured data. However, the A1 and A2 images show alternating features, indicative of deconvolution errors. The best fit model has $\sigma_{mul} = 651$ μJy/Beam and a peak-to-peak error of 27.2 mJy/Beam. We find a large χ^2 of 9393 for 315 degrees of freedom. If we assume normally distributed errors, we find the fit is 360σ from an optimal fit (i.e. $\chi^2/N_{dof} = 1$).

We believe that some of the residual features result from the incorrect reconstruc-

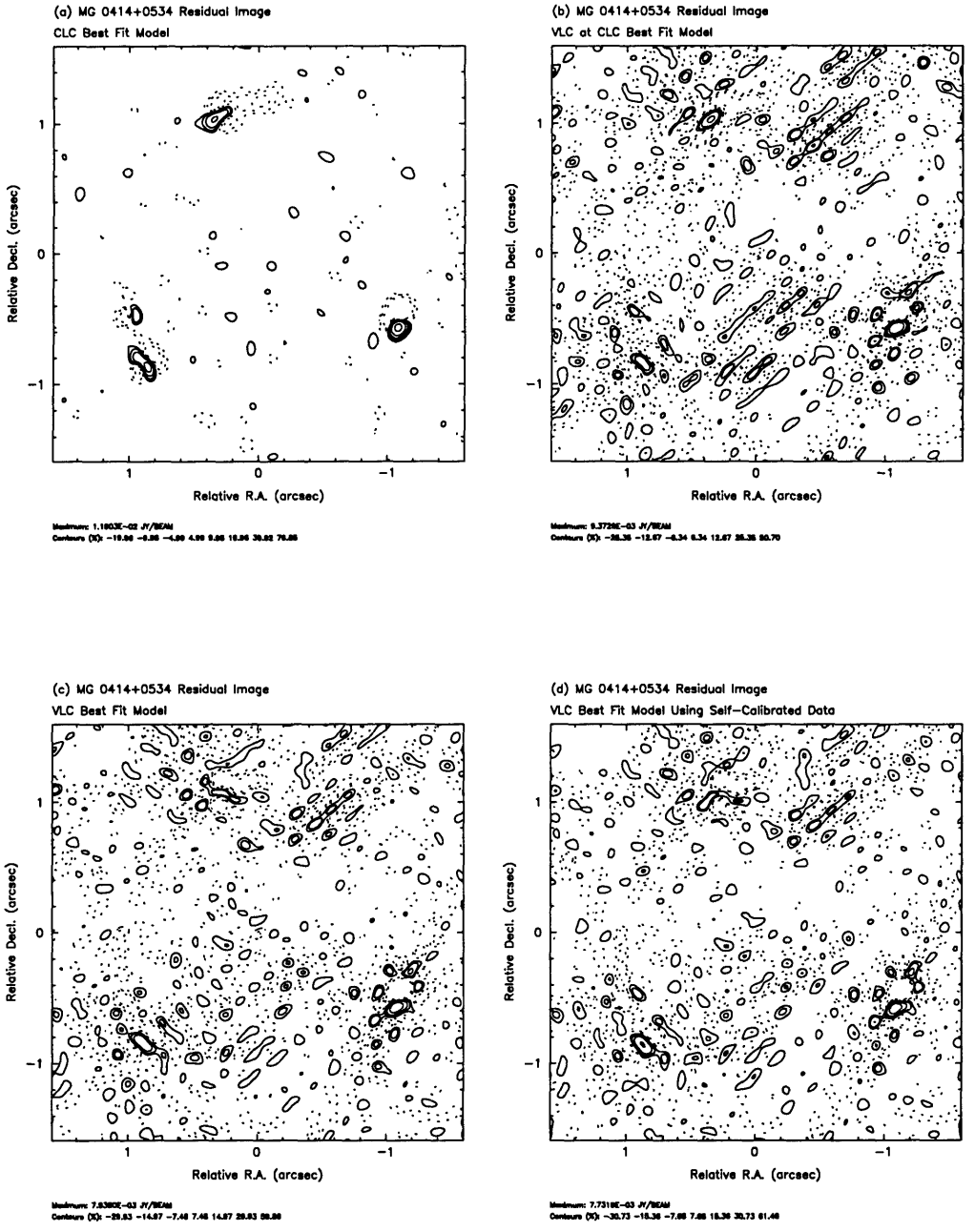

Figure 3-9: The MG+0414+0534 residual images after LensClean. The absolute contour levels are the same as Figure 3-5. Panel (a) shows the best fit residuals after Clean map LensClean. Panel (b) shows the residuals after Visibility LensClean using the best fit Clean map LensClean lens model. Panel (c) shows the best fit residuals after Visibility LensClean. Panel (d) shows the best fit residuals after Visibility LensClean on the self-calibrated data set.

Model	b asec	x_l asec	y_l asec	γ	θ_γ degrees
CLC	1.179±0.001	-0.480±0.003	-1.296±0.002	0.092±0.003	-10.1±0.5
VLC†	"	"	"	"	"
VLC	1.181±0.001	-0.482±0.002	-1.296±0.002	0.091±0.002	-9.6±0.3
VLC/SC	1.181±0.001	-0.490±0.001	-1.299±0.002	0.086±0.002	-9.6±0.3
	σ_{mul} μJy/Beam	P-P mJy/Beam	χ^2	N_{dof}	χ^2/N_{dof}
CLC	651.3	27.2	9390	315	29.8
VLC†	842.3	25.4	134000	64600	2.08
VLC	795.4	23.9	129000	64600	2.00
VLC/SC	788.8	23.9	125000	61700	2.03

† We performed Visibility LensClean fixing the lens model to the best fit model found by the Clean map LensClean algorithm.

Table 3.1: Results for the MG 0414+0534 system using the singular isothermal sphere plus external shear model. VLC/SC indicates the results using the visibility data set after self-calibration with the converged VLC model. The lens position is measured relative to component B. P-P indicates the peak-to-peak value in the residual image. θ_γ is measured north through east. The CLC confidence intervals are calculated using $\Delta\chi^2 \leq 15.1$ and the VLC confidence intervals are calculated using $\Delta\chi^2 \leq 4$. χ^2 is calculated using χ^2_{clc} for the CLC model and χ^2_{vlc} for the VLC models.

tions of the compact sources in the CLEAN image. The A1/A2 images are highly magnified so small changes in the reconstruction of the B/C images are lensed into larger features at A1/A2. CLEAN will always create these features because of its "local" nature, raising the question whether an algorithm which "globally" fits the data might solve the problem. To test this hypothesis, we replaced CLEAN reconstructed images with NNLS reconstructed images. The rms noise in the NNLS image agreed with that from the CLEAN image, and the differences between the images were less than 0.25 mJy/Beam, significantly smaller than the features seen in the CLC residuals, but the differences are peaked about the component positions indicating changes in the point source reconstructions. However, when we applied the CLC method to the NNLS image, we detected no significant change in the residual strength, pattern, or the lens model parameters. This test was not completely independent of the CLEAN algorithm because CLEAN was used to deconvolve the image during self-calibration. As another test, we repeated the entire self-calibration using

the NNLS method. As before, little change was seen in the CLC results. We conclude that the NNLS algorithm suffers from the same problems as CLEAN and introduces systematic errors into the reconstructed images.

For the VLC lens modeling, we used the NNLS self-calibrated data set, since both NNLS and CLEAN self-calibrated data sets perform identically in the CLC analysis. VLC requires subtraction of each clean component from each visibility data point; therefore, the data set was averaged from 10 second to 30 second intervals, increasing the computational efficiency. The number of visibility points drops to 32575, each with a theoretical noise of 21.2 mJy. First, we applied VLC using the lens model found by the CLC method. The residuals, shown in Figure 3-9b, have significantly more structure. Since the VLC algorithm subtracts using the dirty beam rather than the compact clean beam, errors in the lens model are introduced throughout the residual image via the sidelobes of the dirty beam. Consequently, we see the rms residual in the multiply-imaged region increases to 842 μJy/Beam. However, the peak-to-peak error drops by 5 percent to 25.4 mJy/Beam, suggesting small errors in the clean map reconstructions. The χ^2 is 134000; since the system has 64600 degrees of freedom, this χ^2 is 194σ from the expected best fit value. This value is, however, much lower than that estimated by the CLC algorithm, although the model remains a poor fit to the data.

Next, we optimized the lens model using VLC, and Figure 3-9c shows the residual image. The best fit solution has $\sigma_{mul} = 795$ μJy/Beam and a peak-to-peak error of 23.9 mJy/Beam, down 12 percent from the CLC best fit solution. The drop in both the rms error and peak-to-peak error suggests systematic errors in the clean map are affecting the CLC algorithm. We found a χ^2 of 129000, slightly better than the previous model. The lens parameters were found to be consistent within the confidence limits.

During the self-calibration stage, the deconvolution methods did not use any lensing information. As our final experiment on MG0414, we used the VLC clean component model to self-calibrate the visibility data set. This procedure tests the consistency of the gain-corrected visibility data with gravitational lensing. Because the

amplitudes were not adjusted in the original self-calibration, we performed a phase-only self-calibration with a 30 second solution interval. Figure 3-9d shows the best fit residual image after optimizing the lens model in VLC on the re-self-calibrated data. The rms residual drops slightly to 789 mJy/Bean and the peak-to-peak error remains unchanged. The χ^2_{vlc} is 125000 and the number of degrees of freedom has dropped to 61700 through the inclusion of 2900 gain factors in the self-calibration. The lens model parameters do vary slightly; however, the lens model does not fit significantly better. The errors are dominated by the incorrect fit of the lens model.

The small differences between the Clean map LensClean and Visibility LensClean solutions indicate that the CLC algorithm is affected by deconvolution errors. This analysis also shows that the CLC algorithm underestimates the rms error, since an incorrect lens model only causes errors near the clean components in error. The VLC algorithm will corrupt empty regions of the residual image through the sidelobes of the incorrect subtractions. Therefore, the VLC algorithm allows us to more easily identify problems with the lens model. Furthermore, we found a significant effect in the peak-to-peak residual. The VLC/SC solution had a peak-to-peak error 12 percent lower than the CLC solution. At the CLC best fit solution, the VLC algorithm found the χ^2 was 194σ from an optimal fit. After optimizing the lens model parameters within VLC, we found a significant improvement of 14σ to 180σ from an optimal fit. Even though the lens model was found to fit the system poorly, the differences between the CLC and VLC algorithms were detectable.

3.6.2 MG 1654+1346

In contrast to MG0414, MG1654 (Langston *et al.* 1989; Langston *et al.* 1990) provides an example of a lensing system dominated by extended emission. The background source is a $z_s = 1.74$ quasar, consisting of a compact core and two radio lobes. The southern lobe has been lensed into a ring. Kochanek (1995) has extensively modeled this system using the CLC algorithm. We compare our results with his models; however, the data set used by Kochanek (1995) was unavailable so we used one that differed slightly in the editing. Note that these data do not show the faint bridge

across the center of the ring and the low-level emission stretching vertically from the ring seen in Langston *et al.* (1990). Figure 3-10 shows the 8 GHz VLA image of the core and lensed radio lobe with an angular resolution of 0″.21 by 0″.19. In empty

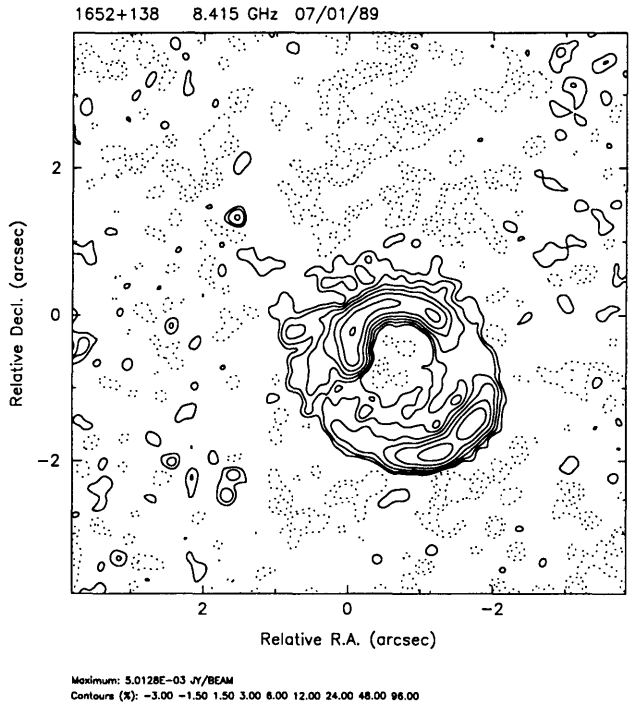

Figure 3-10: Final CLEAN image of MG 1654+1346 used in Clean map LensClean. The contour levels are -3, -1.5, 1.5, 3, 6, 12, 24, 48, and 96 percent of the peak, 5.01 mJy/Beam. The beam FWHM is 0″.21 by 0″.19.

regions of the image, the peak-to-peak error in the image is 500 μJy/Beam and the estimated noise is 59 μJy/Beam. The data set contains 18956 visibility points, each with a theoretical noise of 6.35 mJy/Beam (Crane & Napier 1989). The peak in the image is 5 mJy/Beam, although most of the flux in the system is contained in the fainter ring emission. Kochanek (1995) finds the lens in MG1654 is best fit by the first-order approximation to the elliptical mass distribution with surface density,

$$\Sigma(\vec{r}) = \frac{1}{2}\Sigma_c b^{2-\alpha}\left(1+\frac{r^2}{s^2}\right)^{\alpha/2-1}\left[1-\frac{2-\alpha}{2}\frac{r^2}{r^2+s^2}\epsilon\cos 2\left(\theta-\theta_\epsilon\right)\right] \tag{3.35}$$

where $\Sigma_c = c^2 D_{OS} D_{OL}/4\pi G D_{LS}$ is the critical surface mass density for lensing (see Section A.5). The monopole shape is controlled by the exponent α and the core radius

s. The ellipticity ϵ and the position angle θ_ϵ govern the quadrupole shape.

Since the MG1654 system has already been well fit by Kochanek (1995), we expect to detect more clearly small systematic errors in the image reconstructions. Our data set had small differences from the one used by Kochanek (1995), so we found the best fit CLC model for our data set. The residuals, shown in Figure 3-11a, have a peak-to-peak error of 727 μJy/Beam and $\sigma_{mul} = 73.8$ μJy/Beam, leading to a χ^2_{clc} of 310, significantly larger than Kochanek (1995) found. The best fit lens model found was consistent in all parameters except for the monopole exponent α. The residual image shows strong arcs with alternating positive and negative flux. The largest residuals are clustered about the emission regions of the map, and they are caused by striping in the reconstruction of the ring (see Section 2.5.2). The two sides of the ring are striped independently, and when the lens model in CLC overlaps these stripes, this results in an alternating residual pattern.

We tested if the constraint that clean components be positive-definite caused the differences in the results by using the Clean map LensClean algorithm allowing negative clean components on our data set (CLC†† in Table 3.2). Although we do not achieve the same goodness-of-fit, our lens model solution is consistent as Kochanek (1995) within the conservative error bars. We also find a significantly lower residual rms and peak-to-peak error than achieved with the positive-definite constraint. If we examine the clean component distribution, we find negative pixels in the image reconstruction. Figure 3-12 shows the clean component distribution for the Clean map LensClean analyses with and without the negative clean components. If we included the negative clean components, we find the largest negative pixel is -45 μJy/Beam, a significant fraction of the noise level. Although the bias is significantly smaller than that in the MG0414 analysis, we still find the negative pixels are a problem in the MG1654 analysis.

The VLC algorithm dramatically reduces the striping problem in CLC. The best fit VLC residual image is shown in Figure 3-11b. The ring-shaped residuals are significantly reduced and there is no longer the alternating pattern, although some coherent structures about the ring remain. The rms residual is $\sigma_{mul} = 61$ μJy/Beam,

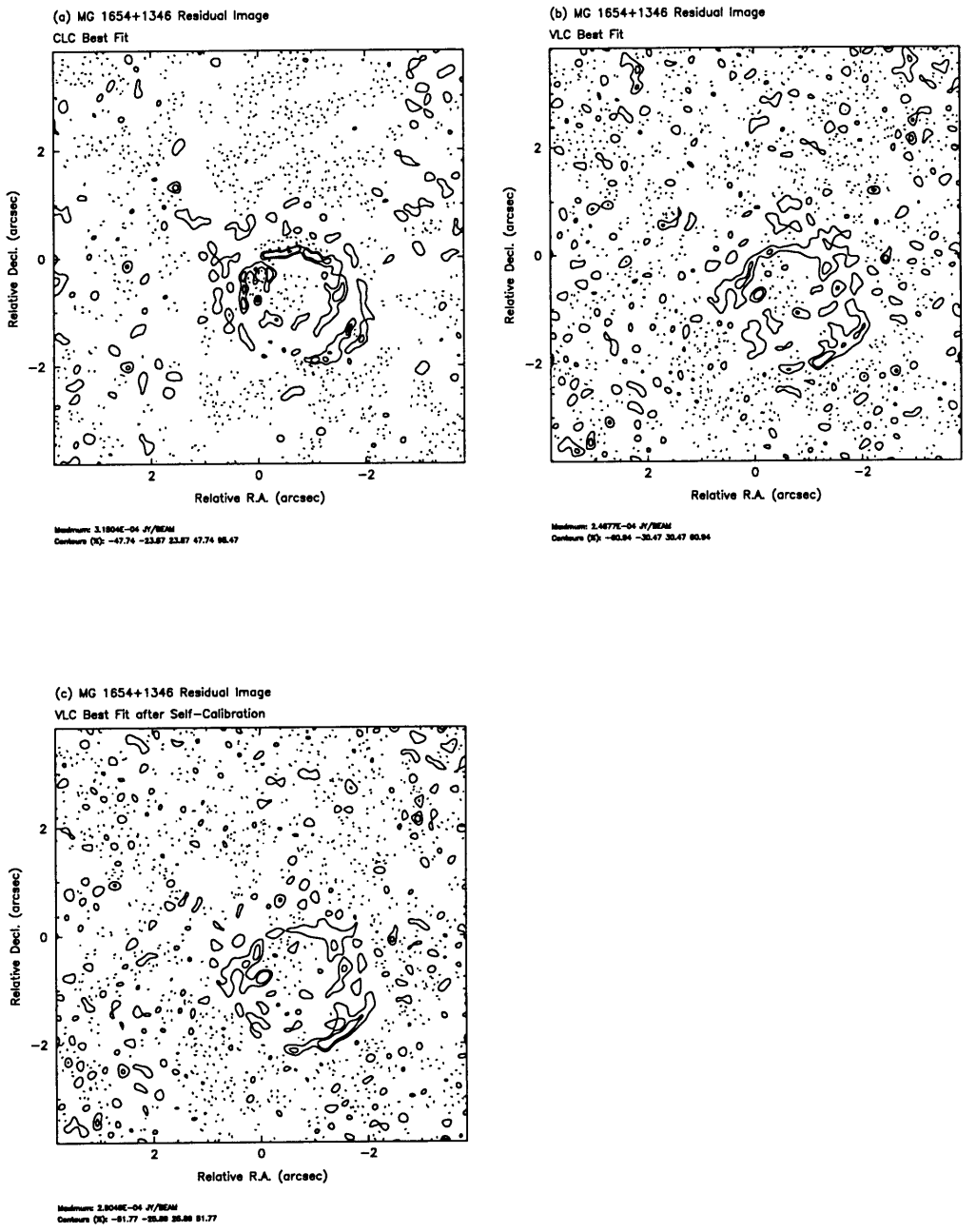

Figure 3-11: The MG 1654+1346 residual images after LensClean. The absolute contour levels are the same as Figure 3-10. Panel (a) shows the best fit residuals after Clean map LensClean. Panel (b) shows the best fit residuals after Visibility LensClean. Panel (c) shows the best fit residuals after Visibility LensClean on the self-calibrated data set.

Model	α	s asec	b asec	x_l asec	y_l asec
CLC†	$1.10^{+0.01}_{-0.16}$	$0.005^{+0.043}_{-0.005}$	1.119±0.106	2.263±0.008	-2.078±0.016
CLC††	1.11±0.15	0.005±0.027	1.133±0.131	2.201±0.007	-2.013±0.011
CLC	1.17±0.03	0.010±0.003	1.234±0.035	2.213±0.029	-2.028±0.030
VLC	1.16±0.02	0.016±0.007	1.206±0.023	2.210±0.014	-2.032±0.015
VLC/SC	1.15±0.01	0.016±0.001	1.203±0.003	2.223±0.003	-2.036±0.003
	ϵ	θ_ϵ degrees			
CLC†	0.286±0.086	11.5±1.1			
CLC††	0.283±0.066	11.6±1.9			
CLC	0.236±0.009	11.8±4.0			
VLC	0.226±0.002	11.1±0.1			
VLC/SC	0.226±0.002	11.1±0.1			
	σ_{mul} μJy/Beam	P-P mJy/Beam	χ^2	N_{dof}	χ^2/N_{dof}
CLC†	25	0.304	133	76	1.75
CLC††	60	0.683	195	76	2.57
CLC	74	0.727	310	76	4.08
VLC	61	0.491	42600	34600	1.23
VLC/SC	61	0.493	38900	34000	1.14

† Results from Kochanek (1995) using a different data set and the CLC algorithm allowing negative clean components.
†† Results using our data set and the CLC algorithm allowing negative clean component.

Table 3.2: Results for the MG 1654+1346 system using the approximate elliptical mass distribution. VLC/SC indicates the results using the visibility data set after self-calibration with the converged VLC model. The lens position is measured relative to the quasar core. P-P indicates the peak-to-peak value in the residual image. θ_γ is measured north through east. The CLC confidence intervals are calculated using $\Delta\chi^2 \leq 15.1$ and the VLC confidence intervals are calculated using $\Delta\chi^2 \leq 4$. χ^2 is calculated using χ^2_{clc} for the CLC model and χ^2_{vlc} for the VLC models.

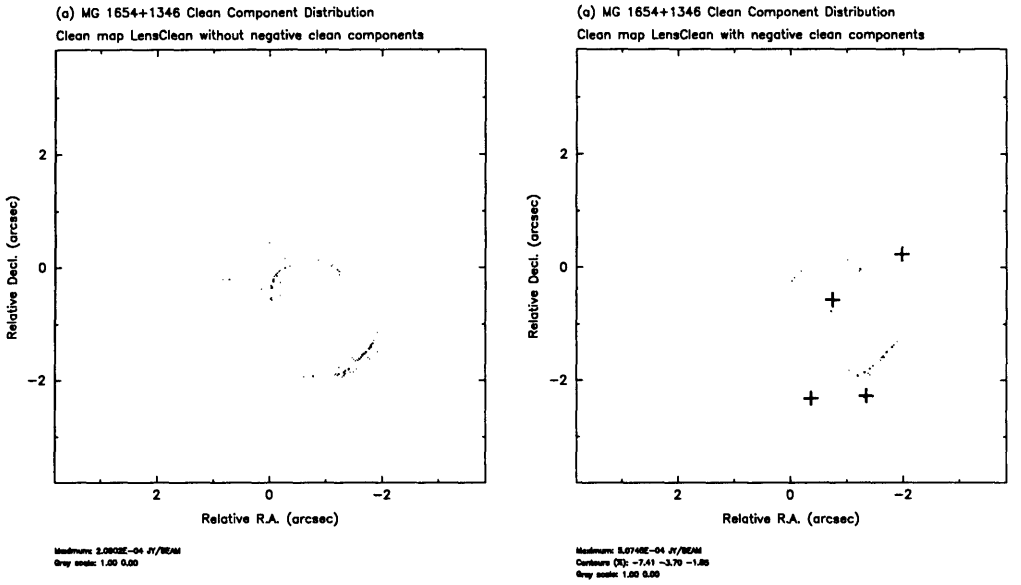

Figure 3-12: The distribution of clean components using the Clean map LensClean algorithm on the 5 GHz MG 1654+1346 data set. Panel (a) shows the distribution using the constraint of positive definite clean components and Panel (b) shows the distribution with negative clean components. The + symbols show the positions of the largest negative clean components ($\gtrsim$ 15 μJy/Beam).

consistent with the noise level in the CLEAN image, and the peak-to-peak value of 491 μJy/Beam. The χ^2_{vlc} is 42600. With 34600 degrees of freedom, we find χ^2_{vlc}/N_{dof} = 1.23, 38σ from the best fit. A normal CLEAN with no lens model gives a χ^2_{vlc} of 43100 with 27800 degrees of freedom, or χ^2_{vlc}/N_{dof} = 1.55, worse than the VLC fit. The primary effect is that the normal CLEAN uses far more independent clean components to fit the data. The VLC reconstruction is a more accurate representation of the image than the normal CLEAN component model. The VLC model solution is consistent with the CLC solution found in our analysis. However, we found that the solution is barely consistent with that found by Kochanek (1995). While most of the parameters are in reasonable agreement within the conservative CLC confidence intervals, the monopole exponent α is well outside the error bars. The error in the lens position is due primarily to the uncertainty in location of the quasar core between data sets rather than differences in the lens models. Within our data set, the CLC and VLC

best fit lens positions are consistent.

As in the MG0414 system, we self-calibrated the MG1654 data using the best fit VLC reconstruction as a model for the true image and redid a full optimization of the lensing parameters using VLC. Again, we performed a phase-only self-calibration since the data were not amplitude self-calibrated. The residuals are shown in Figure 3-11c. We found the rms residuals and peak-to-peak error did not change. However, the χ^2_{vlc} dropped to 38900 and the number of degrees of freedom has dropped to 34000, accounting for the 600 gain factors used in the self-calibration. The χ^2_{vlc}/N_{dof} dropped to 1.14, only 19σ from an optimal fit of $\chi^2_{vlc}/N_{dof} = 1$, assuming normally distributed errors. Since the lens model solution has not changed significantly from the best fit VLC solution, we conclude that the better fit is due to the reduction of systematic errors introduced in the original self-calibration.

The MG1654 tests show that sources dominated by extended emission are affected by the errors in the standard deconvolution methods. First, we find VLC shows a more dramatic effect in MG1654 than in MG0414 for two reasons. The lens model chosen does not fit the MG0414 system, so the systematic errors were dominated by the modeling errors. Second, the MG1654 data set contains fewer measured points for a significantly more complex source structure. We find that the VLC solutions are consistent with our CLC analysis and its conservative confidence levels. The Clean map LensClean algorithm used by Kochanek (1995) did not constrain the clean components to be positive-definite, leading to small changes in the reconstructions and converged lens model.

The constraints imposed by gravitational lensing allow a more ambitious interpretation of the reconstructed image. Since each of the four images is differentially magnified, the effective resolution of these images is significantly higher than estimated by the restoring beam (Kochanek & Narayan 1992). Since we have a lens model which better fits the system, we should be able to probe the higher spatial frequency structure in the image by convolving the converged VLC clean component model with a more compact beam. Figure 3-13a shows the best fit VLC reconstructed image using the self-calibrated data set. We convolved the clean component model

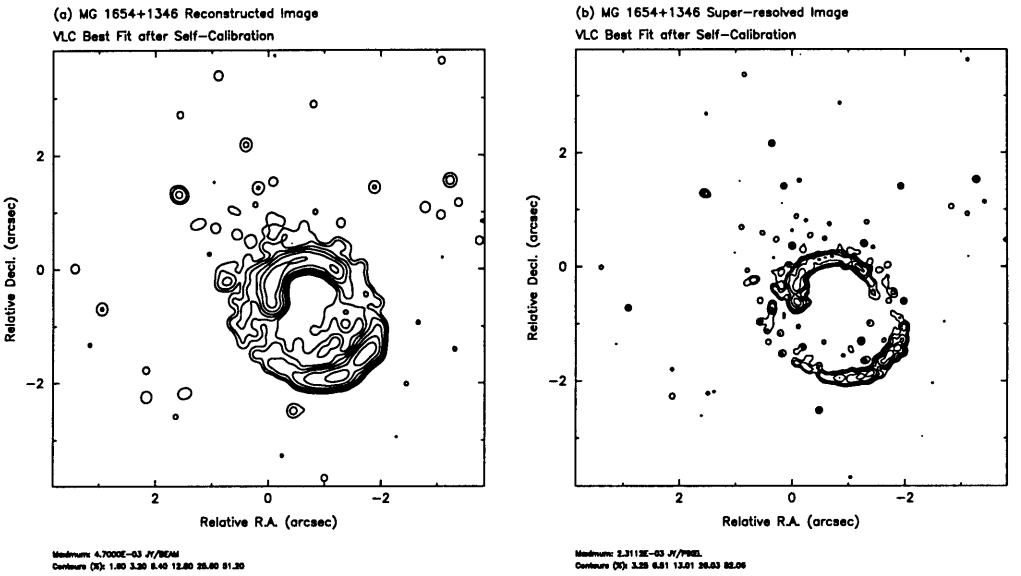

Figure 3-13: The reconstructed Visibility LensClean images of MG 1654+1346 using the self-calibrated data set. The absolute contour levels are the same as Figure 3-10. Panel (a) shows the reconstruction at normal resolution, 0.″21 by 0.″19. Panel (b) shows the super-resolved reconstruction using a 0.″1 restoring beam.

of the image with a 0.″1 restoring beam, an increase by a factor of two in resolution. The super-resolved image, shown in Figure 3-13b, is free of the "striping" artifact and appears to be reconstructed well. To test the accuracy of the super-resolution, higher frequency VLA observations are necessary.

3.7 Discussion of LensClean

The LensClean algorithm is well suited to the problem of reconstructing extended emission in the presence of noise and finite resolution. We found that the inclusion of negative clean components can dramatically bias the results of LensClean. In the case of MG0414, the extra freedom in the negative clean components caused LensClean to find an artificial fit to the system with an error nearly as small as that expected for an optimal fit. We found that the MG1654 system also was affected by negative clean components, but at a much lower level. The ring systems densely sample the

gravitational potential and, therefore, limit the freedom with which negative clean components can alter the fit.

We also find that the use of the clean map and beam as inputs for LensClean introduces errors into the lens modeling results. The source of the errors is in the incorrect reconstruction by the standard image deconvolution techniques. The primary effect is to reduce our ability to measure the goodness-of-fit of the model to the data. The standard deconvolution constraints of positivity and compactness do not require that the final reconstruction also be consistent with the gravitational lensing. Modifying the LensClean algorithm to operate directly on the visibilities improves the fit by reducing the deconvolution errors. Moreover, when a lens model is found to fit the system reasonably well, the lensing requirements reduce the range of allowable reconstructions and give a better fit to the data than a normal clean.

We also find that self-calibration reinforces the deconvolution errors by introducing systematic biases into the visibility data through the gain factors. When we perform a phase-only self-calibration on the MG1654 data using the best fit VLC reconstructed model, we found a significant reduction in the error, implying a better fit. Although we did not perform a fully self-consistent solution for the gain factors and lens model, we found that a single self-calibration with the converged VLC model can reduce the systematic errors introduced by self-calibration.

We believe that Visibility LensClean has reduced many of these systematic errors. Consequently, we should be able to interpret the goodness-of-fit more reliably and apply less conservative confidence intervals in the lens model parameters. The reliability of the confidence intervals depends on the sampling of the χ^2 surface. Sparse sampling may lead to underestimated uncertainties in the lens model parameters. Monte Carlo simulations are required to calculate the true parameter confidence intervals; however, these simulations are currently too computationally intensive to perform. In agreement with Kochanek (1995), we find the approximate elliptical mass distribution is a good but not perfect fit to the MG1654 system. However, the formal errors show the best fit lens model is no longer consistent with an exactly isothermal mass distribution.

We have shown that the standard deconvolution methods used in radio astronomy produce small systematic errors due to poor interpolation in the visibility plane and that the errors are easily detectable in VLA images of gravitational lenses. The level of these errors depends on the accuracy of the interpolation, and reconstructed images from sparser arrays, such as those from VLBI or MERLIN observations, or from other data sets containing fewer visibility points will have more serious problems. Therefore, the rigorous analysis of radio interferometry data should be performed only on the visibilities instead of the reconstructed images.

Chapter 4

Modeling the 15 GHz VLA Data

4.1 Visibility LensClean

Using the Visibility LensClean algorithm, we modeled the MG0414 15 GHz VLA data provided by Katz & Hewitt (1995). MG0414 was observed for 3 hours yielding 32575 complex visibilities points with a theoretical noise per point of 21.2 mJy (Crane & Napier 1989). The data were observed with the VLA in the A-configuration, resulting a beam FWHM of $\simeq 0''.1$. We applied VLC to the data using a variety of lens models. Since the LensClean algorithm requires an efficient solution for the images corresponding to a given source, the lens models attempted are simple approximations of a single galaxy. The models are characterized by a multipole expansion to quadrupole order of either the gravitational potential or surface mass density. This approach has been used to fit several lensing systems with satisfactory results (Kochanek & Narayan 1992; Chen *et al.* 1995; Kochanek 1995).

Kochanek (1991) and Hewitt *et al.* (1992) used a "point solver" lens inversion procedure (see Section 3.2) to fit the MG0414 system for the positions of the images with a variety of simple lens models and found that the system was difficult to fit. Components A1 and A2 are near the tangential critical line and are highly magnified. Small errors in B/C can lead to large variations at A1/A2. Furthermore, the 15 GHz VLA observations show A1, A2, and B to be resolved, which will add more constraints to the LensClean inversion.

4.1.1 Lens Models

The lens models used sample a variety of radial (monopole) structures and angular (quadrupole) structures. We included two lens models from Kochanek (1991). The deflections, magnifications, and surface mass densities for the following models are given in Appendix A.

The models specified by a gravitational potential are,

$$\begin{aligned}
\phi_1 &= br + \frac{1}{2}\gamma r^2 \cos 2(\theta - \theta_\gamma) \\
\phi_2 &= \left\{ \begin{array}{ll} \frac{b^{2-\alpha}}{\alpha}(r^2+s^2)^{\alpha/2} & \alpha \neq 0 \\ \frac{b^2}{2}\ln(r^2+s^2) & \alpha = 0 \end{array} \right\} + \frac{1}{2}\gamma r^2 \cos 2(\theta - \theta_\gamma) \\
\phi_3 &= br + \epsilon br \cos 2(\theta - \theta_\epsilon)
\end{aligned}$$

Model 1 and 3 (models 3 and 2 from Kochanek (1991)) are based on the singular isothermal sphere (SIS). Spiral galaxies show circular velocities which are constant as a function of radius from the center of the galaxy. Therefore, the inferred dynamical mass increases linearly with radius, indicating a three-dimensional mass density which falls off as r^{-2}. The SIS model distributes the matter in a spherically symmetric fashion with this same radial dependence. Model 1 includes an external shear field to break the spherical symmetry. The external shear field is the lowest order description of a mass distribution positioned outside of the region of interest. Model 3 is an approximation to an elliptical singular isothermal sphere. The surface mass density is expanded into a multipole expansion and truncated after the quadrupole moment. ϕ_3 is the gravitational potential which results from this surface mass density. Model 2 adds two parameters to vary the monopole structure. The exponent α controls the concentration of mass within a given radius. A smaller value of α corresponds to a higher mass density near the lens center, where $\alpha = 0$ is a Plummer potential (Blandford & Kochanek 1987), $\alpha = 1$ is an isothermal potential, and $\alpha = 2$ is a uniform sheet of matter. The core radius s is introduced to prevent the mass density from diverging at the lens center.

The models specified by a surface mass density are,

$$\Sigma_4 = \frac{\Sigma_c}{2}\frac{\left(\frac{b}{R_e}\right) I\left(\frac{r}{R_e}\right)}{\int_0^1 x I(x)\mathrm{d}x} + \text{external shear}$$

$$\Sigma_5 = \frac{\Sigma_c}{2} b^{2-\alpha}\left(r^2+s^2\right)^{\alpha/2-1}\left[1-\left(\frac{r^2}{r^2+s^2}\right)\left(\frac{2-\alpha}{2}\right)\epsilon\cos 2(\theta-\theta_\epsilon)\right]$$

where $\Sigma_c = c^2 D_{OS} D_{OL}/4\pi G D_{LS}$ is the critical density for lensing. Model 4 is based on the de Vaucouleurs light distribution assuming a constant mass-to-light ratio. De Vaucouleurs (1948) discovered that the light from elliptical galaxies can be described by,

$$I\left(\frac{r}{R_e}\right) = I_e e^{-7.67\left[(r/R_e)^{0.25}-1\right]} \tag{4.1}$$

where I_e is the surface brightness at the effective radius R_e. This model uses the same radial dependence for the monopole moment of the surface mass density. The quadrupole moment arises from an external shear field, i.e. $\phi_{shear} = \frac{1}{2}\gamma r^2 \cos 2(\theta-\theta_\gamma)$. Model 5 generalizes model 3 by adding a power law exponent α and core radius s to the mass density. As in model 3, the multipole expansion of the mass density is truncated after the quadrupole moment.

4.1.2 Results

Using VLC, we found the best fit lens model for all the lens models described in the previous section. The results are summarized in Table 4.1. The reconstructed and residuals images for all the best fit lens models are shown in Figures 4-1 through 4-9.

We expected that the angular structure is well constrained by the image geometry and found the external shear models to best fit the system. For the SIS plus external shear model (1), we found the rms residual in the multiply-imaged region σ_{mul} was 795 μJy/Beam and a peak-to-peak error of 24 mJy/Beam. The rms error is dominated by the large residuals at the image positions. The approximate elliptical SIS model (3) is a worse fit with $\sigma_{mul} = 1.23$ mJy/Beam.

We tested the dependence of the fit on the radial (monopole) structure of the lens by fixing the exponent and core radius of model 2 to different values. Optical

	b arcsec	x_l arcsec	y_l arcsec	γ/ϵ	$\theta_{\gamma/\epsilon}$ degrees	s/R_e arcsec	α
1	1.181±0.001	-0.482±0.002	-1.296±0.002	0.091±0.002	-9.6±0.3	–	–
2	1.171±0.001	-0.469±0.002	-1.295±0.002	0.181±0.004	-9.7±0.3	0.063	0.0
	1.174±0.001	-0.479±0.002	-1.296±0.003	0.144±0.002	-9.8±0.2	0.063	0.5
	1.174±0.001	-0.476±0.002	-1.295±0.001	0.093±0.002	-9.7±0.3	0.005	1.0
	1.177±0.004	-0.477±0.010	-1.290±0.004	0.085±0.007	-9.7±1.0	0.050	1.0
	1.196±0.001	-0.474±0.001	-1.288±0.001	0.085±0.007	-9.7±1.0	0.200	1.0
3	1.189±0.002	-0.563±0.015	-1.311±0.011	0.062±0.014	-9.6±2.8	–	–
4	1.148±0.002	-0.477±0.002	-1.295±0.003	0.129±0.004	-9.7±0.3	1.250	–
5	0.706±0.015	-0.482±0.010	-1.262±0.002	0.931±0.016	-13.1±0.3	0.001	0.5
	σ_{mul} mJy/Beam	P-P mJy/Beam	χ^2_{vlc}	N_{dof}	χ^2_{vlc}/N_{dof}		
1	0.795	23.9	129000	64600	2.00		
2	0.832	26.8	123000	64700	1.89		
	0.856	27.5	127000	64800	1.96		
	0.893	26.9	130000	64800	2.00		
	0.889	27.7	131000	64800	2.03		
	0.871	25.6	135000	64600	2.09		
3	1.227	28.3	189000	64600	2.93		
4	0.830	25.6	125000	64700	1.92		
5	1.490	48.2	229000	64800	3.53		

Table 4.1: Visibility LensClean results on the 15 GHz VLA MG 0414+0534 data set. The results are from Visibility LensClean on the original self-calibrated data set. The errors are 95 percent confidence levels. The lens position is measured relative to component B. The shear position angle is measured north through east. P-P is the peak-to-peak value in the residual image.

observations of MG0414 do not show a nearby cluster of galaxies, so we chose radial structures which approximate a single object, $\alpha = 0.0$, 0.5, and 1.0. For the $\alpha = 0.0$ and $\alpha = 0.5$ models, we set the core radius to be small, $s = 0''.063$. To test the dependence of the fit to the core radius, we fixed the core radius of the isothermal model to $0''.005$, $0''.05$, and $0''.20$. We found a slight preference for smaller values of α and s, although only at the 5 percent level. Figure 4-7 shows a small amount of flux arising near the center of the system due to the presence of the "fifth" image. Since there is no evidence for the "fifth" image in the radio observation of MG0414 (Katz & Hewitt 1995), we did not try larger core radii.

For the de Vaucouleurs model (4), we fixed the effective radius at $1''.25$ and optimized the remaining parameters. We found this lens model performed as well as the

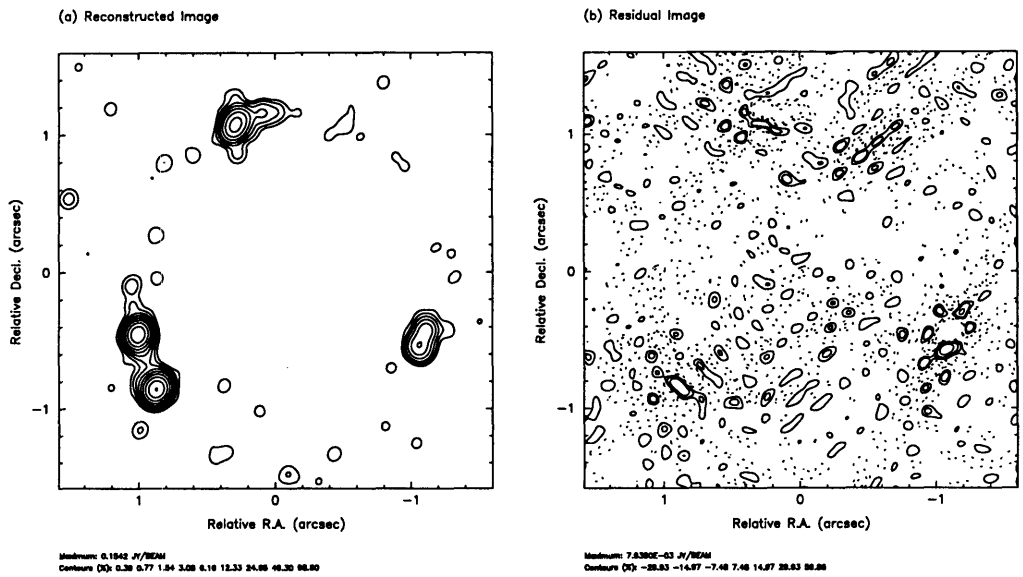

Figure 4-1: Panel (a) shows the reconstructed image and Panel (b) shows the residual image from the best fit singular isothermal sphere (SIS) plus external shear model (1). The absolute contours levels are the same as Figure 3-5.

other external shear models, even though the radial structure is changed from a power law to an exponential. The residuals have $\sigma_{mul} = 830$ μJy/Beam and a peak-to-peak error of 26 mJy/Beam. Since we did not see a significant change in the results as a function of the radial shape parameters, we did not vary the effective radius.

For the approximate elliptical mass models (model 5), we fixed $\alpha = 0.0$ and $\alpha = 0.5$. We omitted the isothermal case ($\alpha = 1$), since that model is identical to model 3 except for the finite core radius. Since the core radius had only a little effect on the fit, we set $s = 0''.001$. We could not fit the system using $\alpha = 0.0$ since the required ellipticity was much greater than unity. For the $\alpha = 0.5$ model, we found a poor fit to the system. The residual have $\sigma_{mul} = 1.49$ mJy/Beam and a peak-to-peak error of 48 mJy/Beam. The required ellipticity of 0.9 is extremely large.

These results show that none of the lens models fit the system well. The dominant factor in the level of the fit is the angular structure of the lens. From the reconstructed images we can see that in all cases, both components B and C are not fit well, indicating problems with the angular shapes of the lens models. The models which

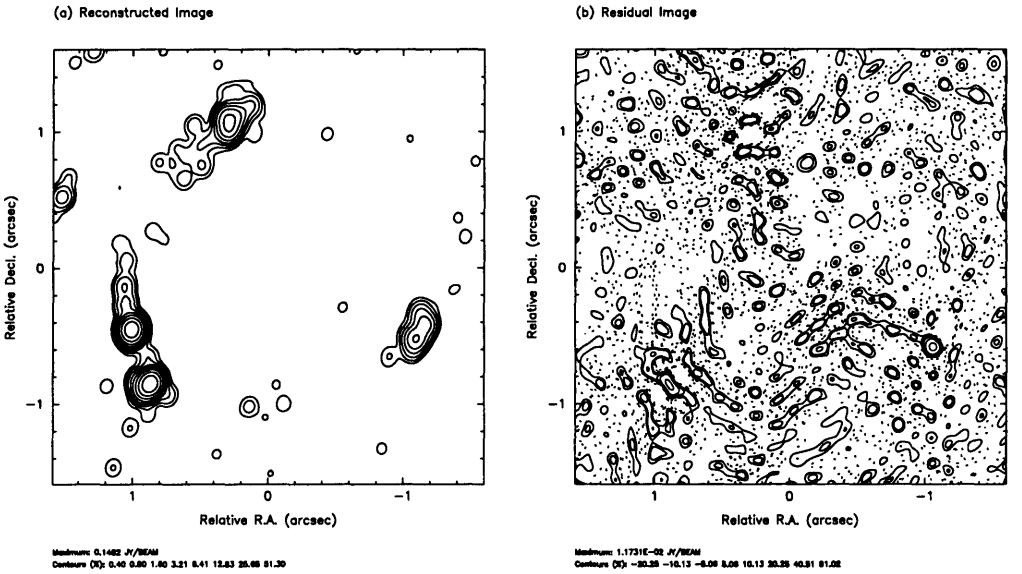

Figure 4-2: Panel (a) shows the reconstructed image and Panel (b) shows the residual image from the best fit approximate singular isothermal ellipsoid model (3). The absolute contours levels are the same as Figure 3-5.

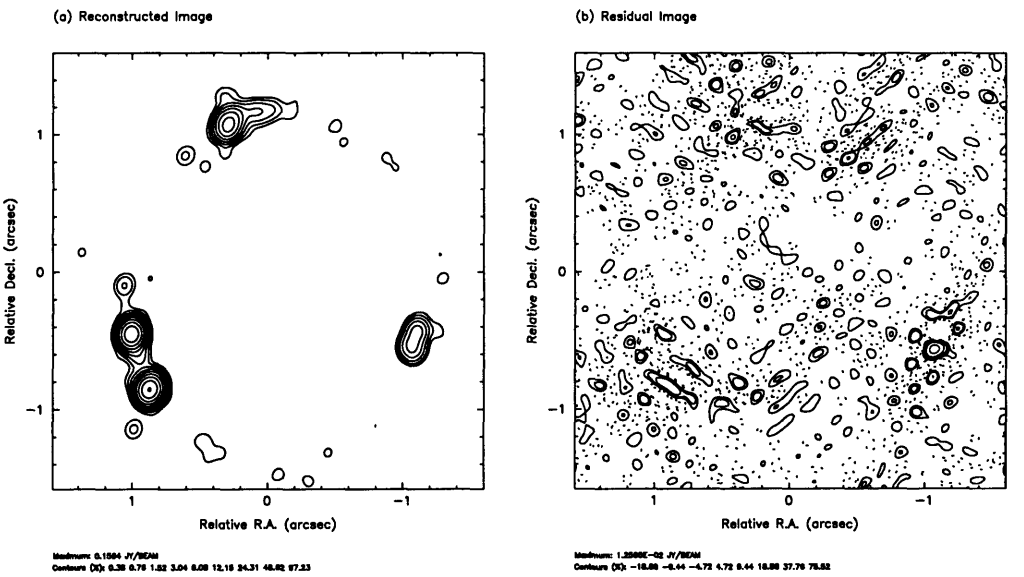

Figure 4-3: Panel (a) shows the reconstructed image and Panel (b) shows the residual image from the best fit generalized monopole plus external shear model (2) using $\alpha = 0.0$ and $s = 0''.005$. The absolute contours levels are the same as Figure 3-5.

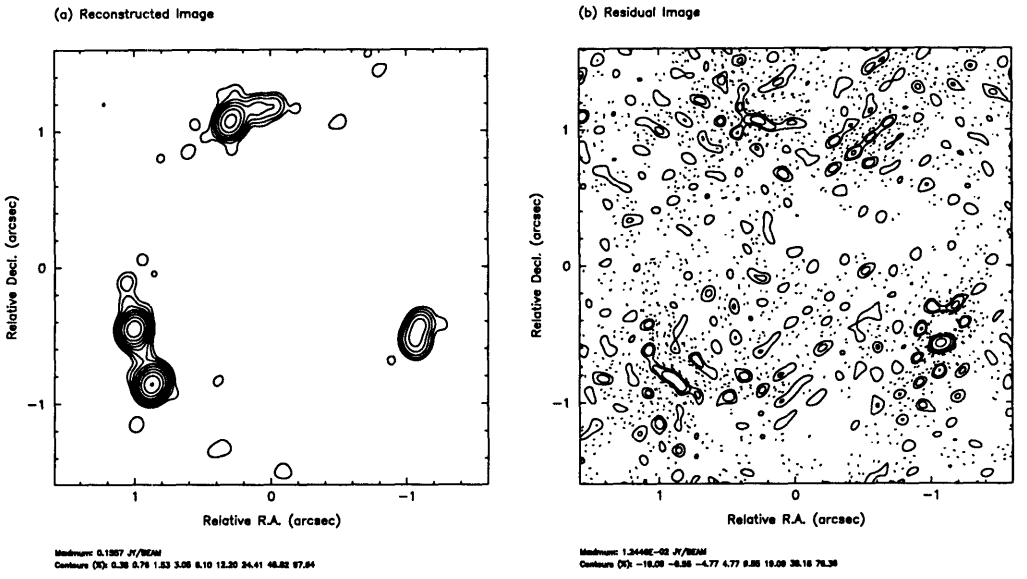

Figure 4-4: Panel (a) shows the reconstructed image and Panel (b) shows the residual image from the best fit generalized monopole plus external shear model (2) using $\alpha = 0.5$ and $s = 0''.005$. The absolute contours levels are the same as Figure 3-5.

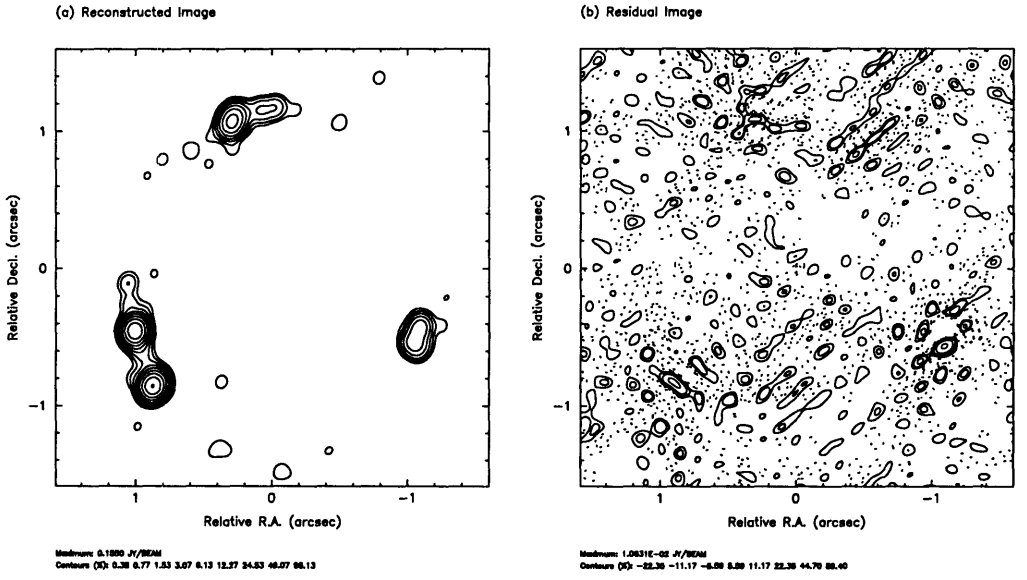

Figure 4-5: Panel (a) shows the reconstructed image and Panel (b) shows the residual image from the best fit generalized monopole plus external shear model (2) using $\alpha = 1.0$ and $s = 0''.005$. The absolute contours levels are the same as Figure 3-5.

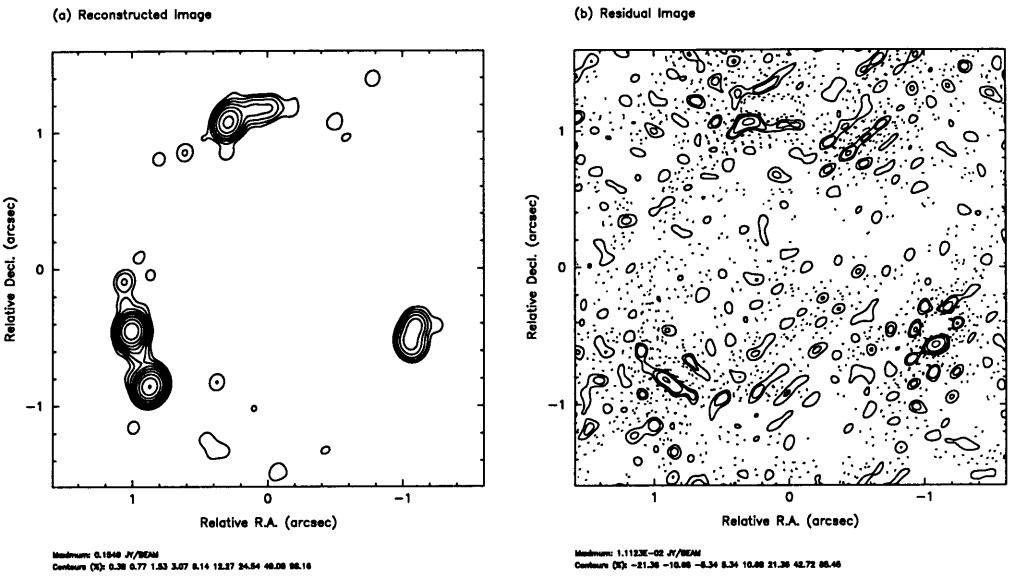

Figure 4-6: Panel (a) shows the reconstructed image and Panel (b) shows the residual image from the best fit generalized monopole plus external shear model (2) using $\alpha = 1.0$ and $s = 0''.05$. The absolute contours levels are the same as Figure 3-5.

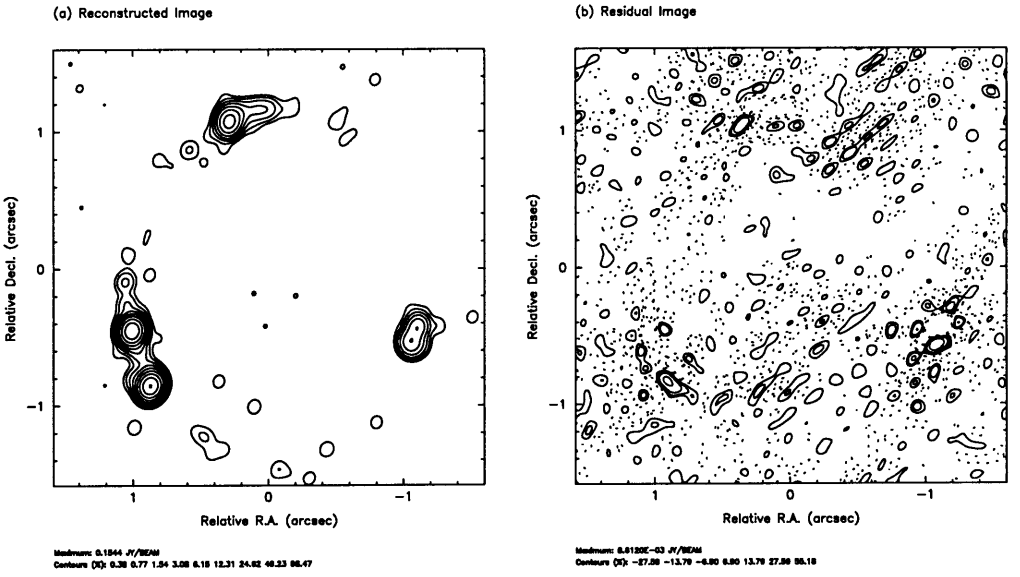

Figure 4-7: Panel (a) shows the reconstructed image and Panel (b) shows the residual image from the best fit generalized monopole plus external shear model (2) using $\alpha = 1.0$ and $s = 0''.20$. The absolute contours levels are the same as Figure 3-5.

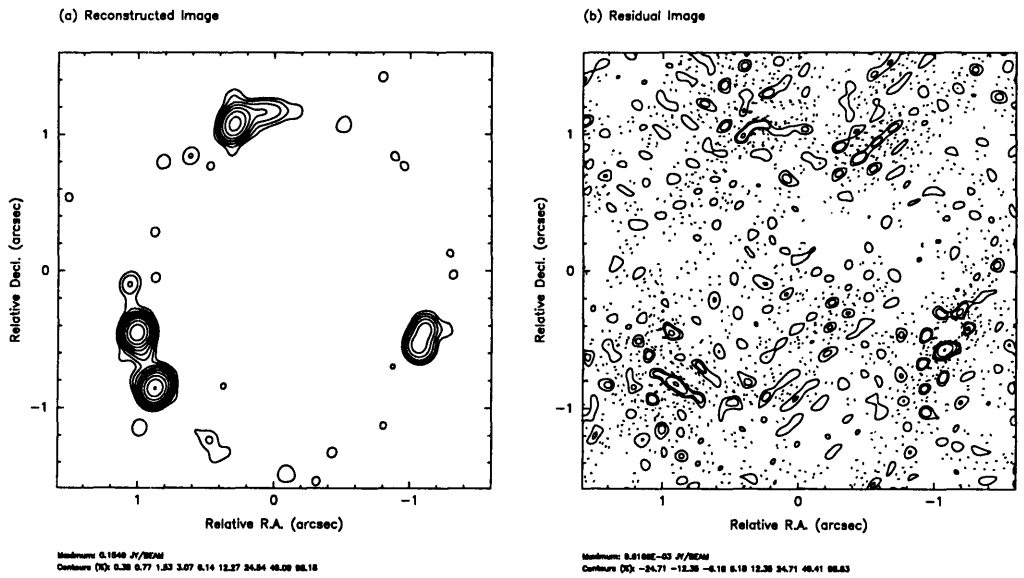

Figure 4-8: Panel (a) shows the reconstructed image and Panel (b) shows the residual image from the best fit de Vaucouleurs plus external shear model (4) using $R_e = 1''.25$. The absolute contours levels are the same as Figure 3-5.

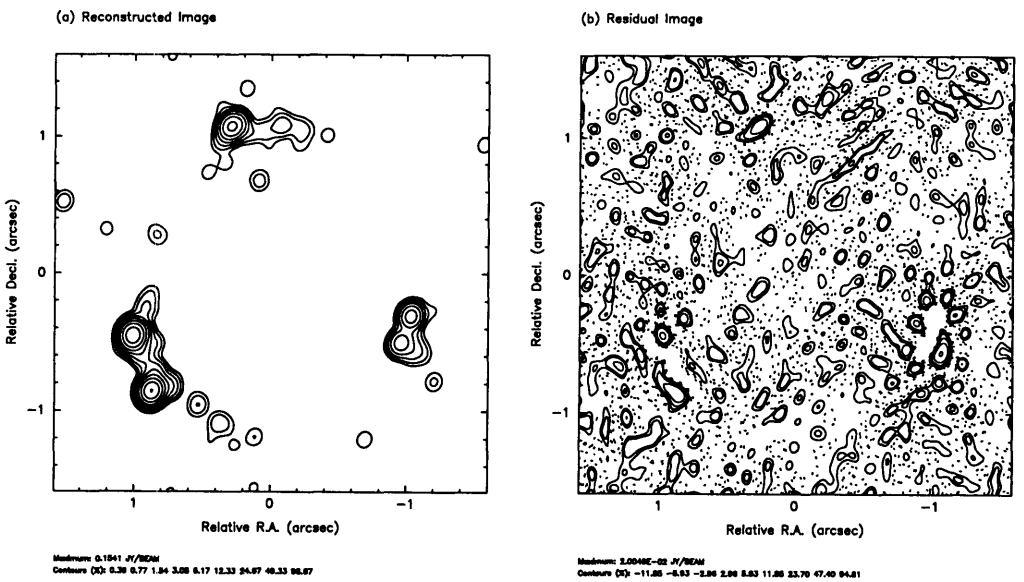

Figure 4-9: Panel (a) shows the reconstructed image and Panel (b) shows the residual image from the best fit approximate elliptical mass distribution model (5) using $\alpha = 0.5$. The absolute contours levels are the same as Figure 3-5.

contain internal shear contributions (models 3 and 5) do not fit the system as well as the external shear models (1, 2, and 4).

The radial dependence of the monopole moment does not greatly impact the fit of the lens model to the data. The Plummer potential fits slightly better than the isothermal models. The fits favor a lower core radius, although the effect is at the 5 percent level. We can understand the weak sensitivity of the system to the radial structure of the potential by examining the image geometry. Let r_{min} (r_{max}) be the radial distance from the lens center to closest (farthest) image. We find the difference between the largest and smallest radius is a small fraction of the mean radial distance from the lens center, i.e. $(r_{max} - r_{min})/2 \simeq 0.15\bar{r}$, so the images only sample the gravitational potential within a small annulus (Kochanek 1991).

We found that although the models to not fit perfectly, they do not have much freedom to vary the parameters greatly. We found the lens positions are consistent with the centroid of the galaxy measured by the Hubble Space Telescope (Falco 1995). Therefore, the primary lens in MG0414 is the galaxy first detected by Schechter & Moore (1993). The position angle of the shear is well constrained by the configuration of the images to be -10 degrees (north through east). Even though the critical radius and shear strength are coupled, the critical radius is well determined by the image separations, excluding model 5 due to the poor fit and large ellipticity.

The results show that a simple monopole and quadrupole component can fit the system at the 90 percent level (i.e. the peak residual is $\simeq$ 10 percent of the peak flux in the system). The primary error appears to be the position of component C. In the SIS plus external shear model, the error in position is $\simeq 0''.1$. We can imagine four sources of the error. We assumed the higher order moments in the multipole expansion were not important in the global structure of the lens. If the lens galaxy were deformed, the quadrupole approximation may not be valid. Second, we have assumed that object X—the faint object 1″ west of component B—does not affect the lens modeling. If object X is important, the external shear will account for some of the effect. However, the proximity of object X to the image positions increases the strengths of the higher order moments in the multipole expansion. A

third source of error can arise from variability in the system. The different arrival time of each component from the source to the observer then causes the observed image to be inconsistent with the underlying lens. Moore & Hewitt (1995) found the flux of MG0414 is varying at the level of a few percent. The lens inversion errors are $\simeq$ 10 percent of the peak flux which is significantly higher than would be expected from the measured variability. The fourth possible contribution to the error is from the global mass distribution in the universe. Seljak (1994) showed that the effects of large-scale structure will shift the relative positions of the images by a few percent. In the case of MG0414, the apparent shifts would be $\approx$ 50 mas, slightly smaller than our position error at C. However, structures smaller than those considered by Seljak (1994) could significantly affect the image geometry.

4.2 Point Source Lens Inversion

Since the previous lens models were unable to fit the MG0414 system, we pursued more complex lens parameterizations. Although we preferred the LensClean algorithm because of its proper handling of extended structures and finite resolution, the method requires that the image positions and magnifications be determined efficiently for all possible source components. LensClean is currently not able to handle the more general classes of models. Therefore, we developed a "point solver" inversion technique for this system. The point solver only maps the images back to the source plane and, thus, does not require a solution to the nonlinear equation for the images.

Since the MG0414 system consists of four compact images, we approximated those components as point sources and required that the four images must map back to the same point in the source plane. Therefore, both the positions and the fluxes at the source plane must agree. Furthermore, we required that the position of the lens must coincide with the centroid of the galaxy at optical wavelengths. Falco (1995) determined from Hubble Space Telescope (HST) measurement the position is 0$''$.466

west and 1.″27 south of component B. We define our error measure as,

$$\chi^2 = \chi^2_{pos} + \chi^2_{flux} + \chi^2_{lens} \tag{4.2}$$

where,

$$\chi^2_{pos} = \sum_i^4 \left(\vec{\beta}_i - \left\langle\vec{\beta}\right\rangle\right)/\sigma^2_{\beta_i}, \tag{4.3}$$

$\left\langle\vec{\beta}\right\rangle$ is the mean position, and σ_{β_i} is the uncertainty in the source plane position. In the coordinate system where the magnification matrix is diagonal, we see that the magnification is given by $\mu = \lambda_u\lambda_v$. Since the magnification in the two directions are not the same, the correct error measure is $\left[\lambda_u^2(u_i - \bar{u})^2 + \lambda_v^2(v_i - \bar{v})^2\right]/\sigma_\theta^2$, where σ_θ is the image plane error. However, the deviation of the magnification from unity is usually dominated by one eigenvalue. We, therefore, define the source plane error as,

$$\sigma_{\beta_i} = \sigma_{\theta_i}/|\mu_i| \tag{4.4}$$

where σ_{θ_i} is the image plane error and $|\mu_i|$ is the magnification for the ith image. Therefore, our error measure is,

$$\chi^2_{pos} = \left[\lambda_u^2\lambda_v^2(u_i - \bar{u})^2 + \lambda_u^2\lambda_v^2(v_i - \bar{v})^2\right]/\sigma_\theta^2 \tag{4.5}$$

which is typically larger by a factor of two than the true error measure since we underestimated the error in the unmagnified direction(Kochanek 1991). For this formulation, we see that the correct definition for the mean is,

$$\left\langle\vec{\beta}\right\rangle = \frac{\sum_i^4 \vec{\beta}_i|\mu_i|^2}{\sum_i^4 |\mu_i|^2}. \tag{4.6}$$

The error measure from the magnifications (fluxes) is,

$$\chi^2_{flux} = \sum_i^4 \left(\mathcal{F}_i - \langle\mathcal{F}\rangle\right)^2/\sigma^2_{\mathcal{F}_i} \tag{4.7}$$

where $\mathcal{F}_i = f_i/|\mu_i|$ is the source plane flux of the ith image, $\langle\mathcal{F}\rangle$ is the square magni-

fication weighted mean flux, and $\sigma_{\mathcal{F}_i}$ is the flux error in the source plane. The image plane flux errors σ_{f_i} are simply scaled by the magnification to obtain the source plane errors,

$$\sigma_{\mathcal{F}_i} = \sigma_{f_i}/|\mu_i|. \tag{4.8}$$

To constrain the primary component in the lens model to be centered on the position of the galaxy found by Falco (1995), we added,

$$\chi^2_{lens} = \left(\vec{x}_{model} - \vec{x}_{HST}\right)^2 / \sigma^2_{HST}. \tag{4.9}$$

We estimated the uncertainty in the HST position of 30 mas, approximately half the point spread function. Since the position is measured relative to component B, the error estimates the uncertainties in finding the centroid of both the lens galaxy and component B.

From the four images in MG0414, we have three relative position and three relative flux measurements from Katz & Hewitt (1995), given in Table 4.2. Since the magnification changes rapidly near A1 and A2, we only used the peak flux values and not the integrated flux values. The HST position of the primary component gives two more measurements. Therefore, the number of degrees of freedom is,

$$N_{dof} = 11 - M \tag{4.10}$$

where M is the number of parameters required to specify the lens model.

Component	$\Delta\alpha$ asec	$\Delta\delta$ asec	σ_θ asec	Flux mJy/Beam	σ_f mJy/Beam
A1	0.588	-1.934	0.01	159.12	6.84
A2	0.721	-1.530	0.01	139.98	6.02
B	-	-	-	56.335	2.42
C	-1.361	-1.635	0.01	24.153	1.43

Table 4.2: Image positions and peak fluxes for the components in MG0414. The image positions are measured relative to component B. These data were taken from Katz & Hewitt (1995).

4.2.1 Lens Models

We began with two lens models implemented in LensClean for comparison: the singular isothermal sphere in an external shear and the approximate singular isothermal ellipsoid,

$$\begin{aligned} \phi_1 &= br + \frac{1}{2}\gamma r^2 \cos 2(\theta - \theta_\gamma) \\ \phi_2 &= br + \epsilon br \cos 2(\theta - \theta_\gamma) \end{aligned}$$

Both of these models have five parameters, leaving six degrees of freedom.

We used two approaches to fit the angular structure in MG0414. The previous models assumed that the monopole and quadrupole moments were sufficient to describe the galaxy. We tested this assumption by including higher order moments in the multipole expansion. We chose the following models,

$$\begin{aligned} \phi_3 &= br + \frac{1}{2}\gamma r^2 \cos 2(\theta - \theta_\gamma) + \epsilon br \cos 2(\theta - \theta_\epsilon) \\ \phi_4 &= br + \frac{1}{2}\gamma r^2 \cos 2(\theta - \theta_\gamma) + \beta r^3 \cos 3(\theta - \theta_\beta) \\ \phi_5 &= br + \frac{1}{2}\gamma r^2 \cos 2(\theta - \theta_\gamma) + \delta r^4 \cos 2(\theta - \theta_\delta). \end{aligned}$$

These models are based on the SIS plus external shear model (1). Model 3 includes quadrupole moments from the external shear and ellipticity of the mass distribution. Model 4 breaks the reflection symmetry assumed in the previous models and Model 5 simply includes the octupole moment. The additional terms in models 4 and 5 arise from mass distributions external to the system (i.e. outside the ring of images). Each additional term adds two parameters—one to specify the amplitude and one to specify the position angle—to the lens model, leaving four degrees of freedom in the system.

Our second approach concentrated on the possible perturbation to the gravitational potential by object X. Schechter & Moore (1993) found the position of object X to be 1″ west of B, although they did not state an error on this determination. We

Lens	b	x_l	y_l	γ/ϵ	$\theta_{\gamma/\epsilon}$
	arcsec	arcsec	arcsec		degrees
1	1.187±0.017	-0.469±0.035	-1.269±0.014	0.091±0.021	-10.3±2.9
2	1.192±0.053	-0.597±0.100	-1.306±0.031	0.093±0.050	-11.3±7.6
	χ^2_{pos}	χ^2_{flux}	χ^2_{lens}	χ^2	
1	158.6	49.8	0.2	209	
2	232.5	103.9	23.3	360	

Table 4.3: Best fit lens model parameters and error statistics for the singular isothermal sphere plus external shear and approximate singular isothermal ellipsoid using the point source solver. The errors are 95 percent confidence intervals. The lens position is measured relative to component B. These models have six degrees of freedom.

introduced a second singular isothermal sphere to several of the previous lens models as an approximate description of object X. Since the second component adds three parameters to specify the mass and position, we chose simple lens models for the primary galaxy,

$$\begin{aligned}
\phi_6 &= br + b' |\vec{r} - \vec{r}'| \\
\phi_7 &= br + \epsilon br \cos 2(\theta - \theta_\epsilon) + b' |\vec{r} - \vec{r}'| \\
\phi_8 &= br + \frac{1}{2}\gamma r^2 \cos 2(\theta - \theta_\epsilon) + b' |\vec{r} - \vec{r}'|
\end{aligned}$$

Model 6 consists only of two singular isothermal spheres. With this model, we explored the possibility of accounting for the ellipticity in the primary galaxy through the effects of a perturbing spherically symmetric component. Models 6 and 7 attempt to fit the system with the primary galaxy dominating, and using the additional SIS component as a perturbation to match the observed images.

4.2.2 Results

We started the minimizations of models 1 and 2 at the best fit solution found by Visibility LensClean. As expected, we found that these lens models do not fit the system well. The results are summarized in Table 4.3.

Lens	b	x_l	y_l	γ	θ_γ	
	arcsec	arcsec	arcsec		degrees	
3	1.183±0.025	-0.450±0.063	-1.302±0.075	0.107±0.307	6.0±19.0	
4	1.189±0.004	-0.467±0.006	-1.240±0.004	0.081±0.010	-17.0±1.6	
5	1.169±0.016	-0.412±0.038	-1.304±0.075	0.084±0.359	-1.3±5.7	
	$\epsilon/\beta b/\delta b^2$	$\theta_{\epsilon/\beta/\delta}$	χ^2_{pos}	χ^2_{flux}	χ^2_{lens}	χ^2
3	0.030±0.091	-53.7±29.9	12.3	53.3	1.4	67
4	0.004±0.002	41.8±4.7	0.6	5.6	1.1	7.3
5	0.006±0.200	26.1±6.5	72.0	40.8	4.7	118

Table 4.4: Best fit lens model parameters and error statistics for lens models 3, 4, and 5 using the point source solver. The errors are 95 percent confidence levels. The lens position is measured relative to component B. These models have four degrees of freedom.

Next, we examined the lens models with additional moments. The results for these models are given in Table 4.4. We see an interesting result. The addition of a quadrupole or octupole moment in models 3 and 5 improved the fit over model 1; however, these models are still far from an optimal fit. We find that after adding an "odd" component, we were able to reasonably fit the system with a χ^2 of 7.3, where the system has four degrees of freedom. The dominant source of error lay in matching the flux of component C. The $\cos 3\theta$ component is interesting since this is the only lens model component which does not have elliptical symmetry. We find the $\cos 3\theta$ component is about a factor of 10 weaker than the quadrupole moment at the image positions ($\frac{1}{2}\gamma \approx 10\beta b$).

To make sure that we did not create any additional images, we used the Gravitational Image Tracing[1] ray-tracing routines to map the images back to the source plane and reconstruct the source. Then, we mapped the source forward to the image plane. Figure 4-10 shows the reconstructed source with caustics and the image with critical lines for model 4. Since the GrIT routines require the images to lie on pixel centers, the images were mapped to slightly different positions in the source plane.

[1]The Gravitational Image Tracing (GrIT) package was written by John Ellithorpe at the Massachusetts Institute of Technology.

Examination of the reconstructed image, we found no additional images produced by this lens model. The caustics and critical lines clearly show a perturbation from the elliptical symmetry. The tangential critical line bulges towards the northwest, in the direction of object X.

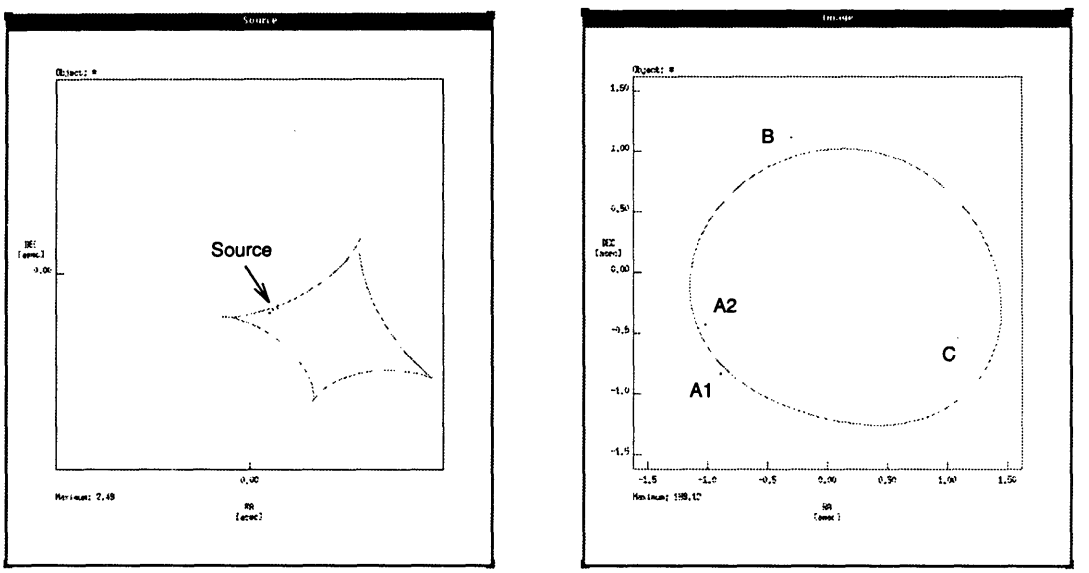

Figure 4-10: Panel (a) shows the reconstructed source and tangential caustic and and Panel (b) shows the point images and the tangential critical for Model 4. The image in panel (a) is a factor of four smaller in each dimension than the image in panel (b). Due to the finite pixel size, the source components do not lie on top of one another.

For the lens models with an additional SIS component, we could fit the system, although an ellipticity was required for the primary lens. The results are summarized in Table 4.5. The lens model with simply two SIS components could not reproduce the observed image positions and magnifications. The primary galaxy requires some ellipticity apart from the effects of the second SIS component. By adding the external shear field, we found a fit to the system with a χ^2 of 16, where the system has three degrees of freedom. The approximate elliptical SIS model could not fit the system as well. In model 8, the position of the additional SIS component is 0.″6 from the estimated position from Schechter & Moore (1993). However, the optical detection was near the 5σ limit (Schechter & Moore 1993), so its position may be uncertain. If object X is not at the same redshift as the primary galaxy, then its apparent position

will not correspond to that found through lens inversion. Furthermore, the properties of object X change due to the different image geometry at the object X redshift. The most significant change is that the critical radius found is the true critical radius scaled by the ratio D_{2S}/D_{1S}, where D_{1S} is the distance from the primary lens to the source and D_{2S} is the distance from the secondary lens to the source[2]. The size of these deviations from the solution found in the lens inversion depends on the difference in redshift.

As with model 4, we examined the model to look for additional images created by the lens. The critical radius of the additional component is much smaller than the distance to any of the images, so we do not expect to find multiple imaging from this component. Figure 4-11 shows the reconstructed source with caustics and the image with critical lines for model 8. Again, the positions in the source plane are not perfect due to the finite pixel size in GrIT. As expected, we found no additional images in the system created by the lens model. The caustics and critical lines look similar to those seen for model 4.

Since we are finding lens models which fit the system reasonably well, we are concerned with biasing the lens model solutions from variability. In section 3.4, we showed the peak errors due to variability will occur at component B because of its large time delay and differential magnification with respect to A1 and A2. To test the level of corruption in the fit, we changed the flux of B and fit the system using

[2]For a system with a second lens at a different redshift, the lens equation is,

$$\begin{aligned} D_{OS}\vec{\beta} &= D_{OS}\vec{\theta} - D_{1S}\vec{\alpha}_1 - D_{2S}\vec{\alpha}_2 \\ \vec{\beta} &= \vec{\theta} - \frac{D_{1S}}{D_{OS}}\left(\vec{\alpha}_1 - \frac{D_{2S}}{D_{1S}}\vec{\alpha}_2\right) \end{aligned}$$

where O indicates the observer, S indicates the source, 1 indicates the primary lens, and 2 indicates the secondary lens. We have assumed that the secondary lens does not produce multiple images. Note that $\vec{\theta}$ is the angular position of the apparent image and $\vec{\alpha}_1$ ($\vec{\alpha}_2$) depend on the angular positions of the light ray at the primary (secondary) lens plane. We can transform this lens into a single object at the primary lens redshift. The deflection angle of the single lens is given by,

$$\vec{\alpha} = \vec{\alpha}_1 - \frac{D_{2S}}{D_{1S}}\vec{\alpha}_2.$$

The exact form of this lens depends on the primary and secondary lens redshifts. From the transformation, we see that the secondary lens deflection is scaled by the ratio D_{2S}/D_{1S}.

Lens	b	x_l	y_l	ϵ/γ	$\theta_{\epsilon/\gamma}$
	arcsec	arcsec	arcsec		degrees
6	0.851±2.000	-1.029±0.500	-1.304±0.075	–	–
7	0.949±0.075	-0.504±0.044	-1.407±0.025	0.103±0.011	-18.7±2.0
8	1.127±0.047	-0.441±0.008	-1.290±0.005	0.088±0.020	-13.0±3.2
	b'	x'_l	y'_l		
	arcsec	arcsec	arcsec		
6	0.450±1.500	0.049±0.375	-0.211±0.500		
7	0.318±0.166	-0.981±0.500	-0.589±0.875		
8	0.076±0.063	-0.454±0.275	-0.199±0.656		
	χ^2_{pos}	χ^2_{flux}	χ^2_{lens}	χ^2	
6	1560	46.2	436	2040	
7	5.3	10.3	22.0	37.6	
8	3.5	11.3	1.2	16.0	

Table 4.5: Best fit lens model parameters and error statistics for lens models 6, 7, and 8 using the point source solver. The errors are 95 percent confidence levels. The lens positions are measured relative to component B. Model 6 has five degrees of freedom and models 7 and 8 have three degrees of freedom.

the $\cos 3\theta$ model. Figure 4-12 shows the change in χ^2 as a function of the B flux. We see that a change in flux of 3 mJy (5 percent) changes the χ^2 by $\lesssim 3$. We also find the change in the converged lens parameters are well below the 95 percent confidence intervals listed in Table 4.4. Therefore, we do not believe the variability level measured by Moore & Hewitt (1995) significantly affects the lens modeling. It is interesting to note the minimum is at a flux of 2 mJy lower than the measured flux, which indicates possible variability in the system; although the lens model is probably not perfect.

The two models which best fit the system have ellipticities due to mass outside the ring of images. However, the HST images of the galaxy show an ellipticity of ~ 0.3 (Falco 1995). Both models also indicate mass towards the position of object X. Angonin-Williams *et al.* (1994) stated that object X was most likely a galactic star, although the Hubble Space Telescope observations show no evidence for a compact stellar object (Falco 1995). Diffuse emission is seen around the position of object X, supporting the interpretation of object X as a galaxy. Furthermore, the Hubble

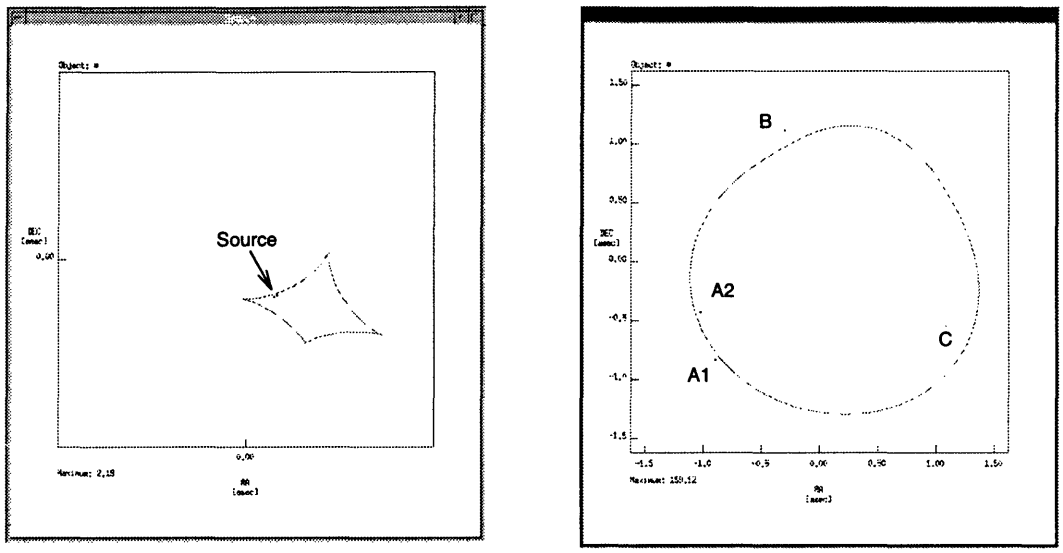

Figure 4-11: Panel (a) shows the reconstructed source and tangential caustic and and Panel (b) shows the point images and the tangential critical for Model 8. The image in panel (a) is a factor of four smaller in each dimension than the image in panel (b). Due to the finite pixel size, the source components do not lie on top of each other.

observations do not show the lensing galaxy to be distorted significantly towards the northwest, although rigorous analysis of the lens has yet to be done (Falco 1995). We find that the $\cos 3\theta$ model fit the system better than the two SIS plus external shear model. However, the structure of both lens models suggests a similar interpretation. The $\cos 3\theta$ model places the "perturbing" mass external to the lensing galaxy, causing the same distortions as the two component SIS model. We believe that object X does influence the lensing geometry of the system and should be taken into account in further modeling of the system.

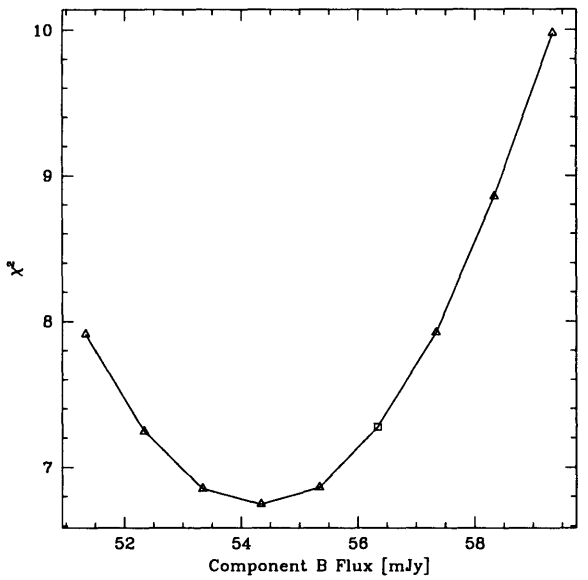

Figure 4-12: Plot of χ^2 versus the flux of component B. We used the $\cos 3\theta$ lens model. The χ^2 is the value after optimizing all the lens model parameters. The $\square$ symbol indicates the measured flux of component B used in the lens inversion.

Chapter 5

5 GHz VLBI Observations

5.1 Observations

On June 7th, 1992, MG0414 was observed at 5 GHz with an array of ten telescopes: Effelsberg, Greenbank, Haystack, Medicina, the phased-VLA, and 5 VLBA[1] telescopes: Fort Davis, Kitt Peak, Los Alamos, Owens Valley, and Pie Town. The European VLBI Network (EVN) stations observed from 12:00 UT through 16:00 UT, when MG0414 set. The North American stations observed from 12:00 UT through 23:00 UT. At each non-VLBA station, the observation was made with the Mark III VLBI recording system in mode B using a 28 MHz bandwidth (Rogers 1983). The VLBA stations recorded the signals using the VLBA system in a Mark III mode B compatible format.

Since the MG0414 components are separated by no more than 2″, they were within the primary beams of all the single dish telescopes. The phased-VLA primary beam is the interferometric beam and not the primary beam of each individual VLA antenna. We observed the source using the compact D-north-C array configuration, resulting in a beam size of $\sim$ 10″. Therefore, we observed all of the MG0414 components simultaneously.

[1]The Very Long Baseline Array is part of the National Radio Astronomy Observatory which is operated by Associated Universities, Inc. under co-operative agreement with the National Science Foundation.

The observation was divided into blocks of approximately one hour in length, each corresponding to four 13 minute tape passes. At the start of each block, we observed 0423-013 (J2000), a redshift $z = 0.9$ BL Lac object, as a bright calibrator. Previous VLBI observations of 0423-013 revealed little structure at the 1 milliarcsecond level (Wehrle *et al.* 1992). Although the flux of 0423-013 has varied dramatically, it usually remains greater than 1 Jy, which allows us to use short 90 second scans of 0423-013 in the phase calibration and "clock finding" (see Section 5.2). The remainder of each block of time was dedicated to observing MG0414.

Effelsberg, Greenbank, Haystack, and Medicina required short interruptions to measure system and antenna temperatures. Even though the VLA and the VLBA stations measure both as the observations proceed, we introduced a short break between each block in the schedules at all the stations to keep the tapes synchronized.

Some difficulties were experienced during the observations. Before the observation, the formatter in the Greenbank Mark III data acquisition rack was left disconnected. The formatter provides accurate timing information to the tape recorder; therefore, the data from Greenbank could not be correlated. The recording head in the Kitt Peak VLBA tape recorder jammed at 19:42 UT, resulting in a loss of data on all Kitt Peak baselines through 22:06 UT.

5.2 Correlation

The data tapes were shipped to the Haystack Observatory for correlation on the Mark III processor. Each station provided an observing log, calibration information, and data for the *a priori* correlator model (see Section 2.6.2). The geometric information, such as the exact location of each telescope, was known through the results of previous geodesy experiments. The tropospheric moisture content was estimated from the weather information in the observing log.

The Mark III processor correlates each station pair at eight residual delays (i.e. eight delays with respect to the correlator model) from $-\frac{3}{4}\mu$s to 1μs. Instrumental effects must be known to this accuracy to measure the complex response of the program

source. We used the instrumental offsets (known as "clock" offsets) found from other observations nearby in time as starting values. To provide a strong unambiguous signal at the correct offsets, we correlated a 0423-013 scan near the midpoint of the observation. If a strong peak was not found (i.e. the "clocks" were off by more than $\pm 1\mu$s), we varied the offsets until the peak shifted into the response window. This procedure is known as "finding clocks." Correlating scans at the beginning and end of the observation, we found the clock offsets were stable throughout the observation, and these values were introduced into the correlator model as constant instrumental offsets.

The delay beam for the longest baseline ($\sim 10^8\lambda$) is $3\farcs5$, which results in more than a 10 percent amplitude reduction for objects $1''$ from the delay center. Even though all the components in MG0414 were observed simultaneously, the size of the delay beam required that the observation be correlated at multiple delay centers to prevent bandwidth smearing (see Section 2.4.1). We chose three positions at which to correlate the MG0414 scans: At the midpoint between A1 and A2, at the position of B, and at the position of C. The delay center coordinates, shown in Table 5.1, were obtained from high-resolution 15 GHz VLA observations of MG0414 (Katz & Hewitt 1995). We chose to correlate at a position between A1 and A2 rather than at both A1 and A2 to reduce the correlation time (approximately 3 days per delay center). The bandwidth smearing due to the $0\farcs25$ offset of A1 and A2 from the delay center resulted in well under a one percent amplitude reduction.

Delay Center	α	δ
A1/A2	$04^h\ 14^m\ 37.7759^s$	$05^o\ 34'\ 42.5415''$
B	$04^h\ 14^m\ 37.7322^s$	$05^o\ 34'\ 44.2690''$
C	$04^h\ 14^m\ 37.6411^s$	$05^o\ 34'\ 42.6390''$
0423-013	$04^h\ 23^m\ 15.8006^s$	$-01^o\ 20'\ 33.0627''$

Table 5.1: Correlation delay center coordinates. The MG 0414+0534 positions are taken from Katz & Hewitt (1995) and the 0423-013 position is from the VLA Calibrator Manual. All positions measured with respect to the J2000 coordinate system.

The Mark III correlator calculates the complex visibility function from the signals

recorded at each station. For each station pair, the correlator introduces a delay for one station ranging from -$\frac{3}{4}\mu$s to +1μs in increments of $\frac{1}{4}\mu$s. For each of these eight delays, the two station signals are corrected by the correlator model and multiplied together. At this point, the phase changes are small enough so the visibilities can be averaged over an accumulation period of 2 seconds. The integration increases the signal-to-noise ratio in each visibility point and also significantly reduces the total size of the data set. The correlated data are archived onto digital-audio-tapes (DATs) at the Haystack Observatory for further processing.

5.3 Calibration

The MG0414 and 0423-013 data sets were imported into the NRAO Astronomical Image Processing System (AIPS) for fringe fitting and amplitude calibration. Each data set corresponding to a single delay center was processed independently. The subsequent sections describe the calibration procedures. The AIPS tasks FRING and ANCAL were used to perform the global fringe fitting and amplitude calibration.

5.3.1 Fringe Fitting

At most VLBI stations, a phase-calibration signal is injected into the signal to measure the time-variable instrumental delays. However, at the time of the observation, the VLBA stations had not been equipped with the phase-cal systems. Since 0423-013 provided an excellent calibration source, we performed a "manual phase-calibration" by fringe fitting for only the delay in each frequency channel (single-band delay) on scans of that source. In addition, differences between the Mark III and VLBA electronics cause a 120 degree phase shift between the upper and lower sideband signals of each frequency channel on baselines which include one Mark III station and one VLBA station. We compensated for this phase shift by solving for each sideband separately in the manual phase-calibration.

Since no 0423-013 scans were available in which all stations were present, we chose to calibrate using the scans at 14:36 UT and 15:51 UT. Fort Davis was chosen as the

reference antenna since it was present in both scans and operating well. The delay solutions for stations common to both scans were found to be consistent. The solutions were applied throughout the entire observation. We verified that the instrumental delays did not change during the observations.

We fringe fitted the 0423-013 scans using a point source model for the source. We used the entire scan length ($\sim$ 90s) for the solution. To prevent large phase errors due to weak signal detections, we required every delay-rate solution to have a signal-to-noise ratio larger than seven on at least three baselines.

In order to fringe fit the MG0414 scans, a model of the source structure was necessary. Since a change in the delay or rate shifts the direction at which the interferometer points, a source containing multiple compact components will have multiple peaks in the response as a function of delay and rate. These peaks are convolved with the delay beam and, in the case of MG0414, are close enough such that the overlapping beams cause the peaks to shift relative to the true delay and rate values. For that reason, we divided the MG0414 data by a model of the source structure, thereby removing phase contributions from the source structure. The correct delay and rate were then found at the position of the response peak.

The model was derived from the same 15 GHz VLA observations of MG0414 used to determine the delay center positions (Katz & Hewitt 1995). The model consisted of four point sources at the positions of the components (See Table 5.2). Since the flux ratios appear to be consistent across many radio frequencies (Katz & Hewitt 1995), we used the 15 GHz flux ratios to set the relative fluxes of the point sources in the model. To set the absolute flux scale of the model, we fixed the B component flux to be equal to that measured at 5 GHz by Hewitt *et al.* (1992). We fringe fitted the MG0414 data sets using a four minute solution interval. As with 0423-013, we required a signal-to-noise of seven on at least baselines for a valid solution.

5.3.2 Amplitude Calibration

In contrast to the VLA, VLBI observations use telescopes with different properties, so the measured amplitudes of the complex visibility must be calibrated. All stations

Component	$\Delta\alpha$ arcsec	$\Delta\delta$ arcsec	Flux Ratio	Flux mJy
A1	0.591	-1.933	2.591	347.19
A2	0.726	-1.529	2.287	306.46
B	04 14 37.72789	05 34 44.2750	1.000	134.00
C	-1.375	-1.634	0.369	49.45

Table 5.2: Four point source model of MG 0414+0534 used for the global fringe fitting. The positions and flux ratios are relative to B. The absolute positions and relative fluxes were obtained from Katz & Hewitt (1995) and the absolute flux level was determined from Hewitt *et al.* (1992). All positions are measured with respect to J2000 coordinates.

provided system temperature measurements during the observation. On Effelsberg baselines, the gains were calibrated using antenna temperature measurements. The Haystack, Medicina, and VLBA stations relied on established gain curves as a function of elevation, and *a priori* source fluxes. The VLA records both VLBI and VLA formats simultaneously and we therefore used the VLA observation to measure the total source fluxes during the observation. We found the flux of 3.9 Jy for 0423-013 and 864 mJy for MG0414. The VLA was calibrated using the provided ratios of antenna temperatures to system temperatures measured during the observation.

5.4 Image Reconstruction

The editing and mapping procedures were performed entirely within the program Difmap[2]. Since Difmap can only process single frequency channel data, the data sets were averaged over frequency, then copied from AIPS into Difmap.

5.4.1 Editing

When observing at low elevations, the atmospheric distortions become significant and cause large phase errors. Therefore, we applied a 15 degree elevation cutoff to

[2]Difmap version 1.2 was written by Martin Shepherd, and is part of the Caltech VLBI Software Package.

the data. Furthermore, each baseline was edited to remove any outlier points which indicated antenna-based errors. For example, between 19:19 UT and 19:23 UT, all visibilities on VLA baselines had zero amplitude and were removed.

During the first third of the observing session, the amplitudes on all Haystack baselines dropped dramatically. Figure 5-1 shows the visibility amplitude for 0423-013 on some Haystack baselines; these should be approximately constant since the source is compact. After 13:00 UT, the 0423-013 scans show amplitudes of ≤ 0.5 Jy, far less than the 3.9 Jy measured with the VLA. The cause of the amplitude drop was not found and since there were not enough good scans on the calibrator to characterize the amplitude change over all time, Haystack data were discarded.

A "u-v crossing point" is the point of intersection in the u-v plane where the tracks from different baselines overlap. At these points, the different baselines should measure the same visibility and, therefore, can be used to check the visibility amplitudes. Typical VLBI amplitude errors are of order 10 percent. However, we found Effelsberg low by a factor of 9.4 and Medicina high by a factor of 2.1. Omitting these stations from the calculation, we found corrections of at most 22 percent on the remaining stations. Due to the large errors and the fact that the MG0414 visibility amplitudes indicate significant structure on angular scales much larger than those probed by the sparse transatlantic baselines, we chose to include only the VLA and VLBA stations in the MG0414 imaging.

During image reconstruction, the flux in the model consistently under-represented the measured flux on the Pie Town-VLA baseline, leaving large oscillating features in the residual image. This short baseline—approximately three times shorter than every other baseline in the observation—is sensitive to lower level flux emission which is resolved out on the longer baselines. Therefore, we removed this baseline from the mapping.

As a result of the editing, approximately 40 percent of the data were discarded. The final u-v coverage and dirty beam for the MG0414 data set shown in Figure 5-2.

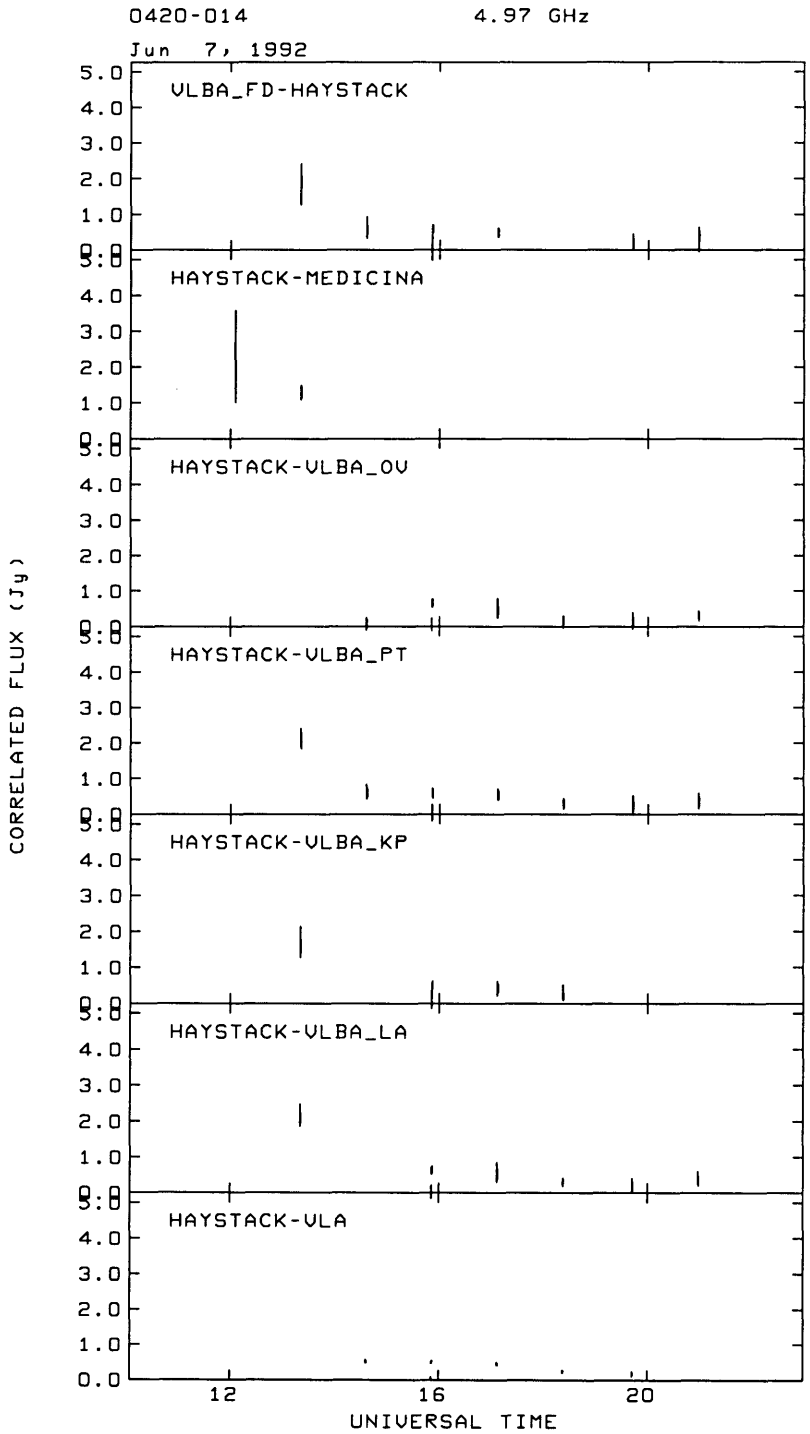

Figure 5-1: Visibility amplitude for 0423-013 (J2000) on Haystack baselines. The amplitudes dramatically drop after 13:00 UT.

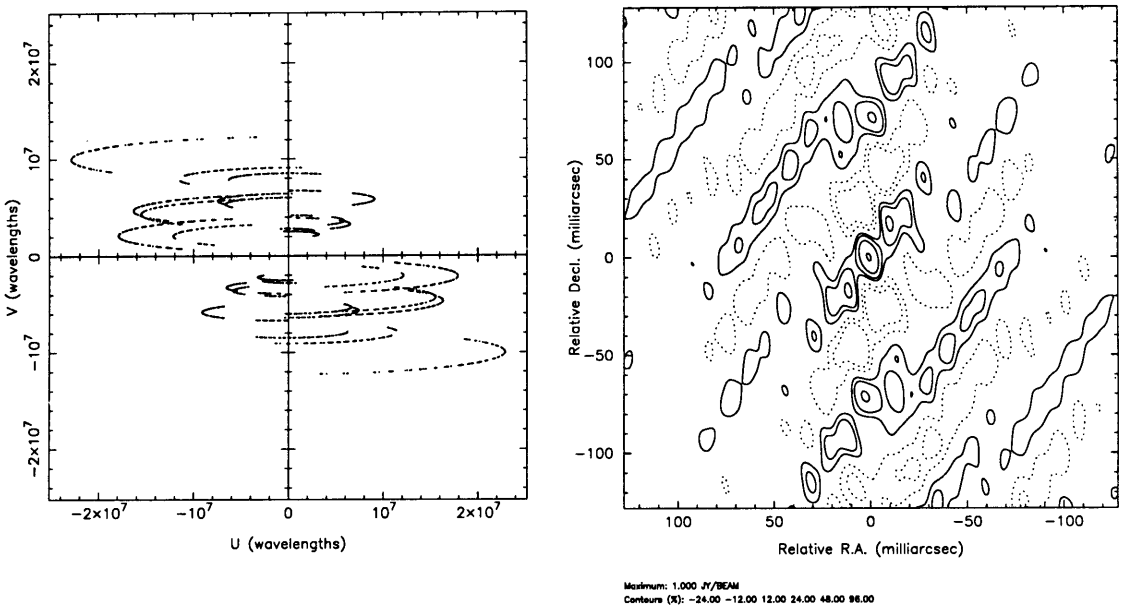

Figure 5-2: The left panel shows the u-v coverage and the right panel shows the dirty beam for the 5 GHz (λ6cm) observation of MG 0414+0534 after the data were edited. To produce the dirty beam, the data were uniformly weighted with a u-v box size of 3 pixels. The FWHM of the central lobe is 17 mas by 8 mas. The largest sidelobe is 50 percent of the peak.

5.4.2 Mapping Procedure

Since the phases were not calibrated, a phase self-calibration was necessary. For 0423-013 scans, a point source model was used as the initial model. Unlike most VLBI sources, the MG0414 system is not centrally peaked, so a point source is not an adequate starting model for the source structure. Instead, we initialized the antenna phases with the four component model used in the fringe fitting.

To reconstruct the image, we used the "difference" mapping procedure. The "difference" image is the residual map that remains after subtracting the clean component model from the visibility data. We identified the location of flux in the difference map, and only regions believed to contain flux were cleaned, constrained by tight clean boxes. We subtracted only a small number of components during each clean cycle to reduce the possibility of "freezing" incorrect clean components into the model. Af-

ter a cleaning cycle, we self-calibrated the data and subtracted the new components from the visibilities. The residual data were then Fourier transformed to produce the "difference" map for the next iteration. The procedure was repeated until the residual image no longer contained any flux. The exact procedure is outlined below with Difmap commands capitalized:

1. Calibrate visibility phases (STARTMOD).
2. Phase Self-calibration/Clean Block:
   (a) Clean (CLEAN) with tight clean boxes around regions of real flux, creating the current clean component model.
   (b) Self-calibrate (SELFCAL) the visibility data adjust phases only using the combined established and current clean component models.
   (c) Subtract the current model from visibility data, incorporate the current model into the established model, and create new "difference" image (MAPPLOT).
   (d) Repeat until peak in the "difference" map no longer decreases or the self-calibration solutions start to diverge.
3. Perform a full amplitude and phase self-calibrate (SELFCAL) with the established model.
4. Reduce the amplitude self-calibration solution interval by half. Repeat Self-calibration/Clean Block if the solution interval is not below 30 minutes.
5. Perform a final amplitude and phase self-calibration using the established model and a solution interval equal to the integration period.

The first amplitude self-calibration sets an overall scale for each station over the entire observation. In other words, the amplitude self-calibration solution interval is equal to the length of the observation. Because amplitude variations, such as those due to cloud cover or antenna elevation, generally change on timescales much longer

than the integration period, we smoothed the gain amplitudes over time. In addition, we ended the cleaning cycles when the amplitude self-calibration solution interval dropped below 30 minutes.

We created the final images by convolving the established clean component model with the clean beam and adding the residual image. The noise was estimated by measuring the root-mean-square (rms) value in empty regions of the final image.

5.4.3 0423-013

Since 0423-013 is a BL Lac object and an optically violent variable (OVV), we needed to check the level of variability during the observation. We divided the VLA observation of 0423-013 into two hour segments. We measured differences up to 2 percent in the integrated flux over the duration of the observation, which is consistent with the level of amplitude errors at the VLA. We, therefore, used the entire data set to image 0423-013. Figure 5-3 shows the final VLBI image of 0423-013 produced using the image reconstruction procedures described above. The data were uniformly weighted using a u-v box size of 3 pixels, yielding a resolution of 20.2 mas by 7.6 mas.

The data are consistent with a 3.6 Jy point source. The VLA observation measured a total flux of 3.9 Jy, indicating amplitude calibration errors at the 10 percent level. With the limited number of antennae and scans on 0423-013, amplitude errors at each station can more significantly affect the reconstructed zero-spacing flux of the source. We constrained the amplitude corrections to maintain the current total flux in the source. However, we found large ($\gtrsim$ 10 percent) amplitude errors, causing the current total flux to underestimate the flux in the system.

5.4.4 MG 0414+0534

To reduce the computation and editing time, the MG0414 data were averaged into 30 second integration intervals. Time-average smearing effects were not significant, since we included only the shorter baselines of the VLA and VLBA stations. Although the data were correlated at three delay centers, the delay beam was large enough

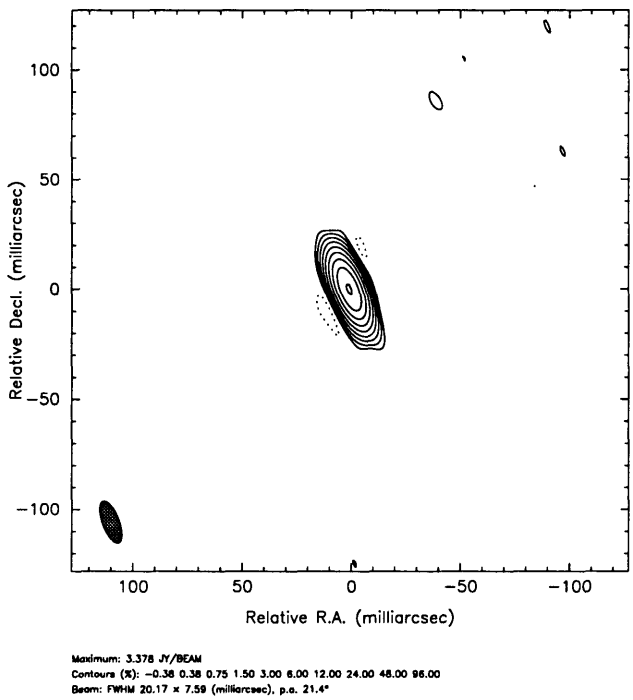

Figure 5-3: Final 5 GHz image of 0423-013 (J2000). The data have been uniformly weighted with a u-v box size of 3 pixels. The size of the restoring beam is given in the lower left corner.

to include correlated flux from more than one component. Therefore, we needed to image all four components in each data set. In order to adequately sample the beam ($\gtrsim$ 4 pixels across the central lobe of the dirty beam) and include all the correlated flux, a single image would have required over 2000^2 pixels, mostly empty. Although Difmap does not have the ability to map multiple fields simultaneously, Difmap does provide the ability to shift the position of the map (phase) center on the sky. By modulating each visibility with $e^{2\pi i(\vec{u}\cdot\Delta\vec{x})}$, where $\vec{u}$ is the projected baseline corresponding to the visibility point, the location of the phase center is shifted by $\Delta\vec{x}$. Using this feature, we mapped multiple fields by shifting to the location of each component during each cleaning cycle. This method of multiple field cleaning is susceptible to biases caused by distant sidelobes in the dirty beam corrupting the positions of the peaks. However, the components were separated by large enough distances so that this was not a significant problem.

Figure 5-4 shows the final VLBI maps of the MG0414 components. The image of

each component was created from the data correlated at the delay center located nearest that component. As in the 0423-013 mapping, the data were uniformly weighted with a u-v box size of 3 pixels. Although there were slight differences in each data set due to lost data during correlation, the resulting beam sizes were all approximately 17 mas by 8 mas. We chose a linear pixel size of 1 mas. The image parameters are given in Table 5.3. The position ($\Delta\alpha$, $\Delta\delta$) is the location of the peak component in each image relative to the peak in B.

Both A1 and A2 are dominated by a strong compact component. In A1, a second extended component lies to the east of the peak with ten percent of the flux of A1. The total integrated flux of A1 is 243 mJy. The A2 image has a more complex structure. The peak flux is 121 mJy/Beam. Along the NE-SW direction, the image appears stretched with a bright component to the north and a possible fainter extension to the south. The object directly to the south of the central peak is significantly brighter than the noise level in the image. However, this component lies directly on a strong sidelobe ($\geq$ 50 % of the central lobe; see Figure 5-2) of the peak component in A2. The total integrated flux of A2 is 219 mJy.

The image of B shows a strong central component with extensions to the east and west. The total integrated flux is 77 mJy with a peak flux is 38 mJy/Beam. The position angle of the extended emission is 116 degrees, in excellent agreement with the elongation of B in the 15 GHz VLA observations of MG0414 (Katz 1994). The structure in B also agrees with the structure seen the 5 GHz MERLIN observations of MG0414 (Patnaik 1993).

The image of C shows a single faint component. Although this data set has been correlated at the position of C, the delay beam is large enough to include correlated flux from A1, A2, and B. Therefore, these brighter components must be reconstructed well before C is detectable. However, the other components are smeared due to the bandwidth and time-averaging, resulting less reliable reconstructions. From these effects, we believe this detection of C is questionable.

Katz & Hewitt (1995) measured 5 GHz integrated fluxes of 401, 362, 156, and 58 mJy for A1, A2, B, and C, respectively. The integrated fluxes in Table 5.3 show

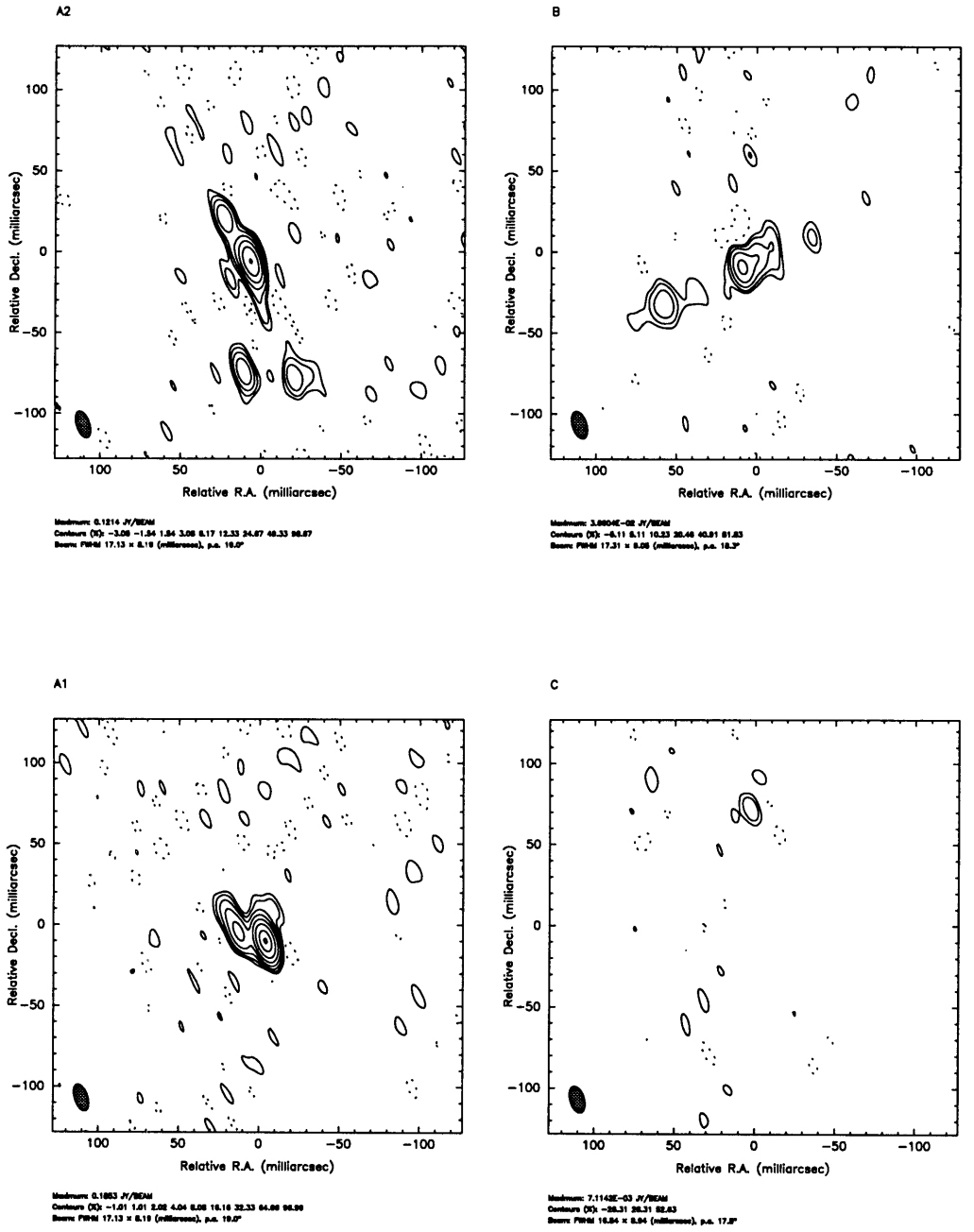

Figure 5-4: Final 5 GHz image of each component in MG 0414+0534. Clockwise from the bottom left, the images are A1, A2, B, and C. The data have been uniformly weighted with a u-v box size of 3 pixels. The contour levels are -2, -1, 1, 2, 4, 8, 16, 32, 64, and 96 percent of the peak flux in A1 (185 mJy/Beam). The size of the restoring beam is shown in the lower left corner of each panel. The image parameters are given in Table 5.3.

Component	$\Delta\alpha$ arcsec	$\Delta\delta$ arcsec	Peak mJy/Beam	Integrated mJy	σ mJy/Beam	VLA Flux mJy
A1	+0.580	-1.947	186.2	242.5	1.4	401
A2	+0.725	-1.541	123.7	219.2	2.3	362
B	–	–	37.7	76.7	1.6	156
C	-1.345	-1.454	9.1	9.1	1.5	58

Table 5.3: Parameters from the 5 GHz VLBI images of MG 0414+0534. The positions ($\Delta\alpha$,$\Delta\delta$) are measured from the peak in the image to the peak in the B image. σ is determined in empty regions of the final images. The 5 GHz VLA integrated fluxes are taken from Katz & Hewitt (1995).

that the VLBI images only recovered approximately half of the flux. The reconstructed 0423-013 image indicates the amplitude errors are at the 10 percent level. The excess flux on the on the Pie Town-VLA baseline clearly indicate that the VLBI images do not reconstruct all the flux in the system. Moreover, the 5 GHz MERLIN observations (Patnaik 1993) show more extended emission than detected in our VLBI images. Therefore, we conclude that the VLBI observations resolved out the low surface brightness emission.

The peak positions in A1 and A2 relative to the peak in B are in good agreement with the relative positions measured from the 15 GHz VLA observations. However, the relative position of component in C is incorrect by larger than the 15 GHz VLA beam. We, therefore, conclude that the detection of C is spurious.

5.5 Image Reliability

The primary goal of these data is to further constrain the gravitational lens inversions of MG0414. Hence, we examined the reliability of the final images in three ways. We checked for differences in the image reconstructions as a result of minor changes in the data reduction procedure. We also examined the differences between the three data sets corresponding to different delay centers. Second, we tested the stability of the reconstructions to changes in the u-v sampling. Our final test was to check the consistency of the final reconstructions with the lensing hypothesis, by mapping clean

components from one image through the lens to the other image locations.

5.5.1 Consistency within the Data Sets

We tested the reliability of some of the components in the images by not including them inside clean boxes during the reconstructions. This experiment tests whether these components result from errors in the image reconstruction. Features due to real flux should remain in the residual image convolved with the dirty beam. Errors in the reconstruction should be corrected during self-calibration. We found that the reconstructions of A1 and B were consistent. All the components in A2 were present in the residual image, even though they were not included within any clean boxes. However, their fluxes were not as stable as those in A1 and B.

We checked that the reconstructed images from all the delay center correlations gave consistent results. Although rigorous comparison of the fluxes and structure was not possible due to bandwidth and time-average smearing effects, the images from each of the three data sets revealed the same general structure. These tests do not fully explore the systematic effects since the data sets are essentially the same.

5.5.2 Time Segmentation

We tested the reliability of the reconstructions by segmenting the data sets in time and comparing the results with that from the entire data set. The time segmentation serves to change the u-v sampling function. Real structures in the image should not be affected by the structure of the dirty beam. On the other hand, the smaller data set provides fewer constraints on the image reconstructions. We found that splitting the data in half caused significant problems in the image reconstruction procedures. The smaller data set led to unreliable reconstructions because of the poor u-v coverage. The visibility data before 16:00 UT were noisier than the rest of the observation, so we chose to map the data from 16:00 UT through 23:00 UT.

Since we do not have a reliable detection of C, we focus only on the reconstructions of A1, A2, and B. Figure 5-5 shows the reconstructed images of A1/A2 and B. The

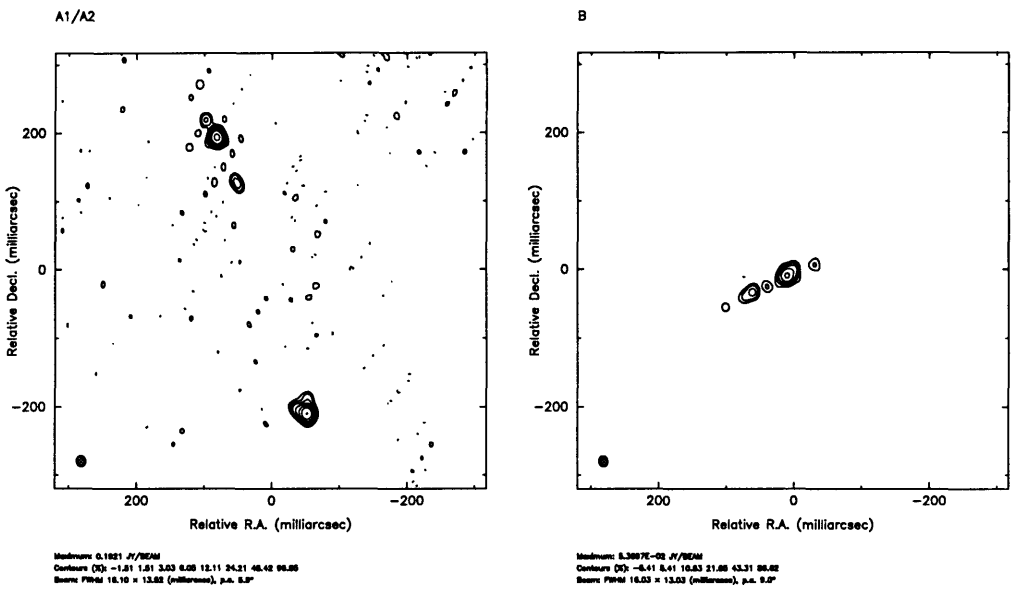

Figure 5-5: Final 5 GHz images of A1/A2 and B using data from 16:00 UT to 23:00 UT. The data have been uniformly weighted with a u-v box size of 3 pixels. The contour levels are -3, -1.5, 1.5, 3, 6, 12, 24, 48, and 96 percent of the peak in A1 (193.8 mJy/Beam). The size of the restoring beam is shown in the lower left corner of each panel.

image parameters are shown in Table 5.4. The beam FWHM is now 16 mas by 12 mas. As before, the segmented data were uniformly weighted with a u-v box size of 3 pixels. We increased the linear pixel size to 2.5 mas so that the images of both A1 and A2 fit within the same map. The structure in A1 is similar to the structure seen before. The larger beam size causes the component to the east to merge with the central peak. The faint extension to the north is also seen, indicating it is probably real. The peak flux in A1 increased to 194 mJy/Beam, although the total integrated flux has dropped by seven percent. The A2 image shows differences in its reconstruction. The integrated flux in A2 is well below that reconstructed using the entire data set. The higher noise level in the A1/A2 image is due to residual sidelobes caused by errors in the reconstruction. The fainter extension to the south and the component directly south of the peak are not present and probably not real. The other components in A2 are all present, although with different relative strengths. The fluxes for the

northern component and the component to the southwest do change; however, both components remain above the noise level. We conclude these components are probably real.

This reconstruction of B results in a lower overall noise level than in the entire data set. The peak is 54 mJy/Beam and the total integrated flux in B has increased to 114 mJy. The noise level has decreased to 0.8 mJy/Beam since more of the lower level emission has been correctly reconstructed, reducing the level of sidelobes extending to the empty regions of the image. The structure is the same as the structure seen previously, except with more low-level emission present. Hence, we believe the structure in VLBI image of B is real.

Component	Peak mJy/Beam	Integrated mJy	σ mJy/Beam
A1	193.8	224.8	1.8†
A2	116.2	155.9	1.8†
B	53.7	113.5	0.8

Table 5.4: Parameters from the 5 GHz VLBI images of MG 0414+0534 using only the data from 16:00 UT to 23:00 UT. σ is determined in empty regions of the final images. † The noise level for A1 and A2 was determined from the same image.

5.5.3 Consistency with Gravitational Lensing

We took advantage of the fact that MG0414 is a gravitational lens system to test the fidelity of the reconstruction. Since we expect the components of MG0414 to be distorted images of one another, we compared the reconstructions of the images by mapping them through a lens model and comparing the results. This test does not rigorously test the reconstructions, but rather verifies the coarse structure since we do not have a lens model which fits the system perfectly (see Section 4.1). We chose a generic lens that could reproduce the gross image geometry: the singular isothermal sphere in an external shear field model. Since the MG0414 components are resolved in the VLBI maps, the exact lens position relative to the components is not known

precisely. We convolve the A1 clean component model from the VLBI maps to the resolution of the 15 GHz VLA observation to find the offset of the peak in A1. If the various components in the VLBI images have different spectral indices, the position of the lens center will be incorrect. The lens model parameters are given in Table 5.5.

b	x	y	γ	θ_γ
arcsec	arcsec	arcsec		degrees
1.196	0.468	-1.290	0.081	-75.6

Table 5.5: Parameters for the singular isothermal sphere plus external shear lens model used to ray-trace the A1 clean component model. The lens position (x,y) is measured relative to B and x increases to the west. θ_γ is measured north through east.

We performed the ray-tracing with the Gravitational Image Tracing (GrIT) package. Since the A1 reconstruction appears reliable, we used the A1 clean components as the model of the true A1 image. Mapping back to the source plane, we reconstructed the source plane brightness distribution, given in the upper right panel of Figure 5-6. Because of the finite pixel size, the fluxes will not be preserved in the ray-tracing. The effective resolution of the source is increased by the magnification of the lens. The large ellipticity of the restoring beam is caused by the strong magnification in only the tangential direction at A1. The reconstructed source has been convolved with the magnification-corrected clean beam. The peak is 0.″384 west and 1.″224 south of component B. The unlensed source is consistent with a core-jet structure; however, multifrequency or polarization observations are needed to distinguish a core from a jet.

We mapped the source brightness distribution to the four image positions. The reconstructions are given in Figure 5-6. We included A1 to check for consistency in the ray tracing and found A1 to be reconstructed correctly. The A2 image is commonly expected to be a mirror image of A1, since they are near the tangential critical line. However, we see that the A2 component appears significantly different from A1. The two components in A1 are widely separated in A2. The relative separation between A1 and A2 is smaller by $\sim$ 50 mas indicating an error in the lens position. The

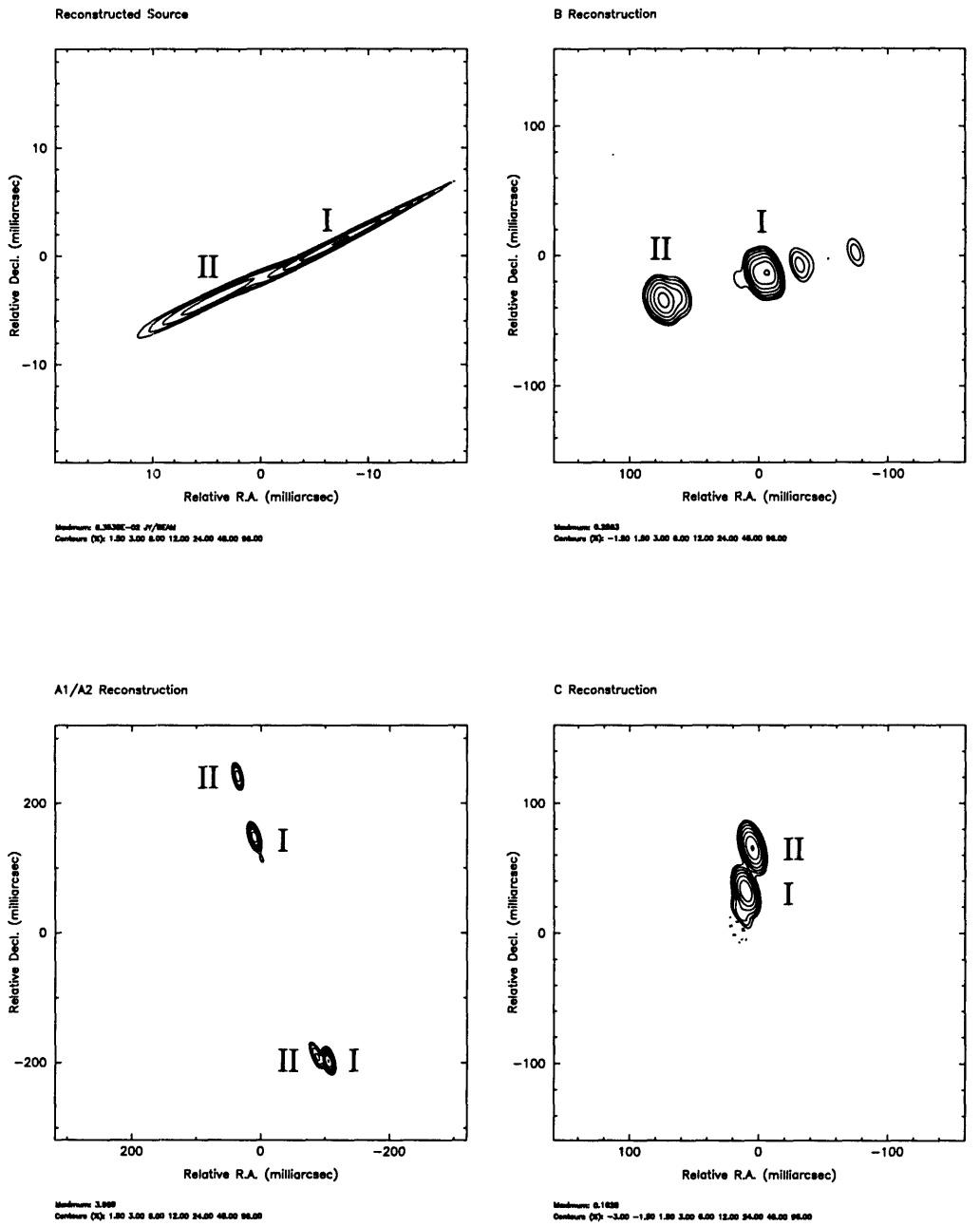

Figure 5-6: The upper right panel shows the reconstructed source brightness distribution of MG0414 from the clean component model of A1. The reconstructed source has been convolved with the lens distorted clean beam. The other panels contain the reconstructed images of MG0414 using the reconstructed MG0414 source. The source and images were created using the Gravitational Image Tracing (GrIT) package. The brightest two components are indicated in each panel with the Roman numeral: I is the brightest component and II is the second brightest component at A1.

A2 reconstruction does not show the additional components seen in A2 VLBI image. The reconstruction of B does strongly resemble to the VLBI image of B, providing good evidence that MG0414 is a gravitational lens and that the VLBI image of B is reliable. The C component reconstruction shows two components; however, we do not have reliable detection of C in the VLBI images for comparison

We believe the VLBI images of A1 and B are reliable models of the true image, while some features of A2 are suspect. The ray-tracing of the A1 clean components suggest that the northern component in A2 is real and is associated with the eastern component in A1. The southern components and the lower-level emission are questionable in A2. Even though we have used a lens model which is known to fit the system poorly (see Section 4.1.2), the critical line structure about A1 and A2 is similar to that in $\cos 3\theta$ model, which was found to fit the system reasonably well. Therefore, we believe the changes in the A2 reconstruction indicate the final VLBI image is suspect. The reconstruction of C appears to be spurious because its position is not in agreement with the reliable VLA positions.

5.6 Lens Inversion

Since we have a lens model which fits the system (see section 4.2), we used the most reliable components from the VLBI reconstructions to further constrain the model. Our lens inversion method requires that we map point sources back to the source plane. Therefore, we chose the two brightest components from the VLBI images of A1. From the previous section, we found that these components are mapped to the central and northern components in A2 and the central and eastern components in B (See Figure 5-4). The positions and fluxes for the components are given in Table 5.6. The position errors were chosen to be approximately half the beam size for the primary components and equal to the beam size for the secondary components. The larger position uncertainties for the B components reflect the different magnification at B. The components have been stretched and, therefore, the positions of the components which map to those in A1 and A2 are less clear. Comparing the fluxes

between the segmented and nonsegmented data, we estimated a flux uncertainty of 10 mJy/Beam for the primary components. The larger 15 mJy/Beam error for the secondary components is because the secondary components are extended and more dependent on the reliability of the reconstruction.

Component	$\Delta\alpha$ arcsec	$\Delta\delta$ arcsec	σ_θ arcsec	Flux mJy/Beam	σ_f mJy/Beam
A1 primary	-0.577	-1.945	11	185.9	10
A1 secondary	-0.594	-1.939	14	39.0	15
A2 primary	-0.712	-1.543	11	122.3	10
A2 secondary	-0.728	-1.516	14	28.7	15
B primary	–	–	–	38.6	10
B secondary	-0.048	-0.023	22	13.8	15

Table 5.6: Input positions and fluxes from the VLBI images. The component positions are measured with respect to the B primary component.

We modified the error measure from Section 4.2 to include the secondary components,

$$\chi^2 = \chi^2_{pos_1} + \chi^2_{pos_2} + \chi^2_{flux_1} + \chi^2_{flux_2} + \chi^2_{lens} \tag{5.1}$$

where 1 specifies the primary component and 2 specifies the secondary component. Since the $\cos 3\theta$ lens model (model 4 from Section 4.2.1) was found to fit the VLA data, we focused on this parameterization.

We began by only modeling the primary components to test the consistency of the VLBI data with the VLA data. We started the minimization at the best fit model given in Table 4.4. We found a good fit to the system with a χ^2 of 0.2 and only one degree of freedom. The best fit model parameters are given Table 5.7.

We found the converged lens model parameters were consistent with those found using the 15 GHz VLA data. We expected that the B components may contribute the largest error since they were clearly resolved in the VLBI images. Using both the primary and secondary components, we found a reasonable fit to the system, with a χ^2 of 16 and seven degrees of freedom. The best fit parameters are shown in Table 5.7. The lens model parameters did vary, although the solution is consistent

	b arcsec	x_l arcsec	y_l arcsec	γ	θ_γ degrees
P	1.180±0.035	-0.473±0.030	-1.277±0.012	0.096±0.063	-5.1±4.1
P&S 1	1.135±0.080	-0.414±0.080	-1.248±0.030	0.097±0.043	-16.3±6.1
P&S 2	1.177±0.025	-0.472±0.024	-1.273±0.015	0.098±0.040	-4.8±3.9
P&S+C	1.181±0.010	-0.463±0.012	-1.258±0.008	0.083±0.017	-13.9±3.4
	$\epsilon/\beta b/\delta b^2$	$\theta_{\epsilon/\beta/\delta}$ degrees			
P	0.003±0.013	-6.1±25.7			
P&S 1	0.006±0.007	38.7±17.5			
P&S 2	0.003±0.006	-6.7±34.1			
P&S+C	0.004±0.004	36.1±7.4			
	χ^2_{pos}	χ^2_{flux}	χ^2_{lens}	χ^2	N_{dof}
P	0.001	0.2	0.1	0.3	1
P&S 1	7.9	2.7	5.8	16.4	7
P&S 2	0.002	0.5	0.1	0.6	3
P&S+C	22.1	2.0	1.1	25.2	9

Table 5.7: Best fit lens model parameters and error statistics for the $\cos 3\theta$ model on the 5 GHz VLBI data. P means only the primary components were fit. P&S 1 includes both the primary and secondary components were used in the inversion and P&S 2 includes the primary component and only the fluxes of the secondary component. P&S+C is identical to P&S 1 except that the VLA C position was added as a constraint. The errors are 95 percent confidence levels. The lens position is measured relative to the primary component in B. The position angles are measured north through east.

with the VLA model within its errors. We found the dominant contribution to the error to be in the positions of the secondary component. If we excluded the positions from the fit (see entry P&S 2 in Table 5.7), we found a good fit to the system with a χ^2 of 0.6 where $N_{dof} = 3$.

We found that without the position of the C component, the lens models had more freedom to fit the magnifications. However, the position of C no longer agreed with the VLA observation. We inserted the C component into the modeling by requiring that the peak position of C measured with the VLA traced back to the same source position as the other primary components (Model P&S+C in Table 5.7). We found a reasonable fit with a χ^2 per degree of freedom of 2.8. The constraints added by the

position of C constrained the lens model well. The final lens model parameters agree with those found using only the VLA data set.

We reconstructed the source brightness distribution by ray-tracing the clean component model of A1 back to the source plane using the GrIT package. Then, we mapped this source to the A1, A2, B, and C images. The reconstructed source and images for the P&S+C lens model are shown in Figure 5-7.

We see that the source is similar to that in Figure 5-6. As before, we mapped the source to A1 to test the accuracy of the ray-tracing and found no errors. The relative separations of the primary and secondary components for the data and best fit lens model are shown in Table 5.8. The relative separations between the primary

Component	$\left\vert\vec{x}_1^{data} - \vec{x}_2^{data}\right\vert$	$\left\vert\vec{x}_1^{model} - \vec{x}_2^{model}\right\vert$
	mas	mas
A1	17.7	18.2
A2	31.6	83.1
B	53.6	86.3

Table 5.8: The relative separations between the primary and secondary components for both the 5 GHz VLBI data set and best fit lens model.

and secondary components in the A2 and B images are rather large. However, we have made the approximation that the secondary component is point-like, which the VLBI image of B shows this approximation in incorrect. Furthermore, we are using the clean component model from A1, which was created using a 1 milliarcsecond grid. Since the directions of large magnifications at A1 and B are in orthogonal directions, the error at B would be approximately $\delta x \mu_B \simeq 10$ mas. However, this error should not significantly affect the A2 reconstruction, indicating some problems with the lens model or possible inconsistencies in the VLBI reconstruction of A2. The lens inversion should be performed with higher dynamic range VLBI data and within Visibility LensClean.

The 5 GHz VLBI data show the MG0414 system is consistent with the lensing scenario. We find the structure of VLBI images to be reasonably described by the

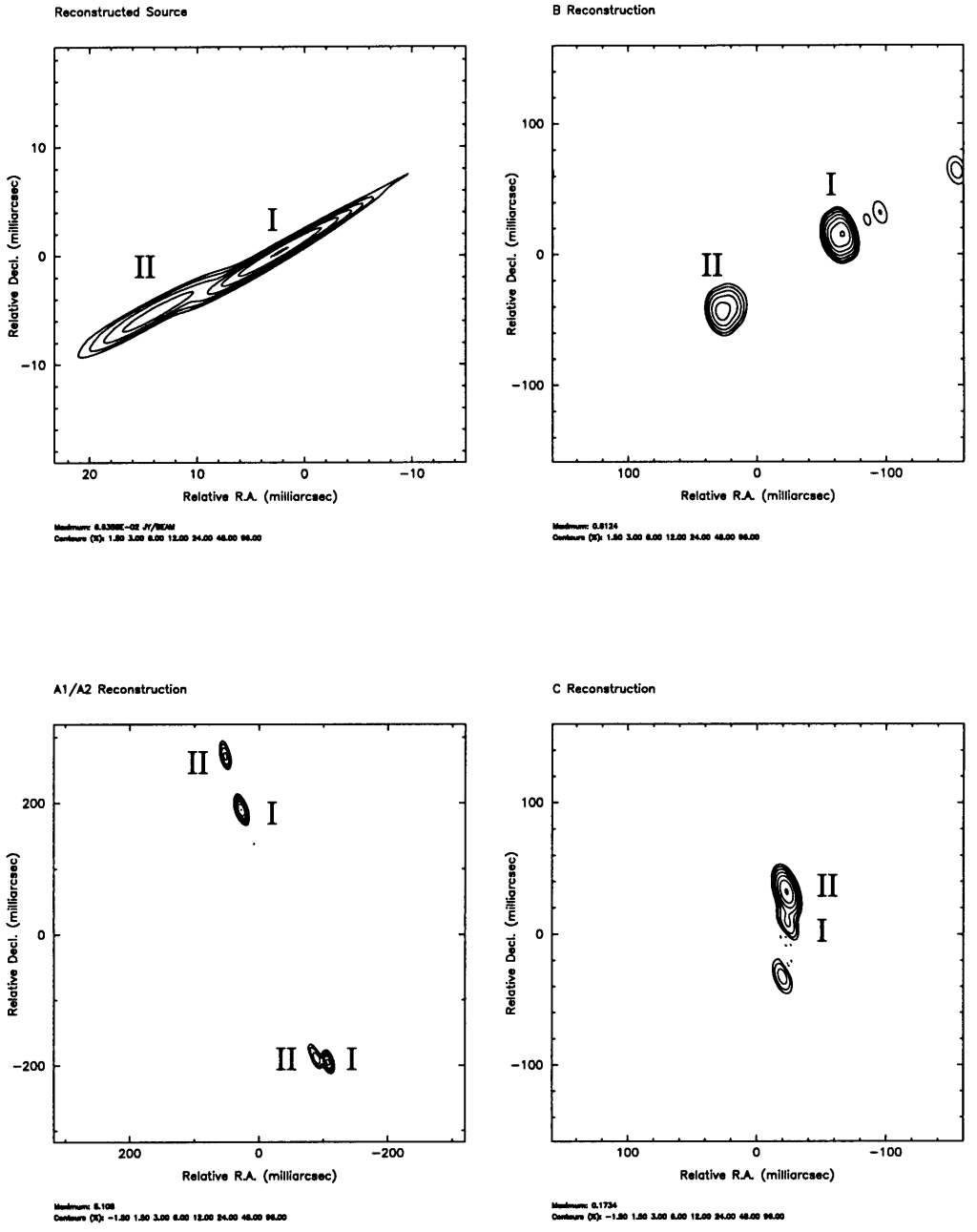

Figure 5-7: The reconstructed images for the best fit $\cos 3\theta$ model. The upper right panel shows the reconstructed source brightness distribution of MG0414 from the clean component model of A1. The reconstructed source has been convolved with the lens distorted clean beam. The other panels contain the reconstructed images of MG0414 using the reconstructed MG0414 source. The source and images were created using the Gravitational Image Tracing (GrIT) package. The brightest two components are indicated in each panel with the Roman numeral: I is the brightest component and II is the second brightest component at A1.

reconstructions from the clean component model of A1. Using the point source lens modeling procedure, we find the best fit lens model is consistent with that found using the 15 GHz VLA data set. Although we did not find an optimum fit to the VLBI image, the best fit model is less than 3σ from an optimal fit (i.e. $\chi^2/N_{dof} = 1$), assuming normally distributed errors. The two main sources of error are the reliability of the secondary components and the resolved components in B. The secondary components are extended and fainter than the primary components, so their exact positions and fluxes are more uncertain. The poor quality of this VLBI observation along with the sparse sampling in the u-v plane resulted in low dynamic range images of the MG0414 components. The VLBA will increase the dynamic range since the array has been used over the past years and the observational problems have been greatly reduced. Reliably reconstructing the low-level diffuse emission in MG0414 will provide valuable constraints on the lens model magnification structure. Second, the VLBI images clearly show the components to be extended. Therefore, errors result from using the peak flux and position of each component because the components are resolved at B, but mostly unresolved at A1 and A2. These finite resolution effects are the key reason for the development of LensClean. We believe applying Visibility LensClean to the VLBI data would significantly reduce this error.

Chapter 6

Conclusions

6.1 Lens Inversion Results

There is little doubt remaining that MG0414 is a gravitational lens system. The geometry of the system originally suggested that the source of the gravitational potential was a single isolated galaxy. However, using the Visibility LensClean procedure, we find that the system is not fit well by a simple lens model. Approximating the lens galaxy by only the first two terms in a multipole expansion, we find the observed data are not consistent. Although this type of lens model is successful in fitting the lens galaxy in MG 1654+1346 (see Section 3.6.2), Chen *et al.* (1995) find that the MG 1131+0456 lens is also not well described by this approximation.

By adding another term to the multipole expansion, we find a lens model which fit the system reasonably well but not perfectly:

$$\phi(\vec{r}) = br + \frac{1}{2}\gamma r^2 \cos 2(\theta - \theta_\gamma) + \beta r^3 \cos 3(\theta - \theta_\beta). \tag{6.1}$$

The best fit model parameters are given in Table 6.1. The HST I-band and V-band images show the lens galaxy is elongated with a position angle of $\sim 45^o$ (Falco 1995). The emission from the galaxy is limited to approximately $\simeq 0\farcs5$, yielding little information about the structure of the galaxy outside the circle defined by the images. However, we find the system is best fit with a lens model containing a circularly sym-

	b arcsec	x_l arcsec	y_l arcsec	γ	θ_γ degrees
Best Fit	1.181±0.010	-0.463±0.012	-1.258±0.008	0.083±0.017	-13.9±3.4
	$\epsilon/\beta b/\delta b^2$	$\theta_{\epsilon/\beta/\delta}$ degree			
Best Fit	0.004±0.004	36.1±7.4			

Table 6.1: Parameters for lens model which best fit the MG 0414+0534 system, the singular isothermal sphere plus external shear and $\cos 3\theta$ component. The errors are 95 percent confidence levels. The lens position is measured relative to the primary component in B. The position angles are measured north through east.

metric mass density within the images. Therefore, the luminous matter distribution is flatter (more elliptical) than the total matter distribution.

The higher order moments are due only to a mass distribution outside the ring of images. The quadrupole moment largely determines the image geometry, which is further perturbed by the $\cos 3\theta$ moment. The external shear has a position angle of -14°, indicating the mass distribution is located at an angle of 76° or -104°. Annis & Luppino (1993) observed the field around the MG0414 system at infrared wavelengths and found many faint objects within 40″. Objects 5 and 9 (Table 3 from Annis & Luppino 1993) are in the correct orientation to produce the shear, although both objects are $\gtrsim 19''$ away. If we assume the lens redshift is small ($z_L \simeq 0.1$), we can obtain a lower limit on the mass of the galaxies required to produce the shear in the primary lens galaxy,

$$M(r) \approx 10^{12} h_{75}^{-1} \left(\frac{r}{19''}\right)^2 \left(\frac{\mathcal{R}(z_L, z_S, \Omega)}{\mathcal{R}(0.1, 2.64, 1.0)}\right) M_\odot \tag{6.2}$$

where $H_o = 75 h_{75}$ km s^{-1} Mpc^{-1} and $\mathcal{R}(z_L, z_S, \Omega)$ depends on the curvature of the universe (Equation 6.6). The dependence of $M(r)$ on the lens redshift is identical to that in Figure 6-1. For a lens at $z_L = 1$, the required mass becomes very large for an elliptical galaxy ($\approx 10^{13} h_{75}^{-1} M_\odot$ for an object at $r \approx 19''$).

At optical wavelengths, the lens galaxy is too faint to determine if the luminous matter distribution outside the images can cause the observed quadrupole moment.

However, the HST images of the lens galaxy shows the position angle of the ellipticity within the ring of images is not consistent with the measured shear orientation.

The perturbation to the quadrupole moment required to fit the image geometry broke the reflection symmetry in the lens, i.e. $\phi(\vec{r}) = \phi(-\vec{r})$. In particular, we needed to include the next higher order moment from an external mass distribution, $\beta r^3 \cos 3(\theta - \theta_\beta)$. At the critical radius (approximately the distance from the lens to the images), the amplitude of the "odd" moment is a factor of 10 lower than the quadrupole moment ($\frac{1}{2}\gamma \approx 10\beta b$). We have verified that this level of perturbation affects only the details of the four image geometry and does not alter the number of images. The source of the perturbation is consistent with its being object X, the faint object 1″ west of B found by Schechter & Moore (1993). The lens model which fits next best—the two SIS components plus external shear model—has the second SIS component near the position of object X. Schechter & Moore (1993) did not quote an uncertainty on the position, though they did state that their detection was only at the 5σ level. If object X is at a significantly different redshift than the primary lens galaxy, the apparent position of object X does not have to agree with that found by the lens inversion. However, the position angle of the $\cos 3\theta$ component should not vary significantly.

We do not believe the $\cos 3\theta$ perturbation arises purely within the primary lens galaxy. Although optical images of the galaxy do not show any obvious perturbations, a rigorous analysis has not yet been performed (Falco 1995). Optical photometry of elliptical galaxies has found small deviations from a purely elliptical structure (Franx *et al.* 1989; Bender *et al.* 1987). The isophotes of many ellipticals require a $\cos 3\theta$ moment with an amplitude of a few tenths of a percent relative to the major axis. Franx *et al.* (1989) attribute these perturbations either to dust or to true deformations in elliptical galaxies. The magnitude of the $\cos 3\theta$ component scales as r_d^{-3}, where r_d is the characteristic radius of the surface mass density perturbation. The asymmetries are more concentrated at larger radii ($r \gtrsim 12$ kpc), so the observed deformations lead to perturbations below 0.1 percent at the critical radius. Deformations could exist closer to the center of the primary galaxy; however, we find within the circle of images

the lens is best fit without any deformations from spherical symmetry. Deep high-resolution observations of MG0414 can determine the distribution of the luminous matter in the primary lens galaxy. Moreover, if the object X is behind the primary lens, the image of object X should be distorted by the gravitational potential of the primary lens. These observations can place limits on the redshift of object X relative to the primary lens.

Seljak (1994) has shown that large scale structure will perturb the relative positions of the images by a few percent. However, structures on a smaller scale may lead to perturbations larger than he predicted. This fact is clear if we consider that object X is significant. Its proximity and mass cause perturbations at the one percent level.

The 5 GHz VLBI observations of the components in MG0414 show the system to be resolved at the 10 milliarcsecond level. The lens inversion of the 15 GHz VLA observation (100 milliarcsecond resolution) only fit for the positions and magnification of each image. However, the resolved structures provide constraints on the gradient of the magnification matrix at each image. Although we do not have a reliable detection of C, we used the data from A1, A2, and B and found the VLA lens model is consistent with the VLBI data. However, the lack of constraints from component C caused large uncertainties in the best fit lens parameters. We find the inclusion of the VLA position of C in the lens inversion greatly reduces the uncertainties in the results. The inversion results from the VLBI data show the lens model magnification gradients are somewhat consistent with the observed VLBI data. We were limited to the point source inversion algorithm and thus approximated the resolved structures as point sources. The poor quality of our VLBI data set also prevented a more detailed examination of the structure within each component in MG0414. In particular, low surface brightness emission was not detected, causing a significant reduction in the observed flux. These resolved structures are needed to place strong constraints on the lens models. The recent development of the Very Large Baseline Array provides a good instrument for high-resolution and high dynamic range observations.

To take advantage of the resolved structure in the images, the lens inversion should be performed using the Visibility LensClean algorithm on both the VLA and VLBI

data sets. The additional constraints from the extended structures will lead to smaller confidence intervals on the lens model parameters. Furthermore, we only focused on the angular structure of the lens by fixing the radial structure to be isothermal. The extra information used by Visibility LensClean may also be able to constrain the radial structure of the lens galaxy.

6.2 Optical-Radio Flux Ratio Discrepancy

The optical A2/A1 flux ratio of 0.3 (Schechter & Moore 1993) is significantly smaller than the measured radio A2/A1 flux ratio of 0.9 (Katz & Hewitt 1995). Using the best fit lens model, we examine the magnifications at the A1 and A2 components, shown in Table 6.2. We find that the magnifications at the primary and secondary

Component	Primary	Secondary
A1	29	50
A2	17	38
A2/A1	0.6	0.8

Table 6.2: Magnifications at the positions of the primary and secondary components predicted by the best fit $\cos 3\theta$ lens model.

components change rapidly due to their close distance to the critical line. However, the A2/A1 magnification ratios at the primary and secondary components remain relatively constant in the range $0.6 \sim 0.8$. These values are significantly larger than the measured optical flux ratio. If the quasar core is located near either the primary or secondary component, the optical flux ratio cannot be caused by differential magnification. Multifrequency or polarization VLBI observations are required to identify the core component.

Our best fit lens model is identical to the $\beta = 1.0$ model used by Witt, Mao, & Schechter (1994), except for the $\cos 3\theta$ perturbation. We have shown that their lens model parameterization (model 2 in Section 4.1 with zero core radius) does not fit the image geometry seen in radio observations. However, the perturbation is weak

and should not significantly impact their results, which state that the low optical flux ratio of 0.3 is caused by microlensing.

6.3 Nature of the Lens

Using the lens model found by the lens inversion methods, we calculate some basic properties of the galaxy and object X. The redshift of the background quasar source is $z_S = 2.64$ (Lawrence *et al.* 1994). Unfortunately, no spectral features due to the lens have been found (Lawrence 1995). We crudely estimate the redshift of the lens as the most probable lens redshift for our system, $z_L \approx 0.5$ (Schneider *et al.* 1992).

In gravitational lens systems, the total mass of the lens galaxy interior to the critical radius $M(< b)$ is well determined by the image geometry. For the $\cos 3\theta$ model, we find $M(< b)$ is dependent only on the critical radius,

$$M(< b) = \pi \Sigma_c b^2. \tag{6.3}$$

This expression includes only the mass of the primary galaxy and not the mass causing external shear or $\cos 3\theta$ moments. We can express the critical mass density in terms of solar masses per square arcsecond,

$$\Sigma_c = 3.1 \times 10^{11} h_{75}^{-1} \left[\frac{D_{OS} D_{OL}}{\left(\frac{2c}{H_o}\right) D_{LS}} \right] M_\odot \text{arcsec}^{-2} \tag{6.4}$$

$$= 3.1 \times 10^{11} h_{75}^{-1} \mathcal{R}(z_L, z_S, \Omega) M_\odot \text{arcsec}^{-2} \tag{6.5}$$

where,

$$\mathcal{R}(z_L, z_S, \Omega) = \frac{1}{\Omega^2 (1 + z_L)} \left[\frac{(1 - \Omega - G_L)(1 - \Omega - G_S)}{(1 - \Omega - G_L G_S)} \right] \left[\frac{(1 - G_L)(1 - G_S)}{(G_L - G_S)} \right], \tag{6.6}$$

$G_i = \sqrt{1 + \Omega z_i}$, and $H_o = 75 h_{75}$ km s^{-1} Mpc^{-1}. Using Equation 3.11, we find the mass of the primary lens is given by,

$$M(< b) = 4.3 \pm 0.1 \times 10^{12} h_{75}^{-1} \mathcal{R}(z_L, z_S, \Omega) M_\odot. \tag{6.7}$$

If we assume $\Omega = 1$ (Einstein-de Sitter cosmology) and a lens redshift of $z_L = 0.5$, we find the mass enclosed by the critical radius of $5.4h_{75}^{-1}$ kpc is $8.5 \pm 0.1 \times 10^{11}h_{75}^{-1}M_{\odot}$. This value is in the normal range for elliptical galaxies. Figure 6-1 shows the dependence of the lens mass on the lens redshift and Ω for $H_o = 75$ km s^{-1} Mpc^{-1}. We see that for redshifts near the source redshift of $z_S = 2.64$, a large mass is

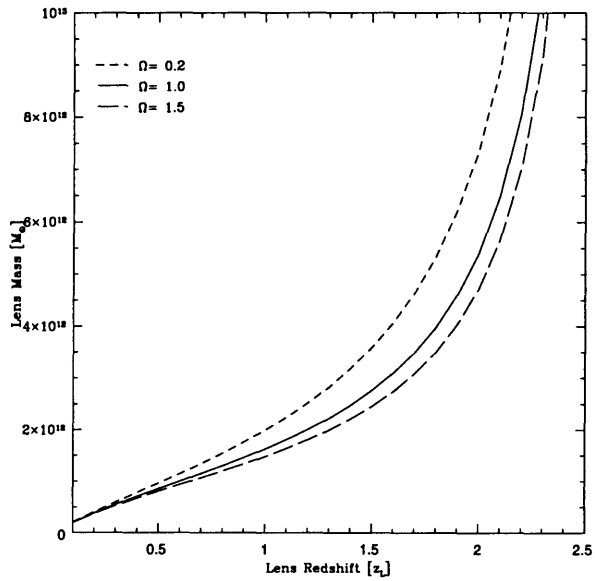

Figure 6-1: Mass of the primary lensing galaxy as a function of lens redshift. We assume a Friedmann cosmology with $\Lambda = 0$ and $H_o = 75$ km s^{-1} Mpc^{-1}. We plot three curves corresponding to $\Omega = 0.2$, 1.0, and 1.5.

required to achieve the observed image separations. At redshifts larger than unity, the curvature of the universe becomes significant.

We can estimate the mass of object X using the two SIS plus external shear lens model. Although this model did not fit as well as the $\cos 3\theta$ model, it gave comparable results. We found a critical radius for object X of 0.076 ± 0.063 arcseconds. We make the simplifying assumption that object X is at the same redshift as the primary galaxy, and find that the mass within the critical radius is,

$$M(< b) = 5.9 \pm 9.6 \times 10^9 h_{75}^{-1}\mathcal{R}(z_L, z_S, \Omega)M_{\odot}. \tag{6.8}$$

The mass has the same dependence on the lens redshift as the mass of the primary

galaxy shown in Figure 6-1. At a redshift of $\Omega = 1$ and $z_L = 0.5$, the mass within $0.4h_{75}^{-1}$ kpc is $1.5 \pm 2.4 \times 10^9 h_{75}^{-1} M_\odot$. This mass is consistent with that of a small companion to the primary lens, although one must remember that there is no direct evidence that these objects are at the same redshift.

The inferred velocity dispersion of dark matter in an isothermal halo is relatively insensitive to the exact cosmological model adopted and depends only on the critical radius of the lens,

$$\sigma_{DM} = \sqrt{\frac{bc^2}{4\pi}\left(\frac{D_{OS}}{D_{LS}}\right)} \tag{6.9}$$

$$= 186\sqrt{\frac{D_{OS}}{D_{LS}}}\left(\frac{b}{1''}\right)^{\frac{1}{2}} \text{km s}^{-1}. \tag{6.10}$$

Since the velocity dispersion depends only the ratio of distances, we see that σ_{DM} does not depend on H_o. The critical radius for the primary lens galaxy is $1''.181 \pm 0''.010$ (Table 6.1), so the inferred dark matter velocity dispersion is given by,

$$\sigma_{DM} = 202 \pm 1\sqrt{(1+z_L)\left[\frac{1-\Omega-G_S}{1-\Omega-G_L G_S}\right]\left[\frac{G_S-1}{G_S-G_L}\right]} \text{km s}^{-1}. \tag{6.11}$$

Figure 6-2 shows σ_{DM} as a function of redshift for several cosmologies and we see that the galaxy velocity dispersion is weakly dependent on the cosmological model. However, the redshift of the lens is important. We find a velocity dispersion of 258 ± 1 km/s for $z_L = 0.5$, with a range from 220 km/s ($z_L \simeq 0.1$) to 1400 km/s ($z_L \simeq 2.5$). Typically, an elliptical galaxy has a velocity dispersion of $\lesssim 400$ km/s, which limits the lens redshift to $z_L \lesssim 1.4$.

The Faber-Jackson (1976) relation connects the total luminosity of an elliptical galaxy with its central velocity dispersion. Gott (1977) showed that the velocity dispersion of dark matter σ_{DM} is related to the luminous velocity dispersion σ_L by $\sigma_{DM} = (3/2)^{1/2}\sigma_L$. However, Kochanek (1994) examined the dispersion profiles of 37 elliptical galaxies and found this relationship is true for the average of luminous velocity dispersion over the entire galaxy, but, near the galaxy center, the luminous velocity dispersion is a good estimator of σ_{DM}. Kochanek (1994) developed a

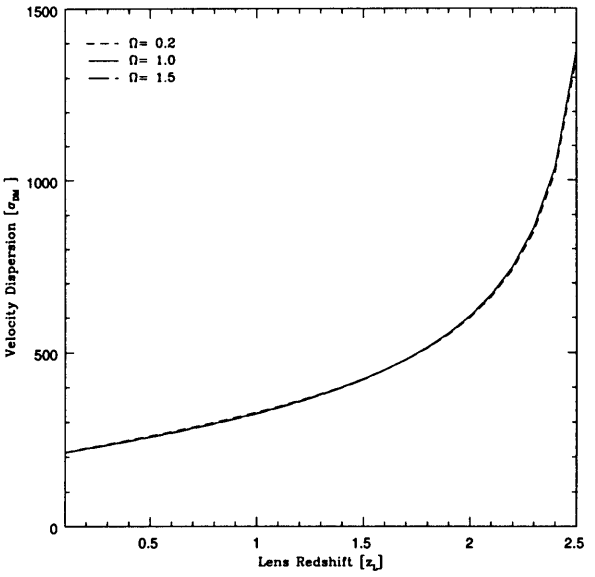

Figure 6-2: Velocity dispersion of the lensing galaxy as a function of lens redshift and Ω. We plotted three values of Ω: 0.2, 1.0, and 1.5.

luminosity-σ_{DM} relationship analogous to the Faber-Jackson relation:

$$L = L_* \left(\frac{\sigma_{DM}}{\sigma_{DM*}}\right)^{\gamma} \tag{6.12}$$

where $\sigma_{DM*} = 225 \pm 10$ km/s and $\gamma = 4.1 \pm 0.9$ (Kochanek 1994). In the visual band, $M_{V*} = -2.5 \log_{10} L_* + \text{constant} \approx -21.5$ (Milhalas & Binney 1981). Therefore, we can estimate the apparent magnitude[1] of the lens galaxy using,

$$m_V = M_{V*} + 5 \log_{10} \left(\frac{D_{OL}(1+z_L)^2}{10 \text{ pc}}\right) - \frac{5\gamma}{2} \log_{10} \left(\frac{\sigma_{DM}}{\sigma_{DM*}}\right). \tag{6.13}$$

[1]The apparent magnitude m is measure of the flux from an object on a logarithmic scale and given by $m = -2.5 \log_{10} F + c$ where F is the observed flux. Note that the definition is such that a larger apparent magnitude corresponds to a fainter object. The absolute magnitude M is defined as the apparent magnitude of an object at a distance of 10 parsecs. Therefore, the apparent and absolute magnitudes are related by,

$$m - M = 5 \log_{10} \left(\frac{d_L}{10 \text{ pc}}\right)$$

where the left-hand side of the equation is known as the "distance modulus" and the luminosity distance d_L is related to the angular-diameter distance d_A by $d_L = (1+z)^{-2} d_A$.

Figure 6-3 shows the dependence of the apparent magnitude as a function of redshift and cosmology. For the redshift range from $z_L = 0.1$ to $z_L = 2.5$, we find a peak magnitude of $\simeq 20$. Angonin-Willaime *et al.* (1994) have measured 24.4 ± 0.5 for the magnitude in the V-band of the lens galaxy; this result is plotted in Figure 6-3. We applied an evolution correction (Tinsley 1972) and the K-correction (Coleman *et al.* 1980) for elliptical galaxies to extrapolate the measured apparent magnitude to a given lens redshift. We only plot the measured magnitude up to $z = 2.0$, since the correction have been calculated only in this range. The corrections are made assuming elliptical galaxies have spectra which are similar to the nuclei of M31 and M81. These corrections are in agreement with Oke & Sandage (1968) and Pence (1976) up to a redshift of $\simeq 1.3$. However, at larger redshifts, the nuclei of M31 and M81 may be not approximate an elliptical galaxy and the corrections may be invalid. For a lens redshift below $z \sim 1$, we find a discrepancy of $\gtrsim 1$ magnitude, supporting the theory that dust is present in the lens galaxy (Lawrence *et al.* 1994).

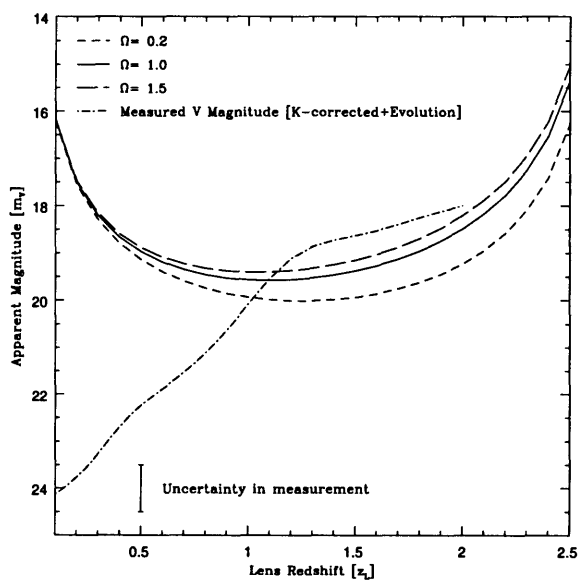

Figure 6-3: Apparent magnitude of the lensing galaxy as a function of lens redshift and Ω using the Faber-Jackson relation which assumes the lens galaxy is a normal elliptical galaxy. We have assumed $H_o = 75$ km s^{-1} Mpc^{-1} and plotted curves three values of Ω: 0.2, 1.0, and 1.5.

If the difference in the radio and optical flux ratios are due to microlensing (Witt

et al. 1994), the galaxy may not be very dusty at the image locations. If we assume the entire galaxy is then not very dusty, we find the lens should be at a redshift greater than unity. At these redshifts, the inferred mass and velocity dispersion of the galaxy are $\gtrsim 1.5 \times 10^{12} h_{75}^{-1} M_{\odot}$ and $\gtrsim 330$ km/s, respectively.

6.4 Prospects for Determining H_o

An exciting application of gravitational lens system is the determination of Hubble's constant. Moore & Hewitt (1995) find the radio fluxes are variable at the level of a few percent and are pursuing the time delay measurements in this system.

To solve for H_o as a function of the measured time delay, we invert equation 3.20 to obtain,

$$\begin{aligned} H_o &= 2\left(\frac{1+z_L}{\triangle t_{12}}\right)\mathcal{R}(z_L, z_S, \Omega) \\ &\quad \times \left\{\frac{1}{2}\left[\left(\vec{\theta}_1 - \vec{\beta}_1\right)^2 - \left(\vec{\theta}_2 - \vec{\beta}_2\right)^2\right] - \left[\phi\left(\vec{\theta}_1\right) - \phi\left(\vec{\theta}_2\right)\right]\right\} \qquad (6.14) \\ &= 2\left(\frac{1+z_L}{\triangle t_{12}}\right)\mathcal{R}(z_L, z_S, \Omega)\left\{\frac{1}{2}\left[\vec{\alpha}_1^2 - \vec{\alpha}_2^2\right] - \left[\phi\left(\vec{\theta}_1\right) - \phi\left(\vec{\theta}_2\right)\right]\right\} \qquad (6.15) \end{aligned}$$

where $\mathcal{R}(z_L, z_S, \Omega)$ is defined in Equation 6.6. We know that the images must map to the same source and, therefore, the lens equation gives,

$$\vec{\alpha}_1 - \vec{\alpha}_2 = -\left(\vec{\theta}_1 - \vec{\theta}_2\right). \qquad (6.16)$$

Using this relationship, we transform Equation 6.15 to,

$$H_o = 2\left(\frac{1+z_L}{\triangle t_{12}}\right)\mathcal{R}(z_L, z_S, \Omega)\left\{-\left(\vec{\theta}_1 - \vec{\theta}_2\right)\cdot\left(\frac{\vec{\alpha}_1 + \vec{\alpha}_2}{2}\right) - \left[\phi\left(\vec{\theta}_1\right) - \phi\left(\vec{\theta}_2\right)\right]\right\} \qquad (6.17)$$

(Gorenstein *et al.* 1988b). This formulation requires the images 1 and 2 to map back to the same source. Therefore, more observational constraints are imposed in the calculation of H_o, reducing the uncertainties in the lens model from correlations in the lens parameters.

In Figure 6-4, we plot H_o for a variety of lens model in an Einstein-de Sitter cosmology ($\Omega = 1$, $\Lambda = 0$). Since the time delays in MG0414 have not been measured,

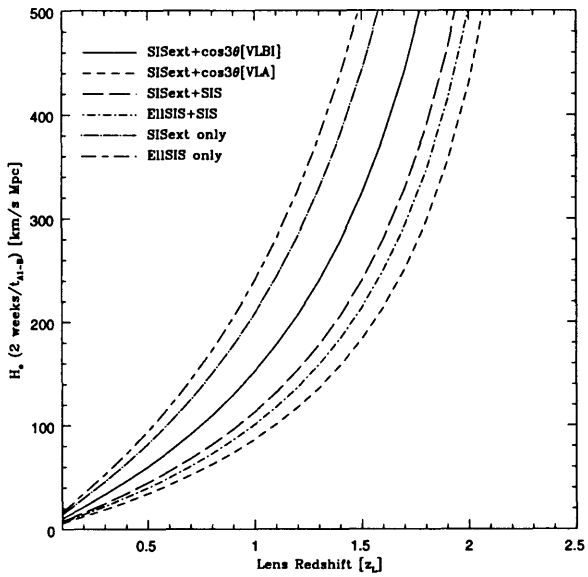

Figure 6-4: Hubble constant for different lens models. We have assumed a time delay of 2 weeks between A1 and B. We have assume $\Omega = 1$ and $\Lambda = 0$.

we assumed the A1-B time delay is two weeks; different delays simply scale the curve vertically in the sense that a larger delay corresponds to a smaller Hubble constant. At a lens redshift of $z_L = 0.5$ and for $\Omega = 1$, the best fit $\cos 3\theta$ lens model predicts a Hubble's constant of,

$$H_o = 60 \pm 8 \left(\frac{\triangle t_{B-A1}}{2 \text{ weeks}} \right)^{-1} \text{ km s}^{-1} \text{ Mpc}^{-1} \tag{6.18}$$

where the quoted uncertainty is the 95 percent confidence level from propagating the lens model uncertainties through Equation 6.17. The different models show similar dependences on the lens redshift, although significantly different values of H_o at a given lens redshift. The $\cos 3\theta$ model and the two SIS plus external shear models (SISext+SIS in Figure 6-4) are the models which fit the system the best. The other models perform significantly worse in the lens inversion. We see that the differences between the best fit model using the VLA data and the VLBI data are larger than

the uncertainty estimates, indicating that an accurate lens inversion is crucial to a reliable determination of H_o.

We plot H_o predicted by the best fit lens model in several different cosmological models, including those with a non-zero cosmological constant Λ. We vary Ω from 0.2 to 1.5 in a cosmology with $\Lambda = 0$. We also plot three models with no curvature, but with different values of Ω and Λ. The cosmological models with curvature ($\Lambda = 0$

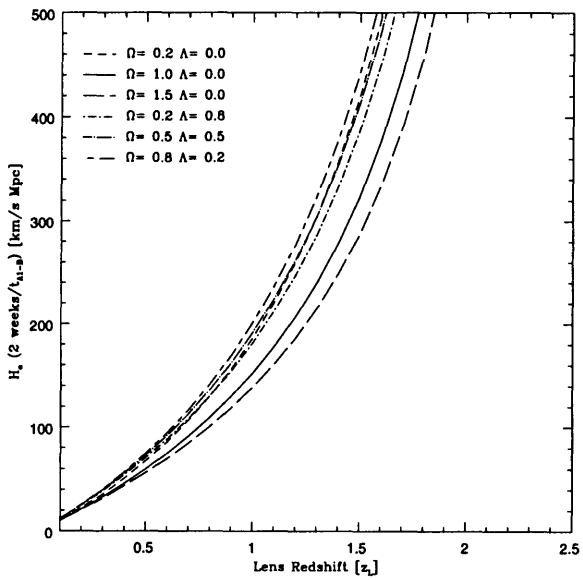

Figure 6-5: Hubble constant for different cosmologies and best fit lens model. We have assumed a time delay of 2 weeks between A1 and B.

and $\Omega = 0.2$ and 1.5) are significantly different from the $\Omega = 1$ cosmology. The flat cosmologies with differing amounts of Λ show differences within the lens model uncertainties. If H_o is found independently, this system may also be used to place limits on curvature of the universe.

6.5 Future Prospects

The point source lens inversion methods have shown that the $\cos 3\theta$ models fit the 15 GHz VLA data. However, the analysis should be implemented with LensClean to reduce the uncertainties in the lens model parameters. The largest gain in the

lens modeling will be achieved by applying the Visibility LensClean algorithm to the VLBI data. While we have shown that the lens model does also fit the magnification gradients at the image positions, the errors were large due to the resolved structures in the VLBI images. VLBA observations with higher dynamic range should detect the low-level extended emission and provide more information about the magnification structure at each component. In addition, performing the lens inversion within Visibility LensClean should provide stringent constraints on the lens model and significantly reduce the uncertainties and range of possible lens models. Therefore, one can explore the finer details in the lens, such as the radial structure, and address the questions of whether a lens redshift lens model is sufficient to describe the system and whether the more terms should be included in the multipole expansion of the lens.

The best fit lens model indicate a perturbation in the gravitational potential in the direction of object X. Object X could be a small companion to the primary lens or simply another galaxy near the line-of-sight. Deep optical observations may determine if object X is truly extragalactic. If object X is behind the primary galaxy, deep images should detect distortions in the shape of the galaxy due to gravitational lensing by the primary galaxy.

The astrophysics results to be extracted from the MG0414 system rely on knowing the redshift of the lens. Lawrence *et al.* (1994) found the lens in MG0414 to be rich in dust. If the lens contains large amounts of neutral hydrogen, the redshift of the lens should be detectable through absorption at the $\lambda 21$ cm HI line. When the redshift of the lens is known and better constrained models are obtained, this system will be an excellent candidate for determining Hubble's constant and possibly Ω.

Appendix A

Lens Models

This section describes the deflection angles, magnifications, and surface mass densities for the lens models used in this thesis. The coordinates are relative to the lens center. The rectangular coordinates have their usual definitions: $(x, y) = (r\cos\theta, r\sin\theta)$.

A.1 Singular Isothermal Sphere (SIS) plus External Shear

Observations of the rotation curves in spiral galaxies show that to radii much greater than the optical emission extends, the mass increases linearly with radius (i.e. the two dimensional mass density falls off as r^{-1}). The singular isothermal sphere (SIS) has a mass distribution which obeys this radial dependence, assuming spherical symmetry. The quadrupole moment in this lens model arises from an external shear field. We parameterize this model by,

$$\phi(\vec{r}) = br + \frac{1}{2}\gamma r^2 \cos 2(\theta - \theta_\gamma) \tag{A.1}$$

where b is the critical radius of the lens. This model approximates the gravitational influence from an external mass distribution by the lowest order effect, the external shear field, which causes a quadrupole moment parameterized by the shear strength γ and the shear position angle θ_γ. The surface mass density of the lens (not including

the external mass distribution) is given by,

$$\Sigma(\vec{r}) = \frac{\Sigma_c}{2}\frac{b}{r} \tag{A.2}$$

where $\Sigma_c = c^2 D_{OS} D_{OL}/4\pi G D_{LS}$ is the critical surface mass density for lensing. To simplify the computation, we define the cosine and sine shear coefficients,

$$\begin{aligned} \gamma_c &= \gamma \cos 2\theta_\gamma \\ \gamma_s &= \gamma \sin 2\theta_\gamma \end{aligned} \tag{A.3}$$

so the potential can be written as,

$$\phi(\vec{r}) = br + \frac{1}{2}(x^2 - y^2)\gamma_c + xy\gamma_s. \tag{A.4}$$

The deflection produced in the x and y directions are,

$$\begin{aligned} \alpha_x &= \tfrac{bx}{r} + x\gamma_c + y\gamma_s \\ \alpha_y &= \tfrac{by}{r} - y\gamma_c + x\gamma_s \end{aligned} \tag{A.5}$$

and the magnification is,

$$\mu = \left| \begin{array}{cc} 1 - \frac{by^2}{r^3} - \gamma_c & -\frac{bxy}{r^3} - \gamma_s \\ -\frac{bxy}{r^3} - \gamma_s & 1 - \frac{bx^2}{r^3} + \gamma_c \end{array} \right|^{-1}. \tag{A.6}$$

A.2 Generalized Monopole plus External Shear

This lens model generalizes the SIS plus external shear model by adding two parameters which control the radial dependence of the monopole structure:

$$\phi(\vec{r}) = \left\{ \begin{array}{ll} \frac{b^{2-\alpha}}{\alpha}(r^2 + s^2)^{\alpha/2} & \alpha \neq 0 \\ \frac{b^2}{2}\ln(r^2 + s^2) & \alpha = 0 \end{array} \right\} + \frac{1}{2}\gamma r^2 \cos 2(\theta - \theta_\gamma). \tag{A.7}$$

The monopole exponent α determines the concentration of mass within a given radius, in the sense that a lower value of α corresponds to a more compact mass distribution.

The exponent can vary from $\alpha = 0$ to $\alpha = 2$, where $\alpha = 0$ is a Plummer distribution (Binney & Tremaine 1987), $\alpha = 1$ is an isothermal distribution, and $\alpha = 2$ is a sheet of uniform mass density. Using Equation 3.10, the surface mass density is given by,

$$\Sigma(\vec{r}) = \frac{\Sigma_c}{2} b^{2-\alpha}(r^2 + s^2)^{\alpha/2-2}(s^2 + \alpha r^2). \tag{A.8}$$

The deflection produced by this model is,

$$\begin{aligned} \alpha_x &= b^{2-\alpha}\tfrac{x}{r}(r^2 + s^2)^{\alpha/2-1} + x\gamma_c + y\gamma_s \\ \alpha_y &= b^{2-\alpha}\tfrac{y}{r}(r^2 + s^2)^{\alpha/2-1} - y\gamma_c + x\gamma_s \end{aligned} \tag{A.9}$$

where γ_c and γ_s are given by Equation A.3. The magnification of an image is given by,

$$\mu = \begin{vmatrix} 1 - \mathcal{A}(r)\left[r^2 + s^2 + x^2(\alpha - 2)\right] - \gamma_c & \mathcal{A}(r)xy(\alpha - 2) - \gamma_s \\ \mathcal{A}(r)xy(\alpha - 2) - \gamma_s & 1 - \mathcal{A}(r)\left[r^2 + s^2 + y^2(\alpha - 2)\right] + \gamma_c \end{vmatrix}^{-1} \tag{A.10}$$

where,

$$\mathcal{A}(r) = b^{2-\alpha}(r^2 + s^2)^{\alpha/2-2}. \tag{A.11}$$

The effect of the core radius is to prevent the mass density from diverging at the lens center. The magnification of the "odd" image (see section 3.1) is strongly dependent on the size of the core radius. Since the "odd" image is located near the lens center, we can approximate its magnification by,

$$\mu_{odd} \simeq \left(\frac{s}{b}\right)^{4-2\alpha} \tag{A.12}$$

which, for $\alpha < 2$, decreases to zero as the core radius tends towards zero.

A.3 Approximate Singular Isothermal Ellipsoid

The elliptical mass distribution results in a quadrupole moment different from the SIS plus external shear lens model. We parameterize the elliptical mass distribution by,

$$\Sigma(\vec{r}) = \frac{\Sigma_c}{2}\frac{b}{r(1-\epsilon^m\cos 2(\theta-\theta_\epsilon))} \tag{A.13}$$

where ϵ^m is the ellipticity of the mass distribution. We expand the mass density in a multipole expansion and only include the monopole and quadrupole moments,

$$\Sigma(\vec{r}) = \frac{\Sigma_c}{2}\frac{b}{r}(1+\epsilon^m\cos 2(\theta-\theta_\epsilon)). \tag{A.14}$$

The potential formed by this mass distribution is,

$$\phi(\vec{r}) = br + \epsilon br\cos 2(\theta-\theta_\epsilon). \tag{A.15}$$

We see that the ellipticity of the potential ϵ is only one third that of the mass distribution: $\epsilon = \frac{1}{3}\epsilon^m$. We define the quadrupole shear coefficients,

$$\begin{aligned}\epsilon_c &= \epsilon b\cos 2\theta_\epsilon \\ \epsilon_s &= \epsilon b\sin 2\theta_\epsilon\end{aligned} \tag{A.16}$$

so the potential can be written as,

$$\phi(\vec{r}) = br + \frac{x^2-y^2}{r}\epsilon_c + \frac{2xy}{r}\epsilon_s. \tag{A.17}$$

The deflection produced by this lens model is,

$$\begin{aligned}\alpha_x &= \tfrac{bx}{r} + \tfrac{x}{r^3}(3x^2+y^2)\epsilon_c + \tfrac{2y^3}{r^3}\epsilon_s \\ \alpha_y &= \tfrac{by}{r} - \tfrac{y}{r^3}(3y^2+x^2)\epsilon_c + \tfrac{2x^3}{r^3}\epsilon_s\end{aligned} \tag{A.18}$$

and the magnification is,

$$\mu = \left| \begin{array}{cc} 1 - \frac{by^2}{r^3} + \frac{3y^2}{r^3}(\rho_c\epsilon_c + \rho_s\epsilon_s) & -\frac{bxy}{r^3} - \frac{3xy}{r^3}(\rho_c\epsilon_c + \rho_s\epsilon_s) \\ -\frac{bxy}{r^3} - \frac{3xy}{r^3}(\rho_c\epsilon_c + \rho_s\epsilon_s) & 1 - \frac{bx^2}{r^3} + \frac{3x^2}{r^3}(\rho_c\epsilon_c + \rho_s\epsilon_s) \end{array} \right|^{-1} \tag{A.19}$$

where,

$$\begin{aligned} \rho_c &= \frac{x^2-y^2}{r^2} = \cos 2\theta \\ \rho_s &= \frac{2xy}{r^2} = \sin 2\theta. \end{aligned} \tag{A.20}$$

A.4 De Vaucouleurs Mass Distribution plus External Shear

De Vaucouleurs (1948) found the light distributions of elliptical galaxies are described by,

$$I(\xi) = I_e e^{-7.67[\xi^{0.25}-1]} \tag{A.21}$$

where $\xi = r/R_e$ is the radius in units of the effective radius R_e. The effective radius is defined such that half the total luminosity is contained within a circle of radius R_e. I_e is the surface brightness at the effective radius R_e. This lens model assumes a constant mass-to-light ratio and, therefore, has a mass distribution with the same radial dependence as $I(\xi)$. To add ellipticity to the lens, an external shear field is included. The deflection produced by this lens is,

$$\begin{aligned} \alpha_x &= b\frac{R_e}{r}\frac{x}{r}F(\xi) + x\gamma_c + y\gamma_s \\ \alpha_y &= b\frac{R_e}{r}\frac{y}{r}F(\xi) - y\gamma_c + x\gamma_s \end{aligned} \tag{A.22}$$

where b is the critical radius, γ_c and γ_s are given by Equation A.3, and $F(\xi)$ is,

$$F(\xi) = \frac{\int_o^\xi xI(x)dx}{\int_0^1 xI(x)dx} \quad 0 \le F \le 2 \tag{A.23}$$

(Maoz & Rix 1993). The magnification of an image is,

$$\mu = \left| \begin{array}{cc} 1 - bR_e \left[\frac{y^2-x^2}{r^4} F(\xi) + \frac{x^2}{r^4}\xi K(\xi)\right] - \gamma_c & bR_e \frac{xy}{r^4}\left[2F(\xi) + \xi K(\xi)\right] - \gamma_s \\ bR_e \frac{xy}{r^4}\left[2F(\xi) + \xi K(\xi)\right] - \gamma_s & 1 - bR_e \left[\frac{x^2-y^2}{r^4} F(\xi) + \frac{y^2}{r^4}\xi K(\xi)\right] + \gamma_c \end{array} \right|^{-1} \tag{A.24}$$

where,

$$K(\xi) = \frac{\xi I(\xi)}{\int_0^1 x I(x) dx}. \tag{A.25}$$

A.5 Approximate Elliptical Mass Distribution

The elliptical mass distribution is given by,

$$\Sigma(\vec{r}) = \frac{\Sigma_c}{2} b^{2-\alpha} \left[r^2(1 + \epsilon \cos 2(\theta - \theta_\epsilon)) + s^2\right]^{\alpha/2-1}. \tag{A.26}$$

We expand $\Sigma(\vec{r})$ in a multipole expansion to quadrupole order,

$$\Sigma(\vec{r}) = \frac{\Sigma_c}{2} b^{2-\alpha} (r^2 + s^2)^{\alpha/2-1} \left[1 - \left(\frac{r^2}{r^2 + s^2}\right)\left(\frac{2-\alpha}{2}\right) \epsilon \cos 2(\theta - \theta_\epsilon)\right]. \tag{A.27}$$

We define the cosine and sine shear coefficients,

$$\begin{aligned} \gamma_c &= \epsilon \cos 2\theta_\epsilon \\ \gamma_s &= \epsilon \sin 2\theta_\epsilon \end{aligned} \tag{A.28}$$

so the surface mass density can be written as,

$$\Sigma(\vec{r}) = \frac{\Sigma_c}{2} b^{2-\alpha} (r^2 + s^2)^{\alpha/2-1} \left[1 - \left(\frac{1}{r^2 + s^2}\right)\left(\frac{2-\alpha}{2}\right)\left\{(x^2 - y^2)\gamma_c + 2xy\gamma_s\right\}\right]. \tag{A.29}$$

The deflection produced by this model is,

$$\begin{aligned} \alpha_x &= b^{2-\alpha}\left[\frac{x}{r}\frac{\partial \phi_{MP}}{\partial r} + \frac{x}{r}\frac{\partial \phi_{QP}}{\partial r}(\gamma_c\rho_c + \gamma_s\rho_s) + \frac{2y}{r^2}\phi_{QP}(\gamma_c\rho_s - \gamma_s\rho_c)\right] \\ \alpha_y &= b^{2-\alpha}\left[\frac{y}{r}\frac{\partial \phi_{MP}}{\partial r} + \frac{y}{r}\frac{\partial \phi_{QP}}{\partial r}(\gamma_c\rho_c + \gamma_s\rho_s) - \frac{2x}{r^2}\phi_{QP}(\gamma_c\rho_s - \gamma_s\rho_c)\right] \end{aligned} \tag{A.30}$$

where,

$$\begin{aligned} \rho_c &= \frac{x^2-y^2}{r^2} = \cos 2\theta \\ \rho_s &= \frac{2xy}{r^2} = \sin 2\theta \end{aligned} \tag{A.31}$$

and,

$$\frac{\partial \phi_{MP}}{\partial r} = \frac{(r^2+s^2)^{\alpha/2} - s^\alpha}{\alpha r} \tag{A.32}$$

$$\phi_{QP} = \frac{1}{2}\frac{\alpha r^2 (r^2+s^2)^{\alpha/2} - 2s^2\left[(r^2+s^2)^{\alpha/2} - s^\alpha\right]}{\alpha(\alpha+2)r^2} \tag{A.33}$$

$$\frac{\partial \phi_{QP}}{\partial r} = \frac{r}{2}(r^2+s^2)^{\alpha/2-1} - \frac{2}{r}\phi_{QP}. \tag{A.34}$$

Using Equation 3.15, we see that the magnification matrix can be written as,

$$\mu = \begin{pmatrix} 1-\partial_{xx}\phi & -\partial_{xy}\phi \\ -\partial_{xy}\phi & 1-\partial_{yy}\phi \end{pmatrix} \tag{A.35}$$

where,

$$\begin{aligned} \partial_{xx}\phi \equiv \frac{\partial^2\phi}{\partial x^2} = b^{2-\alpha}\Bigg\{ & \frac{x^2}{r^2}\left[(r^2+s^2)^{\alpha/2-1} - \frac{1}{r}\frac{\partial \phi_{MP}}{\partial r}\right] + \frac{y^2}{r^2}\frac{1}{r}\frac{\partial \phi_{MP}}{\partial r} + \\ & \gamma_c\left[\frac{x^2}{r^2}\rho_c g - \rho_c^2 g_1 + 2\rho_s^2 g_2\right] + \\ & \gamma_s\left[\frac{x^2}{r^2}\rho_s g - \rho_c\rho_s g_1 - 2\rho_c\rho_s g_2\right]\Bigg\} \end{aligned} \tag{A.36}$$

$$\begin{aligned} \partial_{yy}\phi \equiv \frac{\partial^2\phi}{\partial y^2} = b^{2-\alpha}\Bigg\{ & \frac{y^2}{r^2}\left[(r^2+s^2)^{\alpha/2-1} - \frac{1}{r}\frac{\partial \phi_{MP}}{\partial r}\right] + \frac{x^2}{r^2}\frac{1}{r}\frac{\partial \phi_{MP}}{\partial r} + \\ & \gamma_c\left[\frac{y^2}{r^2}\rho_c g + \rho_c^2 g_1 - 2\rho_s^2 g_2\right] + \\ & \gamma_s\left[\frac{y^2}{r^2}\rho_s g + \rho_c\rho_s g_1 + 2\rho_c\rho_s g_2\right]\Bigg\} \end{aligned} \tag{A.37}$$

$$\begin{aligned} \partial_{xy}\phi \equiv \frac{\partial^2\phi}{\partial x \partial y} = b^{2-\alpha}\Bigg\{ & \frac{xy}{r^2}\left[(r^2+s^2)^{\alpha/2-1} - \frac{2}{r}\frac{\partial \phi_{MP}}{\partial r}\right] + \\ & \gamma_c\left[\frac{xy}{r^2}\rho_c g - \rho_c\rho_s g_1 - 2\rho_c\rho_s g_2\right] + \\ & \gamma_s\left[\frac{xy}{r^2}\rho_s g + \rho_s^2 g_1 + 2\rho_c^2 g_2\right]\Bigg\} \end{aligned} \tag{A.38}$$

(A.39)

and,

$$g = \frac{\alpha-2}{2} r^2 (r^2+s^2)^{\alpha/2-2} \tag{A.40}$$

$$g_1 = \frac{1}{2}(r^2+s^2)^{\alpha/2-1} - \frac{6}{r^2}\phi_{QP} \tag{A.41}$$

$$g_2 = \frac{1}{2}(r^2+s^2)^{\alpha/2-1} - \frac{3}{r^2}\phi_{QP}. \tag{A.42}$$

A.6 SIS plus External Shear and Cosine 3θ Component

This lens model contains the SIS plus external shear model and includes a cosine 3θ component,

$$\phi(\vec{r}) = br + \frac{1}{2}\gamma r^2 \cos 2(\theta - \theta_\gamma) + \beta r^3 \cos 3(\theta - \theta_\beta). \tag{A.43}$$

The cosine 3θ component is the next higher moment caused by a mass distribution external to the system and does not add to the surface mass density of the primary lens. Hence, the mass density for this model is also given by Equation A.2. As with the SIS plus external shear model, we use the definitions for the cosine and sine shear coefficients (Equation A.3) and define two coefficients for the $\cos 3\theta$ component,

$$\begin{aligned} \beta_c &= \beta \cos 3\theta_\beta \\ \beta_s &= \beta \sin 3\theta_\beta. \end{aligned} \tag{A.44}$$

The potential can now be written as,

$$\phi(\vec{r}) = br + \frac{1}{2}\tilde{\rho}_c\gamma_c + \frac{1}{2}\tilde{\rho}_s\gamma_s + 3\tilde{\rho}_c(x\beta_c + y\beta_s) - 3\tilde{\rho}_s(y\beta_c - x\beta_s) \tag{A.45}$$

where,

$$\begin{aligned} \tilde{\rho}_c &= x^2 - y^2 &&= r^2\cos 2\theta \\ \tilde{\rho}_s &= 2xy &&= r^2 \sin 2\theta. \end{aligned} \tag{A.46}$$

The deflection produced by this lens model is,

$$\begin{aligned} \alpha_x &= \tfrac{bx}{r} + x\gamma_c + y\gamma_s + 3\tilde{\rho}_c\beta_c + 3\tilde{\rho}_s\beta_s \\ \alpha_y &= \tfrac{by}{r} - y\gamma_c + x\gamma_s + 3\tilde{\rho}_c\beta_c - 3\tilde{\rho}_s\beta_s \end{aligned} \tag{A.47}$$

and the magnification is,

$$\mu = \left| \begin{array}{cc} 1 - \frac{by^2}{r^3} - \gamma_c - 6x\beta_c - 6y\beta_s & -\frac{bxy}{r^3} - \gamma_s - 6x\beta_c + 6y\beta_s \\ -\frac{bxy}{r^3} - \gamma_s - 6x\beta_c + 6y\beta_s & 1 - \frac{bx^2}{r^3} + \gamma_c + 6x\beta_c + 6y\beta_s \end{array} \right|^{-1} . \tag{A.48}$$

A.7 SIS plus External Shear and Octupole

This lens model contains the SIS plus external shear model and includes the octupole moment,

$$\phi(\vec{r}) = br + \frac{1}{2}\gamma r^2 \cos 2(\theta - \theta_\gamma) + \delta r^4 \cos 4(\theta - \theta_\delta) . \tag{A.49}$$

Since the quadrupole and octupole terms are due to an external mass distribution, the mass density is given by Equation A.2. As with the SIS plus external model, we use the definitions for the cosine and sine shear coefficients (Equation A.3) and define two coefficients for the octupole moment,

$$\begin{aligned} \delta_c &= \delta \cos 4\theta_\delta \\ \delta_s &= \delta \sin 4\theta_\delta . \end{aligned} \tag{A.50}$$

The potential can now be written as,

$$\phi(\vec{r}) = br + \frac{1}{2}\tilde{\rho}_c\gamma_c + \frac{1}{2}\tilde{\rho}_s\gamma_s + \tilde{\rho}_c(\tilde{\rho}_c\delta_c + 2\tilde{\rho}_s\delta_s) - \tilde{\rho}_s^2\delta_c \tag{A.51}$$

where $\tilde{\rho}_c$ and $\tilde{\rho}_s$ are defined by Equation A.46. The deflection produced by this lens model is,

$$\begin{aligned} \alpha_x &= \tfrac{bx}{r} + x\gamma_c + y\gamma_s + 4\tilde{\rho}_c(x\delta_c + y\delta_s) + 4\tilde{\rho}_s(x\delta_s - y\delta_c) \\ \alpha_y &= \tfrac{by}{r} - y\gamma_c + x\gamma_s + 4\tilde{\rho}_c(x\delta_s - y\delta_c) - 4\tilde{\rho}_s(x\delta_c + y\delta_s) \end{aligned} \tag{A.52}$$

and the magnification is,

$$\mu = \left| \begin{array}{cc} 1 - \frac{by^2}{r^3} - \gamma_c - 12\tilde{\rho}_c\delta_c - 12\tilde{\rho}_s\delta_s & -\frac{bxy}{r^3} - \gamma_s - 12\tilde{\rho}_c\delta_s + 12\tilde{\rho}_s\delta_c \\ -\frac{bxy}{r^3} - \gamma_s - 12\tilde{\rho}_c\delta_s + 12\tilde{\rho}_s\delta_c & 1 - \frac{bx^2}{r^3} + \gamma_c + 12\tilde{\rho}_c\delta_c + 12\tilde{\rho}_s\delta_s \end{array} \right|^{-1} . \quad \text{(A.53)}$$

Bibliography

Angonin-Willaime, M.-C., Vanderriest, C., Hammer, F., & Magain, P., 1994, *Astronomy & Astrophysics,* **281**, 388

Annis, J. & Luppino, G. A., 1993, *Astrophysical Journal Letters,* **407**, L69

Arfken, G., 1985, *Mathematical Methods for Physicists*, Academic Press, San Diego, CA

Bender, R., Döberneiner, S., & Möllenhoff, C., 1987, *Astronomy & Astrophysics Supplement,* **74**, 385

Binney, J. & Tremaine, S., 1987, *Galactic Dynamics*, Princeton University Press, Princeton, NJ

Blandford, R., 1990, in R. Blandford, H. Netzer, & L. Wolfjer (eds.), *Active Galactic Nuclei*, p. 258, Springer-Verlag

Blandford, R. & Narayan, R., 1992, *Annual Reviews of Astronomy and Astrophysics,* **30**, 311

Blandford, R. D. & Kochanek, C. S., 1987, *Astrophysical Journal,* **321**, 628

Bridle, A. H. & Schwab, F. R., 1989, in R. A. Perley, F. R. Schwab, & A. H. Bridle (eds.), *Sythesis Imaging in Radio Astronomy*, No. 6 in Conference Series, pp 247–258, Astronomical Society of the Pacific

Briggs, D. S., 1994, *Ph.D. thesis*, New Mexico Institute of Mining and Technology

Briggs, D. S., Davis, R., Conway, J., & Walker, R., 1994, *NRAO Memorandum Number 697*

Chen, G., Kochanek, C., & Hewitt, J., 1995, Astrophysical Journal, in press

Chowlson, O., 1924, *Astronomische Nachrichten,* **221**, 329

Churchill, R. V. & Brown, J. W., 1976, *Complex Variables and Applications*, McGraw-

Hill, Inc., New York, NY

Clark, B. G., 1980, *Astronomy & Astrophysics,* **89**, 377

Coleman, G. D., Wu, C.-C., & Weedman, D. W., 1980, *Astrophysical Journal Supplement,* **43**, 393

Conner, S., Lehár, J., & Burke, B., 1992, *Astrophysical Journal Letters,* **387**, L61

Cornwell, T. & Fomalont, E. B., 1989, in R. A. Perley, F. R. Schwab, & A. H. Bridle (eds.), *Sythesis Imaging in Radio Astronomy*, No. 6 in Conference Series, pp 185–197, Astronomical Society of the Pacific

Cotton, W. D. & Schwab, F. R., 1993, *VLBA Scientific Memorandum Number 2*

Crane, P. C. & Napier, P. J., 1989, in R. A. Perley, F. R. Schwab, & A. H. Bridle (eds.), *Sythesis Imaging in Radio Astronomy*, No. 6 in Conference Series, pp 139–165, Astronomical Society of the Pacific

de Vaucouleurs, G., 1948, *Ann. D'Ap.,* **11**, 247

Dyer, C. & Roeder, R., 1973, *Astrophysical Journal Letters,* **180**, L31

Dyson, F. W., Eddington, A. S., & Davidson, C., 1920, *Phil. Trans.,* **A 220**, 291

Eddington, A., 1920, *Space, Time, and Gravitation*, Cambridge University Press, Cambridge

Eddington, A. S., 1919, *Observatory,* **42**, 119

Einstein, A., 1936, *Science,* **84**, 406

Eintein, A., 1915, *Sitzungber Preub. Akad. Wissensch., erster Halbband,* p. 831

Faber, S. M. & Jackson, R. E., 1976, *Astrophysical Journal,* **204**, 668

Falco, E. E., 1995, *Private communication*

Falco, E. E., Gorenstein, M. V., & Shapiro, I. I., 1991, *Astrophysical Journal,* **372**, 364

Franx, M., Illingworth, G., & Heckman, T., 1989, *Astronomical Journal,* **98**, 539

Garrett, M., Calder, R., Porcas, R., King, L., Walsh, D., & Wilkinson, P., 1995, *Monthly Notices of the Royal Astronomical Society,* **270**, 457

Gorenstein, M., Cohen, N., Shapiro, I., Rogers, A., Bonometti, R., Falco, E., Bartel, N., & Marcaide, J., 1988a, *Astrophysical Journal,* **334**, 42

Gorenstein, M. V., Falco, E. E., & Shapiro, I. I., 1988b, *Astrophysical Journal,* **327**,

693

Gott, J. R., 1977, *Annual Reviews of Astronomy and Astrophysics,* **15**, 235

Heflin, M. B., Gorenstein, M. V., Lawrence, C. R., & Burke, B. F., 1992, *Astrophysical Journal,* **378**, 519

Hewitt, J., Burke, B., Turner, E., Schneider, D., Lawrence, C., Langston, G., & Brody, J., 1988a, in J. Moran, J. Hewitt, & K. Lo (eds.), *Gravitational Lenses: Proceedings, Cambridge, Massachusetts, USA 1988*, No. 330 in Lecture Notes in Physics, pp 147–158, Springer-Verlag

Hewitt, J., Turner, E., Schneider, D., Burke, B., Langston, G., & Lawrence, C., 1988b, *Nature,* **333**, 537

Hewitt, J. N., Turner, E. L., Lawrence, C. R., Schneider, D. P., & Brody, J. P., 1992, *Astrophysical Journal,* **104**, 968

Högbom, J., 1974, *Astrophysical Journal Supplement,* **15**, 417

Katz, C., 1994, *Private communication*

Katz, C. & Hewitt, J. N., 1995, *in preparation*

Kochanek, C., 1991, *Astrophysical Journal,* **373**, 354

Kochanek, C., 1995, *Astrophysical Journal,* **445**, 672

Kochanek, C. & Narayan, R., 1992, *Astrophysical Journal,* **401**, 461

Kochanek, C. S., 1994, *Astrophysical Journal,* **436**, 56

Kovner, I., 1987, *Astrophysical Journal,* **312**, 22

Langston, G., Conner, S., Lehár, J., Burke, B., & Weiler, K., 1990, *Nature,* **344**, 43

Langston, G., Schneider, D., Coner, S., Carilli, C., Lehár, J., Burke, B., Turner, E., Gunn, J., Hewitt, J., & Schmidt, M., 1989, *Astronomical Journal,* **97**, 1283

Laplace, P. S., 1795, *Exposition du Système du monde*

Lavery, R. & Henry, J., 1988, *Astrophysical Journal Letters,* **329**, L21

Lawrence, C., Elston, R., Jannuzi, B., & Turner, E., 1994, Astronomical Journal in press

Lawrence, C. R., 1995, *Private communication*

Lawson, C. L. & Hanson, R. J., 1974, *Solving Least Squares Problems*, Prentice-Hall, Englewood Cliffs, NJ

Lebach, D. E., Corey, B. E., Shapiro, I. I., Ratner, M. I., Webber, J. C., Rogers, A. E. E., Davis, J. L., & Herring, T. A., 1995, *submitted to Physical Review Letters*

Lehár, J., Hewitt, J. N., Roberts, D. H., & Burke, B., 1992, *Astrophysical Journal,* **384**, 453

Lynds, R. & Petrosian, V., 1986, *Bulletin of the American Astronomical Society,* **18**, 1014

Maoz, D. & Rix, H.-W., 1993, *Astrophysical Journal,* **416**, 425

Michell, J., 1784, *Trans. R. Soc. London,* **74**, 35

Milhalas, D. & Binney, J., 1981, *Galactic Astronomy*, Freeman, San Francisco, CA

Moore, C. & Hewitt, J., 1995, *submitted to the Astrophysical Journal*

Narasimha, D. & Chitre, S., 1989, *Astronomical Journal,* **97**, 327

Narasimha, D., Subramanian, K., & Chitre, S., 1987, *Astrophysical Journal,* **315**, 434

Narayan, R. & Nityananda, R., 1986, *Annual Reviews of Astronomy and Astrophysics,* **24**, 127

Nelder, J. & Mead, R., 1965, *Computer Journal,* **7**, 308

Oke, J. B. & Sandage, A. R., 1968, *Astrophysical Journal,* **154**, 21

Patnaik, A., 1993, in J. Surdej, D. Fraipont-Caro, E. Gosset, S. Refsdal, & M. Remy (eds.), *Gravitational Lenses in the Universe*, pp 311–323, Université de Liège, Institut d'Astrophysique

Pence, W., 1976, *Astrophysical Journal,* **203**, 39

Perley, R. A., Schwab, F. R., & Bridle, A. H. (eds.), 1989, *Synthesis Imaging in Radio Astronomy*, No. 6 in Conference Series, Astronomical Society of the Pacific

Porcas, R. W., Booth, R. S., Browne, I. W. A., Walsh, D., & Wilkinson, P. N., 1981, *Nature,* **289**, 789

Press, W. H., Flannery, B. P., Teukolsky, S. A., & Vetterling, W. T., 1988, *Numerical Recipes*, Cambridge University Press

Press, W. H., Rybicki, G. B., & Hewitt, J. N., 1992, *Astrophysical Journal,* **385**, 404

Refsdal, S., 1964, *Monthly Notices of the Royal Astronomical Society,* **128**, 307

Refsdal, S., 1966, *Monthly Notices of the Royal Astronomical Society,* **132**, 101

Roberts, D. H., Lehár, J., Hewitt, J. N., & Burke, B. F., 1991, *Nature,* **352**, 43

Rogers, A. E. E., 1983, *Science,* **219**, 51

Rogers, A. E. E., 1993a, *VLBA Scientific Memorandum Number 3*

Rogers, A. E. E., 1993b, *VLBA Scientific Memorandum Number 4*

Schechter, P. L. & Moore, C. B., 1993, *Astronomical Journal,* **105**, 1

Schneider, P., Ehlers, J., & Falco, E. E., 1992, *Gravitational Lenses*, Springer-Verlag

Schwab, F. R., 1984, *Astronomical Journal,* **89**, 1076

Schwab, F. R. & Cotton, W. D., 1983, *Astronomical Journal,* **88**, 688

Seljak, U., 1994, *Astrophysical Journal,* **436**, 509

Seljak, U., 1995, *Ph.D. thesis*, Massachusetts Institute of Technology

Shapiro, I., 1963, *Physical Review Letters,* **13**, 789

Soldner, J., 1804, *Berliner Astron. Jahrb.,* p. 161

Sramek, R. A. & Schwab, F. R., 1989, in R. A. Perley, F. R. Schwab, & A. H. Bridle (eds.), *Sythesis Imaging in Radio Astronomy*, No. 6 in Conference Series, pp 117–138, Astronomical Society of the Pacific

Thompson, A. R., Moran, J. M., & Jr., G. W. S., 1986, *Interferometry and Synthesis in Radio Astronomy*, John Wiley and Sons, New York, NY

Tinsley, B. M., 1972, *Astrophysical Journal,* **178**, 319

Wallington, S. & Kochanek, C., 1995, *Astrophysical Journal,* **441**, 58

Walsh, D., Carswell, R., & Weymann, R., 1979, *Nature,* **279**, 381

Wehrle, A., Cohen, M., Unwin, S., Aller, H., Aller, M., & Nicolson, G., 1992, *Astrophysical Journal,* **391**, 589

Weinberg, S., 1972, *Gravitation and Cosmology: Principles and Applications of the General Theory of Relativity*, John Wiley and Sons, New York, NY

Weymann, R., Latham, D., Angel, J., Green, R., Liebert, J., Turnshek, D., Turnshek, D., & Tyson, J., 1980, *Nature,* **285**, 641

Witt, H. J., Mao, S., & Schechter, P. L., 1994, *submitted to the Astrophysical Journal*

Zwicky, F., 1937a, *Physical Review,* **51**, 290

Zwicky, F., 1937b, *Physical Review,* **51**, 679

5895-29